



ISSN: 1694- 7398
Year: 2020
Volume: 8
Issue: 2
<http://journals.manas.edu.kg>
journals@manas.edu.kg

PUBLICATION PERIOD

Manas Journal of Engineering (MJEN) is published twice year, MJEN is a peer reviewed journal.

OWNERS Kyrgyz - Turkish Manas University
Prof. Dr. Alpaslan CEYLAN
Prof. Dr. Asilbek KULMIRZAYEV

EDITOR Prof. Dr. Nahit AKTAŞ

ASSOCIATE EDITOR Assit. Prof. Dr.Rita İSMAİLOVA

FIELD EDITORS

Prof. Dr. Asilbek ÇEKEEV	(Mathematics, Topology)
Prof. Dr. Anarkül URDALETOVA	(Mathematics)
Prof. Dr. Osman TUTKUN	(Chemistry and Chemical Engineering)
Prof. Dr. İbrahim İlker ÖZYİĞİT	(Biotechnology and Bioengineering)
Assoc. Prof. Dr. Anarseyit DEYDİEV	(Food Engineering, Food Technology)
Assoc. Prof. Dr. Gülbübü KURMANBEKOVA	(Biology, Biochemistry)
Assoc. Prof. Dr. Raimbek SULTANOV	(Computer Engineering, Information Technology)
Asist. Prof. Dr. Emil OMURZAKOĞLU	(Nanoscience, Nanotechnology, Nanomaterials)
Asist. Prof. Dr. Rita İSMAİLOVA	(Computer Engineering, Information Technology)

EDITORIAL BOARD

Prof. Dr. Ali Osman SOLAK	(Chemistry)
Prof. Dr. Selahattin GÜLTEKİN	(Chemical Engineering)
Prof. Dr. Zarlık MAYMEKOV	(Environmental and Ecological Engineering)
Prof. Dr. Coşkan İLICALI	(Food Engineering)
Prof. Dr. Ulan BİRİMKULOV	(Computer Engineering)
Prof. Dr. Fahreddin ABDULLAEV	(Applied Mathematics and Informatics)
Assoc. Prof. Dr. Tamara KARAŞEVA	(Physics)

EDITORIAL ASSISTANTS

Assit. Prof. Dr.Rita İSMAİLOVA
Dr. Ruslan ADİL AKAI TEGİN
Kayahan KÜÇÜK
Jumagul NURAKUN KYZY

CORRESPONDENCE ADDRESS

Kyrgyz Turkish Manas University
Chyngyz Aitmatov Avenue 56 Bishkek, KYRGYZSTAN
URL: <http://journals.manas.edu.kg>
e-mail: journals@manas.edu.kg
Tel : +996 312 492763- Fax: +996 312 541935



CONTENT

Nuran Celikci Cengiz Ayhan Ziba Mustafa Dolaz	Synthesis and characterization of carboxymethyl shrimp chitosan (CMSCh) from waste shrimp shell	77-83
Janyl Iskakova Jamila Smanalieva	Investigation of rheological behavior of Kyrgyz traditional food Sary mai	84-89
Omer Faruk Er Ali Cavak Adnan Aldemir Hilal Kivrak	Investigation of hydrazine electrooxidation performance of carbon nanotube supported Pd monometallic direct hydrazine fuel cell anode catalysts	90-98
Tuba Erşen Dudu	Removal of anionic phenol red from water solution in the batch system by using N,N-dimethylacrylamide and 3-acrylamidopropyl-trimethyl ammonium chloride-based polymeric hydrogels	99-105
Suha Orçun Mert Zehra Özçelik Ceyda Kök	Modelling, sensitivity and exergy analysis of triple-pressure heat recovery steam generator	106-114
Tuba Öztürk Hande Akbaş Gülşen Aydın Keskin	Dye removal from synthetic and dye bath wastewater by electrocoagulation method and isotherms	115-124
Ümit Ecer Şakir Yılmaz Tekin Şahan	Effective clay material enriched with thiol groups for Zn(II) removal from aqueous media: A statistical approach based on response surface methodology	125-131
Serap (Gungor) Koc	Pumice and perlite co-substituted hydroxyapatite: Fabrication and characterization	132-137
Hüseyin Boran Osman Gunaydın Kadir Gucluer	Investigation of engineering properties of blast furnace slag additive mortars	138-143
Mehmet Şahin	Forecasting COVID-19 Cases based on mobility	144-150
Bora Aslan Kerem Ataşen	A blockchain based lifelong learning platform: The Smart University	151-154
Burak Oğul Dağıstan Şimşek	On the recursive sequence $x_{n+1} = \frac{x_{n-14}}{1 + x_{n-2}x_{n-5}x_{n-8}x_{n-11}}$	155-163

Synthesis and characterization of carboxymethyl shrimp chitosan (CMSCh) from waste shrimp shell

Nuran Celikci¹, Cengiz Ayhan Ziba², Mustafa Dolaz^{3,*}

¹ Department of Material Science and Engineering, Institute of Science and Technology, Kahramanmaraş Sutcu Imam University, Kahramanmaraş, Turkey, ORCID:0000-0003-2927-3603

² Department of Chemical Technologies, Afsin Vocational School, Kahramanmaraş Sutcu Imam University, Kahramanmaraş, Turkey, ORCID:0000-0003-2886-5762

³ Department of Environmental Engineering, Faculty of Engineering, Kyrgyz-Turkish Manas University, Bishkek, Kyrgyz Republic, mustafa.dolaz@manas.edu.tr, dolazmustafa@gmail.com, ORCID: 0000-0001-7117-6714

ABSTRACT

Chitin, the main component of shellfish such as crab and shrimp, is one of the most used biopolymers after cellulose. Today, although recycling of waste is becoming increasingly important, large quantities of seafood shells such as crab and shrimp are being destroyed around the world without much evaluation. Chitosan, which is non-toxic, biodegradable-biocompatible and has many application advantages compared to chitin, is used in many sectors, especially cosmetics, pharmaceuticals, and agriculture, as it shows superior properties compared to other biopolymers in terms of chemical and physical properties. In this study, in order to evaluate waste shrimp shells (WSS), shrimp shells were first removed from their minerals and proteins by deproteinization, demineralization, and deacetylation processes. Then, chitosan and carboxymethyl shrimp chitosan (CMSCh) were synthesized by isolation of chitin. The structures of Chitin-chitosan and CMSCh were characterized by spectroscopic methods (FT-IR, XRD, and NMR) and the deacetylation degrees of them were calculated. Also, surface morphologies and thermal properties were analyzed by SEM and DTA-TG, respectively.

ARTICLE INFO

Research article

Received: 13.11.2020

Accepted: 17.12.2020

Keywords:

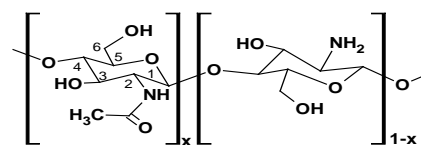
chitosan,
cmsch,
nmr,
waste shrimp shells,
recycle

*Corresponding author

1. Introduction

Chitin, the second most common biopolymer after cellulose occurring in nature [1], is a mucopolysaccharide found in the shells of marine animals such as crab and shrimp. It is also found in the skeleton of insects and in the structure of the cell walls of fungi, mollusks, arthropods, bacteria, and some plants. The structure of chitin is similar to cellulose but contains monomer units of 2-acetamido-2-deoxy- β -D-glucose (N-acetylglucosamine) linked together by β (1 \rightarrow 4) linkages. There are two hydroxyl groups per repeating monomer in the chitin and reactions take place via the more reactive primary hydroxyl group (C6-OH) because it is sterically less inhibited. In general, the shells part of sea animals such as crabs, lobsters, and shrimps consists of 30-40 % protein, 30-50 % calcium carbonate and calcium phosphate, and 20-30% chitin. The protein, calcium carbonate, and calcium phosphate in the shell of these marine animals are limited by some of the applications of chitin. Therefore the chitin is deproteinized and demineralized to remove its proteins and minerals (calcium carbonate, phosphate). The demineralized and

deproteinized chitin has a light pink color due to the presence of astaxanthin pigment. The pigment in the crustacean shells forms complexes with chitin. When a bleached product is desired, this pigment can be eliminated during the decolorization step [2]. Finally, chitin is deacetylated and converted to chitosan. Deacetylstone is usually made at high temperatures with a highly concentrated sodium hydroxide solution to remove some or all the acetyl group from chitin. As a result of the deacetylation of the chitin (60 % and above), "chitosan" is obtained (Scheme 1). Where x (Scheme 1) is the degree of acetylation defined as the mole ratio of acetylated repeating units over total repeating units. If $x > 0.5$, the structure chitin (1 \rightarrow 4)-2-acetamido-2-deoxy- β -D-glucan, if $x < 0.5$ chitosan (1 \rightarrow 4)-2-amino-2-deoxy- β -D-glucan).



Scheme 1. Chitin and Chitosan

Chitosan a product of the deacetylated chitin has attracted attention because of its biocompatibility, biodegradability, nontoxicity, antimicrobial activity, low immunogenicity, inexpensiveness, and accessibility [3, 4]. It is a multifunctional and eco-friendly compound which is known as an amino polysaccharide comprised of β -(1, 4)-2-acetamido-2-deoxy-D-glucopyranosyl and β -(1, 4)-2-amino-2-deoxy-d-glucopyranosyl units [5]. The most important advantage of the chitosan compared to the chitin is solubility in weak acid solutions owing to the protonation of its amino groups. However, chitosan has poor solubility in water due to its very stable crystalline structure arising from strong hydrogen bonds. This is limited its some application areas. Hence, the solubility of chitosan can be improved by depolymerization and its chemical modifications [6]. Chitosan has three reactive groups, primary and secondary hydroxyl groups and amino groups (Scheme 1). These reactive groups in chitosan can be easily chemically modified and changed the physical and mechanical properties. Compared with other water-soluble chitosan derivatives, carboxymethyl chitosan (CMCh) has been widely used because of its ease of synthesis, ampholytic character and possibilities for large applications. CMCh, one of the main derivatives of chitosan obtained by carboxymethylation, has unique properties such as significant biological properties, biocompatibility, gel-forming capacities, non-toxicity, biodegradability, low immunogenicity, antioxidant activities and solubility in a wide pH range [7]. Due to these properties, CMCh has used especially many biomedical applications like wound healing, bio-imaging, tissue engineering and drug/gene delivery [7]. Further, it is also frequently used in cosmetic production and composite materials because of the antimicrobial activity, moisture absorption-retention, antimicrobial and emulsion stabilizing properties of CMCh [6, 8-9].

In this study, to evaluate waste shrimp shells (WSS), shrimp shells were first removed from their minerals and proteins by deproteinization and demineralization processes. Then after the deacetylation of chitin, chitosan was obtained. Then, chitosan and carboxymethyl shrimp chitosan (CMSCh) were synthesized by isolation of chitin. The structures of chitin-chitosan and CMSCh were characterized by spectroscopic methods (FT-IR, XRD and NMR) and the deacetylation degrees of them were calculated. Also, surface morphologies and thermal properties were analyzed by SEM and DTA-TG, respectively.

1. Materials and methods

The waste of shrimp shells (WSS) used in this study was kindly obtained from the Kahramanmaraş local fish market in Turkey. Other chemicals and solvents (NaOH, NaOCl, chloroacetic acid (MCA), glacial acetic acid, 2-propanol, acetone, methanol, ethanol) were analytical grade and used without further purification. The spectroscopic identification of compounds was performed using Scanning Electron

Microscope (SEM) (Jeol/Neoscope Jcm-5000) at EHT = 20kV, The Fourier Transform Infrared (FT-IR) spectrums were taken from 4000 to 400 cm^{-1} using a Perkin Elmer Spectrum 400 Infrared Spectrophotometer with ATR apparatus, X-Ray Diffraction (XRD) patterns were analyzed using XRD diffractometer (Philips X'Pert PRO) with $\text{CuK}\alpha$ radiation operating, the voltage of 40 kV and current of 30 mA at monochromatic radiation ($\lambda=154060$ nm), The Thermal behaviors were measured using a TG-DTA (Seiko II, Japan) and Nuclear Magnetic Resonance (^1H NMR) spectrums were recorded at 30 oC in D₂O using a Bruker-200 MHz Varian spectrometer (90o pulse and 16 scans).

1.1. Isolation of chitin and chitosan

In this study, pink shrimp (*Solenocera melantho*) shells were collected at a local fish market to obtain chitin and chitosan. Firstly, to remove organic compounds found on the surface of shrimp shells, they were washed with tap water and then distilled water. The WSS was laid on a clean surface (Figure 1) and dried at room temperature for 48 hours. The shells were then milled with a lab-scale hammer mill and passed through a 60-80 (0.177-0.250 mm) mesh screen to obtain the uniform size. The synthesis of chitin and chitosan was carried out according to the study by Chang and Tsai [10]. Isolation of chitin involves four traditional steps: demineralization, deproteinization, decolorization and deacetylation with slight modifications. In fact, the isolation of chitin specifically consists of only two steps: demineralization and deproteinization, which involves the dissolution of calcium carbonate with HCl and the removal of proteins with NaOH, respectively



Figure 1. Washed (A) and dried (B) WSS

Step 1: Deproteinization

In order to remove the proteins from the powder of waste shrimp shells, 1 g WSS was weighed and added to 12.5 mL 2.5 M NaOH solution and mixed at 75 °C for 6 hours. This solution, which was brought to room temperature, was filtered with filter paper. The separated residue was washed with distilled water to neutral pH and dried.

Step 2: Demineralisation

1 g of WSS powder was added to 9 mL 1.7 M HCl acid solution and mixed at 65 °C for 6 hours to remove minerals (calcium carbonate, phosphate). The reaction mixture was

brought to room temperature, filtered, and washed with distilled water until the pH of the residue was neutral.

Step 3: Decoloration

The decoloration step was carried out to remove pigments. The chitin powder was extracted with acetone and dried at room temperature for 2 hours. It was then bleached with 0.315% (v/v) sodium hypochlorite (NaClO) solution (containing 5.25% available chlorine), solid:solvent ratio 1:10, w/v [11].

Step 4: Deacetylation

For the N-deacetylation of the chitin obtained from decolorized chitin powder, 26 mL of 60% NaOH solution was added per gram of chitin and stirred at 107 °C for 6 hours. After the mixing process, the mixture, which lowered to room temperature, was filtered through a filter paper and washed with distilled water to neutralize the pH. The residue remaining on the filter paper was dried in an oven at 50 °C.

1.2. Determination of chitosan's deacetylation degree (DD)

The degree of deacetylation of chitosan was determined by conductometric titration. To determine the DD, 5 g of chitosan was kept in the desiccator for 3 hours to bring it to a constant weight. 4 g chitosan (weight on a dry basis) was dissolved with 20 mL of 0.1 M HCl acid and the solution was transferred 250 ml flask for titration. Then, 2 drops of methyl orange were added to the solution, and the solution was mixed until the color turned pink. This solution, which was stirred until its color turned pink to orange, was titrated with 0.1 M NaOH. DD value was calculated according to the formula below by recording the amount of NaOH consumed in the titration [12-13].

$$DD(\%) = 2,03x \frac{V2 - V1}{m + 0,0042(V2 - V1)}$$

Where;

m= weight of sample (g)

V1= volume of NaOH added

V2= volume of HCl added

2.03= coefficient resulting from the molecular weight of chitin monomer unit

0.0042= coefficient resulting from the difference between molecular weights of chitin and chitosan monomer units.

2.3. Preparation of carboxymethyl shrimp chitosan (CMSCh)

CMSCh was synthesized by treating chitosan with aqueous sodium hydroxide solution and then reacting with monochloroacetic acid (MCA) according to the study of Kusuma et al. [14]. 3 grams of chitosan was suspended in 65 mL of isopropyl alcohol and stirred at room temperature for 10 minutes. 22 mL of 40% NaOH solution (w/w) was added to this suspension and stirred for another 30 minutes. Then 15 grams of MCA was added to this basic suspension and stirred at 45 °C for 3 hours. The solid residue obtained by filtration

of this cooled solution was washed with pure methanol and neutralized with glacial acetic acid. It was then washed with 80% methanol and several times absolute ethanol and dried to constant weight. The images of the obtained chitin, chitosan and CMSCh, and their formulas are given in Figure 2 and in Figure 3, respectively.



Figure 2. Images of dried shrimp shell, chitin, chitosan and carboxymethyl shrimp chitosan

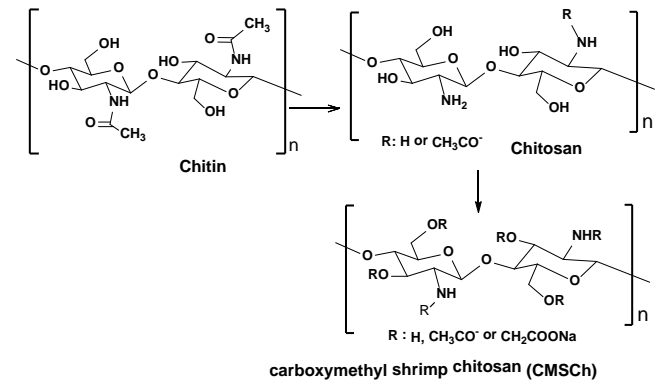


Figure 3. Chitin, Chitosan and CMSCh

2. Result and discussion

Although chitin, which is the second most abundant in nature after cellulose as a natural polymer, is widely used in many areas, some problems may be encountered in practice due to its tight supra-molecular structure. For this reason, it is preferred to use chitosan, which is obtained as a result of deacetylation of chitin, instead of chitin. Some parameters such as deacetylation degree and molecular weight, especially pH, viscosity and color are the properties that determine the use of chitosan. In our study, shrimp shells were firstly purified from minerals and proteins by deproteinization and demineralization processes. Demineralization consists in the removal of minerals, primarily calcium carbonate. Its generally performed by acid treatment using HCl, HNO₃, H₂SO₄, CH₃COOH and HCOOH [15, 16]. Conventionally, demineralization is accomplished using dilute hydrochloric acid at different concentrations (up to 10% w/v) at room temperature, during different incubations time. Demineralization is easily achieved because it involves the decomposition of calcium carbonate into the water-soluble calcium salts with the release of carbon dioxide as shown in the following equation [17]:



Most of the other minerals present in the shellfish cuticle react similarly and give soluble salts in presence of acid. Then, salts can be easily separated by filtration of the chitin solid phase followed by washing using deionized water. Another step is the decolorization of chitin to remove decolorizing agents. The color of chitin products is varied from cream white to intermediate pink color. Because chitin has a light pink or near-white color due to the presence of astaxanthin pigment. For commercial acceptability, the chitin produced from crustacean sources needs to be decolorized which is a process to remove astaxanthins and pigments or bleached to yield cream white chitin powder [15]. When a bleached product is desired, this pigment can be eliminated during the decolorization step [2, 11]. In the last step, chitosan was obtained from the chitin by deacetylation process. Then, obtained chitosan CMSCh was synthesized from obtained chitosan thus waste shrimp shells were evaluated by the synthesis of carboxymethyl shrimp chitosan (CMSCh) from chitin-chitosan. The structures of chitin-chitosan and CMSCh were characterized by spectroscopic methods such as FT-IR, XRD, and NMR, and deacetylation degrees were calculated. In addition, surface morphologies and thermal properties were investigated by SEM and DTA-TG, respectively.

2.1. Degree of deacetylation

The physiological properties of chitosan, especially solubility and molecular weight are determined by its degree of deacetylation [1]. Deacetylation is the process to convert chitin to chitosan by the removal of acetyl groups from the molecular chain of chitin. It is generally obtained by treatment with concentrated sodium or potassium hydroxide solution (40–50 %) at 100 °C or higher, for 30 min or longer to remove some or all of the acetyl groups from the polymer. Thus, the chitosan compound having a highly chemically reactive amino group (-NH₂) is formed. The process of deacetylation is carried out to different degrees depending on its applications. The N-acetyl groups cannot be removed by acidic reaction without hydrolysis of the polysaccharide, thus, alkaline methods must be employed for N-deacetylation [18]. Different researches have reported that the degree of solubility of chitosan is higher for higher degrees of deacetylation (DD) and lower molecular weight [19]. The degree of deacetylation of chitosan ranges from 56 to 99 % with an average of 80 % depending on the crustacean and the preparation methods [20]. In this study, when the acetylation time was 3 hours (chitosan-4), the highest acetylation degree (73.88%) was obtained. As the reaction time was longer, the degree of deacetylation started to decrease (Table 1).

Table 1. Degrees of deacetylation depending on the reaction time of the obtained chitosan

Samples	DD (%)
chitosan -1 (treated for 0.5 h)	57.80
chitosan -2 (treated for 1 h)	65.57
chitosan -3 (treated for 2 h)	73.45
chitosan -4 (treated for 3 h)	73.88
chitosan -5 (treated for 4 h)	72.21
chitosan -6 (treated for 5 h)	65.45

Our results proved that CMSCh prepared at temperatures of 45 oC were soluble in water as in other literature [21-22]. Compared with chitosan, the solubility of CMCh in an aqueous solution could be explained with the introduction of the carboxymethyl group. The properties of chitosan and carboxymethyl shrimp chitosan are compared in Table 2.

Table 2. Comparative characteristic of chitosan and CMSCh

Characteristic	Chitosan	CMSCh-4
Appearance	powder	powder
Colour	pale white	pure white
Odor	light	odorless
DD, %	81	-
Solubility	in acidic medium	in water

2.2. Scanning electron microscopy (SEM) of Chitosan and CMSCh

SEM analysis results for chitosan and CMSCh-4 were shown in Figure 4. Based on this SEM analysis, while the chitosan surface was smooth and flat and had no fibrous structure CMCh surface was lamellar and microstructured. The fact that CMSCh-4 has an uneven surface property indicates the presence of a new formation adhering to the chitosan surface [14, 23]. Increasing magnification from 1000× to 3000× was revealed the recessed and porous surface of CMCh-4.

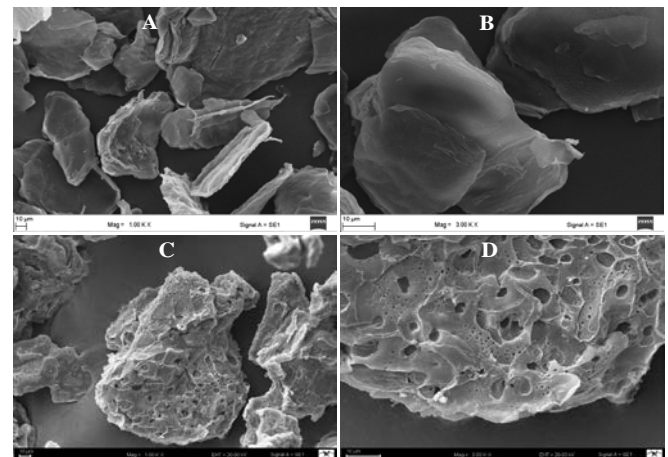


Figure 4. SEM images of chitosan with a magnification of (A) 1000 and (B) 3000 times and CMSCh-4; (C) 1000 and (D) 3000 times

2.3. FTIR spectrums of Chitosan and CMSCh

FTIR spectra of chitosan and CMSCh-4 were shown in Figure 5. The FT-IR spectrum of chitosan showed a wide and broad absorption band between 3401 and 3250 cm^{-1} due to -OH and -NH₂ vibration [24]. This vibration band can be attributed to the presence of free amine formed in chitosan as a result of deacetylation. The significant peaks at around 2971 cm^{-1} are assigned to the asymmetrical and symmetrical stretching vibrations of methylene groups confirm the insertion of long aliphatic chains in the CMSCh molecular structure [25]. A band at 1590 cm^{-1} was observed, which is attributed to the angular deformation of the N-H bonds of the amino group. The band at 1373 cm^{-1} due to the symmetrical angular deformation of CH₃, and the appearance of peaks at 1322 cm^{-1} correspondence to the carboxyl groups overlap with the deforming vibration of NH₂, C-O-C and C-OH [26-27]. The band corresponding to the polysaccharide skeleton including vibrations of the glycoside bonds, C-O and C-O-C asymmetric bridge-O-stretch at 1148 cm^{-1} . The peak at 1056 cm^{-1} was attributed C-O bend stretched and the second hydroxyl groups of a bridge -O- stretch was appeared at 1056 cm^{-1} [25]. The spectra of CMSCh-4 were similar to that of the chitosan (Figure 5). The occurrence of an intense band at 1589 cm^{-1} and a moderate band at 1409 cm^{-1} due to the symmetric and asymmetric axial deformations of COO⁻, respectively, confirms the introduction of the carboxymethyl groups [24]. The appearance of a peak at 1409 cm^{-1} corresponding to the carboxyl group -CH- and CH₃ groups are indicate the carboxymethylation on both the amino and hydroxyl groups of chitosan [27-30]. These results showed that the carboxymethylation was achieved successfully.

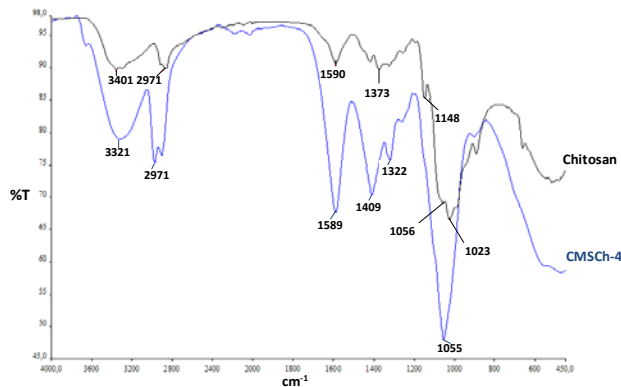


Figure 5. FTIR spectra of chitosan and CMSCh-4

2.4. ¹H-NMR spectrum of CMCh

The ¹H-NMR spectrum of prepared CMSCh-4 was illustrated in Figure 6. In the ¹H-NMR spectrum of CMSCh, signal at 3.8-3.2 ppm was observed; the signal was evidence of N-carboxymethylation. The signal observed between 1.80 and 1.90 ppm corresponds to the hydrogen bonded to the C2 glucosamine ring, while the signals between 3.25 and 3.83 ppm probably as a consequence of the carboxymethylation of

the hydroxyl groups bonded to the carbon atoms C3, C4, C5 or C6 of the glucopyranose that are overlapped, and the signal assigned at 4.8 ppm was due to the solvent [24, 26]. The signal centered at 1.80 ppm corresponds to the hydrogens of the methyl moieties belonging to the acetamido groups. Importantly signal that was observed at 8.36 ppm is assigned to the carbonyl carbons of carboxymethyl groups [31], while the one detected at 8.34 ppm corresponds to the carbonyl carbon of -COCH₃ of the parent chitosan.

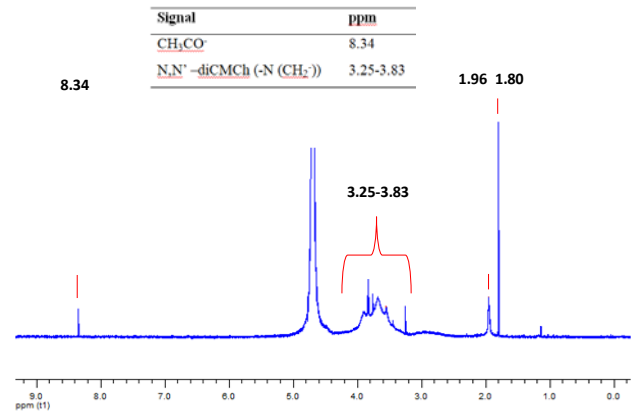


Figure 6. ¹H NMR of CMSCh-4

2.5. XRD spectrums of Chitosan and CMSCh

XRD patterns of chitosan and CMSCh-4 were shown in Figure 7. The characteristic peaks of chitosan appeared a range of $2\theta=20^\circ$ while the characteristic peaks of CMSCh appeared a range of 32° . In the chitosan, the characteristic peak seen at 20° was decreased significantly after carboxymethylation [23]. Based on the obtained results of the XRD diffractogram, it can be said that the sharp peaks that exist on chitosan appear at different angles when compared to the sharp peaks found in CMSCh-4. CMSCh was recognized in some literature by the appearance of characteristic peaks that are less sharp than the characteristic peaks of chitosan at about 32° [14, 32]. These results show that the addition of a large number of substituents to the chitosan polymer, which disrupts the hydrogen bond and constitutes a significant steric barrier in chitosan, significantly changes the crystallinity pattern. The presence of carboxymethyl groups which substitute the hydrogen atoms of the hydroxyl and amino groups of chitosan, decrease the formation of hydrogen bonds. This is due to the less number of hydrogen bonds formed between carboxymethyl shrimp chitosan molecules than chitosan.

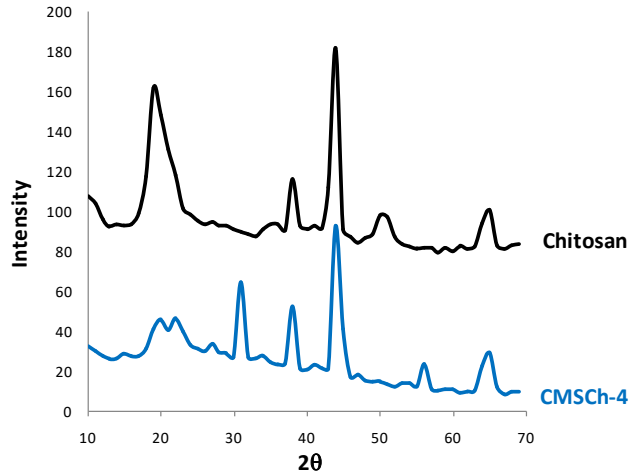


Figure 7. XRD pattern of Chitosan and CMSCh-4

2.6. TG-DTA spectrums of Chitosan and CMSCh

The thermal behaviors of chitosan and CMSCh were investigated at a temperature range of 30-600 °C. As can be seen in Figure 8, the thermal decomposition progress for the initial weight loss in chitosan 8% and CMSCh-4 7% was observed at 100 °C, as a consequence of water evaporation [29]. The high decomposition in both was around 200-350 °C. In the second stage, the weight loss of chitosan and CMSCh-4 is related to the decomposition of non-volatile components [33-34]. Endothermic peaks occurred at 291 °C in chitosan, 287 °C in CMCh-4. Moreover, the mass loss is 31.12% and 19.44%, respectively. Chitosan was appeared to lose more weight than CMSCh-4 when the temperature rises above 350 °C. This can be attributed to the degradation of the part of the molecule that is deacetylated [29]. It was observed that the weight loss of chitosan at the final temperature (590 °C) was 99% while the CMSCh-4 was 50%. After TGA/DTA analysis can be concluded that CMSCh is suitable to be used in heating. All these observations revealed the higher thermal stability of synthesized CMSCh for potential application in some areas such as food processing and pharmaceutical preparations [27].

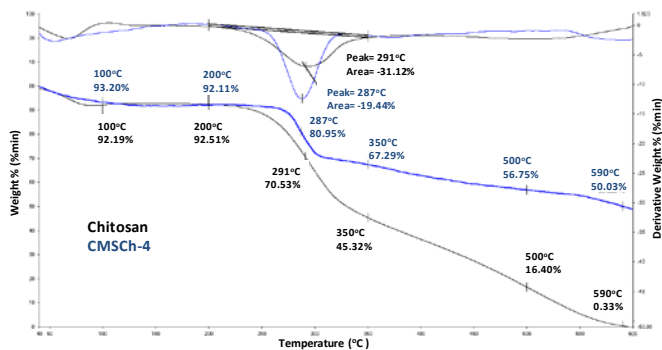


Figure 8. TG-DTA of Chitosan and CMSCh-4

3. Conclusions

Today, although recycling of waste is becoming increasingly important, large quantities of seafood shells such as crab and shrimp are being destroyed around the world without much evaluation. Chitosan, which is non-toxic, biodegradable-biocompatible and has many application advantages compared to chitin, is used in many sectors, especially cosmetics, pharmaceuticals and agriculture, as it shows superior properties compared to other biopolymers in terms of chemical and physical properties. For this purpose, Recycling of shrimp shells was evaluated by synthesizing carboxymethyl shrimp chitosan. Optimum conditions in the isolation of chitin-chitosan and synthesis of CMSCh have been compared with the literature. When the acetylation time was 3 hours (chitosan-4), the highest acetylation degree (73.88%) was obtained. It is understood that these natural polymers, whose structure is characterized by spectroscopic methods, can be used in many areas mentioned above.

References

- [1]. Yeul V.S., Ryalu S.S., "Unprecedented Chitin and Chitosan: A Chemical Overview", *Journal of Polymers and the Environment*, 21, (2013), 606-614.
- [2]. Stephene A.K., "Enhancement of degree of deacetylation of chitin and chitosan production", (2008). Article ID: 56025100.
- [3]. Fazli Y., Shariatinia Z., "Controlled release of cefazolin sodium antibiotic drug from electrospun chitosan-polyethylene oxide nanofibrous Mats." *Materials Science and Engineering: C*, 71, (2017), 641-652.
- [4]. Zheng K., Xiao S., Li W., Wang W., Chena H., Yang F., Qina C., "Chitosan-accorn starch-eugenol edible film: Physico-chemical, barrier, antimicrobial, antioxidant and structural properties", *International Journal of Biological Macromolecules*, 135, (2019), 344-352.
- [5]. Shariatinia Z., "Carboxymethyl chitosan: Properties and biomedical applications", *International Journal of Biological Macromolecules*, 120, (2018), 1406-1419.
- [6]. Mourya V.K., Inamdar N.N., Tiwari A., "Carboxymethyl chitosan and its applications", *Advanced Materials Letters*, 1, (2010), 11-33.
- [7]. Bratskaya S., Privar Y., Nesterov D., Modin E., Kodess M., Slobodyuk A., Marinin D., Pestov A., "Chitosan Gels and Cryogels Cross-Linked with Diglycidyl Ethers

- of Ethylene Glycol and Polyethylene Glycol in Acidic Media”, *Biomacromolecules*, 20, (2019), 1635–1643.
- [8]. Jimtaisong A., Saewan N., “Utilization of carboxymethyl chitosan in cosmetics”, *International Journal of Cosmetic Science*, 36, (2014), 12-21.
- [9]. Morandim-Giannetti A.A., Wecchi P.O., Jo Silverio P.A., Carlstron R., Bersanetti P.A., “Attainment and characterization of carboxymethyl chitosan hydrogels by enzymatic cross-linking”, *Journal of Thermal Analysis and Calorimetry*, 138, (2019), 3635-3643.
- [10]. Chang K.L.B., Tsai G., “Response Surface Optimization and Kinetics of Isolating Chitin from Pink Shrimp (*Solenocera melantho*) Shell Waste”, *Journal of Agricultural and Food Chemistry*, 45, (1997), 1900-19004.
- [11]. Fernandez-Kim S.O., “Physicochemical and Functional Properties Of Crawfish Chitosan As Affected By Different Processing Protocols”, *LSU Master's Theses*. 1338.
- [12]. No H.K., Meyers J.S.P., Lee K.S., “Isolation and Characterization of Chitin from Crawfish Shell Waste”, *Journal of Agricultural and Food Chemistry*, 37, (1989), 575-579.
- [13]. Biskup R.C., Jarosinska D., Rokita B., Ulanski P., Rosiak J.M., “Determination Of Degree Of Deacetylation Of Chitosan-Comparison Of Methods”, *Conference: New Aspects of the Chemistry and Applications of Chitin and its Derivatives At: Warsaw: XVII* (2012).
- [14]. Bulut M.O., Elibüyük U., “Production of Chitosan the Crab Chitin”, *Erzincan University Journal of Science and Technology*, 10, (2017), 213-219.
- [15]. No, H.K.; Hur, E.Y. Control of foam formation by antifoam during demineralization of crustacean shell in preparation of chitin. *J. Agric. Food. Chem.* (1998), 46, 3844–3846.
- [16]. Percot A., Viton C. Domard A., “Characterization of shrimp shell deproteinization”, *Biomacromolecules* 4(2003), 1380–1385.
- [17]. Younes I., Rinaudo M., “Chitin and Chitosan Preparation from Marine Sources. Structure, Properties and Applications”, *Mar. Drugs* 13 (2015), 1133-1174.

Investigation of rheological behavior of Kyrgyz traditional food Sary mai

Janyl Iskakova,^{1,*} Jamila Smanalieva²

¹ Kyrgyz-Turkish Manas University, Engineering Faculty, Environmental Engineering Department, Bishkek, Kyrgyzstan, janyl.iskakova@manas.edu.kg, ORCID:0000-0002-1614-3984

² Department of Food, Nutrition and Home Economics / Vocational Didactics, TU Dresden, 01217 Dresden, Germany, jamila.smanalieva@gmail.com, ORCID: 0000-0002-3929-4291

ABSTRACT

In this study, the rheological properties of shelf-stable and calorie-rich traditional product Sary mai, known as ghee were investigated at various temperatures for the first time. It was found that ghee at 20-30°C reacted as a non-Newtonian pseudoplastic fluid with yield stress value and flow curves fitted to the Herschel-Bulkley model. With increasing the temperature, ghee becomes more fluid: at 40°C the Ostwald-De-Waele model and 50 °C the Newton model were found as the most appropriate to fit the flow curves. The effective viscosity of ghee samples stored at room temperature decreased from 2.613 to 0.023 Pa·s with increasing temperature from 20 to 50°C. The Arrhenius relationship was employed to estimate the flow activation energy for the ghee samples stored at room and fridge temperatures and was found as $E_a = 26.3$ kJ/mol with $R^2 = 0.9350$ and $E_a = 29.9$ kJ/mol with $R^2 = 0.9223$, respectively. Due to the crystallization of fat globules at low temperature the activation energy, yield stress, consistency coefficient, flow index of ghee stored at fridge temperature was higher than the sample stored at room temperature. The amplitude-sweep was performed at 20°C for determining the yield point and the flow point. Obtained parameters provide useful information for the optimization of industrial processes and control of the quality of ghee.

ARTICLE INFO

Research article

Received: 13.06.2020

Accepted: 15.12.2020

Keywords:

Sary mai,
ghee,
rheological properties,
viscosity,
yield stress,
consistency coefficient,
flow index

*Corresponding author

1. Introduction

Previously nomadic, the Kyrgyz people usually used meat or milk-based foods in their diets. Traditionally, cow and mare milk were consumed in Kyrgyzstan. One of the widespread and calorie-rich dairy products Sary mai or ghee is made of cow milk. Ghee (clarified butter, butter oil) is anhydrous milk fat obtained by clarification of cow or buffalo milk fat at a high temperature. According to the literature review, ghee is widely consumed in Asia, Middle East, India, and African countries, therefore, methods of manufacture and characteristics vary [1-4].

According to the home technology of Kyrgyz ghee preparation shown in Fig.1, cow milk butter is melted on a gentle heat (up to 120 °C) to evaporate the moisture and to separate milk proteins. Heating is stopped when solid residues (milk proteins), called Chöbögö, start turning brown. Transparent yellow butter oil will be decanted from Chöbögö and can be stored for about one year in ambient temperature

due to its low moisture content and the presence of natural antioxidants, such as vitamin E [1].

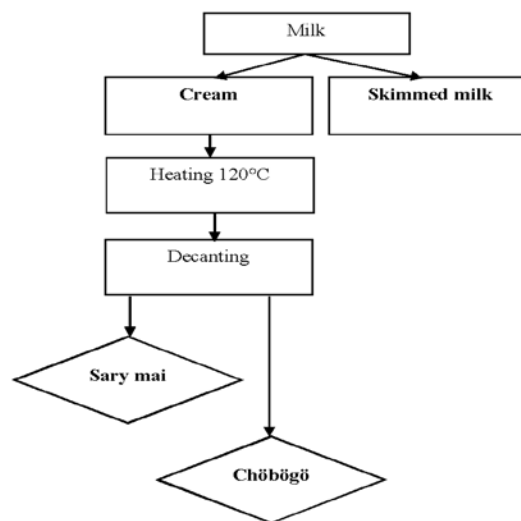


Figure 1. Production scheme of Kyrgyz ghee

According to Sharma et al. (2010), ghee contains a small amount of free fatty acids, phospholipids, sterols, and their esters, fat-soluble vitamins (A, D, E, and K), carotenoids, carbonyl compounds, hydrocarbons, charred casein, moisture and traces of trace elements like copper and iron [5]. Carbonyls, lactones, and free fatty acids are reported to be the key flavoring compounds of ghee. It may contain high amounts of conjugated linoleic acid, as reported as an anticarcinogen. According to Indian medicine, the consumption of ghee with medicinal plants and herbs helps humans to live longer allows its functional components to pass into deeper tissue levels improving their efficacy and bioavailability in the human body [6].

Traditional Kyrgyz ghee is usually produced in homes, villages, and small-scale industries. Ghee requires established technological parameters to produce on the industrial-scale. Generally, an understanding of the rheological properties of food materials has a direct effect on the optimization of processing stages such as production, handling, storage, and final quality [7]. Understanding the relationship between structure and rheology is crucial for the design of fat products with tailored mechanical functionality [8]. Therefore, the objectives of this study were: (i) to investigate the rheological properties of Kyrgyz ghee; (ii) to determine the best time-independent model to fit the flow curves of Kyrgyz ghee; (iii) to study the amplitude dependency of Kyrgyz ghee in the range of 20–50°C.

1. Materials and methods

1.1. Rotational rheological measurements

For this experiment, 2 ghee samples were purchased from Kyrgyz local markets and stored at room temperature (Sary mai 1) and fridge temperature at 5°C (Sary mai 2) until measurement. Composition of ghee according to a producer for melted butter as follows: fats 99.0 g, carbohydrates – 0.6 g, proteins – 0.3 g, vitamin A – 0.6 mg, and 891 kcal energy in 100 g of product [9]

During this study of rheological properties of Kyrgyz ghee rotational and oscillatory measurements have been performed. Rheological measurements were carried out by using the rheometer MCR 302 (Anton Paar, Graz, Austria) with concentric cylinder geometry CC27. Each analysis was done at least three times to avoid inaccuracy. The data, obtained from the rheological measurements were analyzed with the supporting rheometer software Rheoplus 32 Multi 6 version 3.40.

The rotational measurement condition was used to obtain flow behaviors of Kyrgyz ghee by measuring steady shear viscosity $\eta(\dot{\gamma})$ and shear stress $\tau(\dot{\gamma})$ at 20, 30, 40, and 50°C. The measurements were performed in three intervals: I) the shear rate was progressively increased linearly from 2 to 50 s⁻¹ over

a span of 90 s; II) the shear rate was constant at a shear rate of 50 s⁻¹; III) the shear rate was progressively decreased from 50 to 2 s⁻¹.

To describe the rheological behavior of ghee, the flow curves were modeled using equations such as Herschel-Bulkley, and Ostwald-De-Waele [10].

1) Herschel – Bulkley:

$$\tau = \tau_0 + K\dot{\gamma}^n \quad (1)$$

where τ_0 is yield stress, K is the consistency index for the Herschel-Bulkley model, $\dot{\gamma}$ is the shear rate.

2) Ostwald–de Waele (or Power-law):

$$\tau = K\dot{\gamma}^n \quad (2)$$

where K is the consistency index (Pa·sⁿ) and n is a flow behavior index.

For a Newtonian fluid $n = 1$ and K is simply the constant viscosity, η :

$$\tau = \eta\dot{\gamma} \quad (3)$$

The effect of temperature on dynamic viscosity and the activation energy was calculated using an Arrhenius-type equation (Eq. 3):

$$\ln \eta = \ln A + \left(-\frac{E_a}{R} \right) \cdot \left(\frac{1}{T} \right) \quad (4)$$

Where A is the pre-exponential factor, R is the ideal gas constant (8.31 J/mol·K), T is the absolute temperature (K). The activation energy E_a (J/mol) is the energy barrier that must be overcome before the flow process is initiated [11].

1.2. Oscillatory rheological measurements

This oscillatory test was carried out with a constant frequency of 0.1 Hz and variable strain amplitude from 0.01 to 100 % at 20°C. In this test, first the crossover point G'/G'' and an upper boundary of the Linear Viscoelastic (LVE) range were determined.

2. Results and discussion

2.1. Effect of shear rate and temperature on rheological parameters

The flow curves of ghee samples obtained at 20, 30, 40, and 50°C are shown in Figures 2 and 3. The results showed that samples behaved as non-Newtonian pseudoplastic fluid with

a value of yield stress (τ_0) at 20 and 30°C. The sample stored at fridge temperature has the highest consistency coefficient with high yield stress. However, with an increase in temperature the samples tended to shift to a Newtonian fluid at 40 and 50°C. This behavior is due to a reduction in flow resistance and structural change, the melting of fat globules. The same findings were previously described by Duhan et al. (2018) for Indian ghee at 30 and 36°C [12]. Taghizadeh and Razavi (2009) reported that pistachio butter samples show a loss of consistency between 45 and 65°C and behaved as a dilatant fluid with an increase in temperature [13].

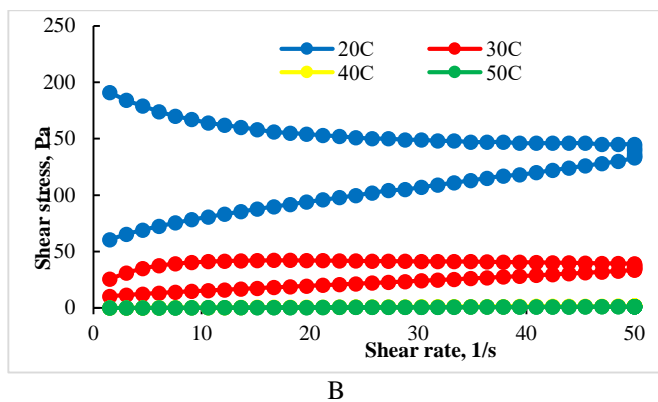
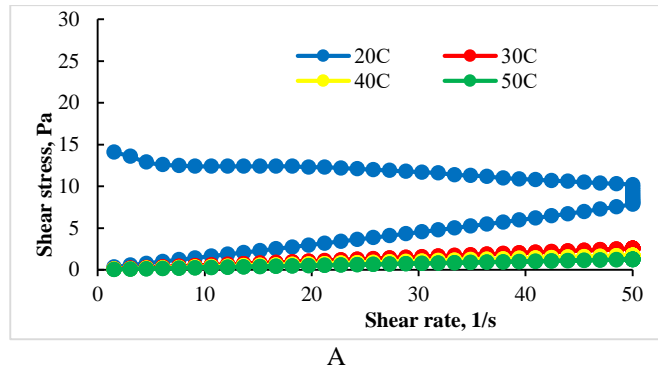


Figure 2. Flow curves of ghee samples with up and down curves at 20, 30, 40, and 50 °C of samples A) Sary mai 1; B) Sary mai 2.

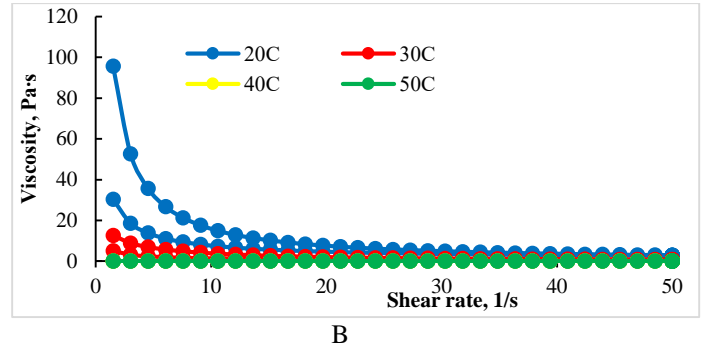
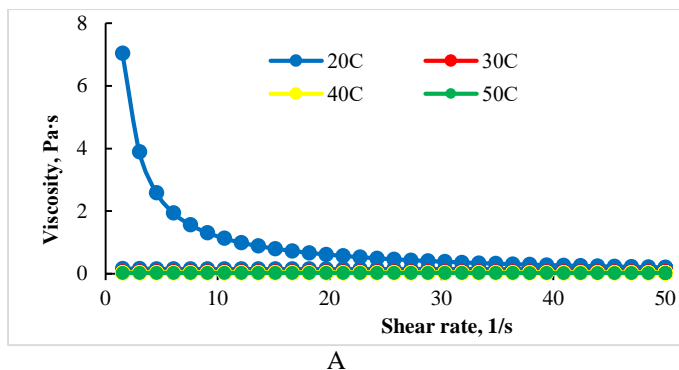


Figure 3. Shear rate and dynamic viscosity relationship of ghee samples at 20, 30, 40, and 50 °C with up and down curves A) Sary mai 1; B) Sary mai 2.

Fig. 3 showed the relationship of shear rate and dynamic viscosity of ghee samples was obtained at 20, 30, 40, and 50°C. The viscosity of ghee samples decreased under shear strain and showed shear-thinning behavior at 20 and 30°C. Three intervals test showed that viscosity equilibrium has not been established between structure degradation and rebuilding. Therefore, it can be concluded that internal network structures were broken down by shearing which leads to degradation of the material. At 40 °C, the viscosity of the up and down curves was nearly the same of both ghee samples and they behaved as a dilatant fluid with flow index $n = 1.0007$, which indicated the start of melting fatty acids. Further increase in temperature leads to the fully melting of fat crystals and at 50°C both samples of Kyrgyz ghee behaved as a Newtonian fluid. The melting and solidification behavior of fats is crucial in determining the rheological properties of fat and fat-containing foods. Naturally, occurring fats are multicomponent mixtures of triacylglycerols. According to Ronholt et al. (2012) and Moorthy (2018), the interactions between component triacylglycerols govern, broadly, the melting behavior of a complete fat [14-15]. Also, other researchers stated that fatty acid composition directly influences the rheological and thermal of animal fats [16].

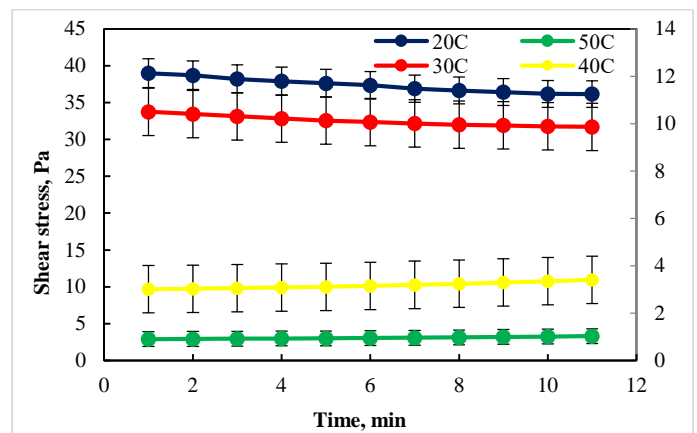


Figure 4. Time-dependent and time-independent flow of Kyrgyz ghee (average values of two samples)

To analyze the time-dependent flow behavior the second interval of flow curve ghee samples was studied at 20, 30, 40, and 50°C. The time-dependent flow exists when shearing at 20 and 30°C (Fig 6). The hysteresis area between the upward and downward curves of shear rate vs shear stress rheograms at 20°C is shown in Table 1. The highest hysteresis area Ath

was at 20°C and with the increase of temperature Ath of Sary mai 1 decreased from 2671.70 to 0.49 Pa/s and the Ath of Sary mai 2 from 8722.13 to 0.49 Pa/s. The upwards and downwards ramp at 40 and 50°C did not differ from each other (see Fig. 2 and 3), therefore, it can be concluded that the sample's behavior is time-independent at these temperatures.

Table 1. Adjustment of experimental data of Kyrgyz ghee to the Herschel-Bulkley and Ostwald-De Wale models

Model	T (°C)	τ_0 (Pa)	K (Pa·s ⁿ)	n	R ²	SD	η_{eff} (Pa·s), at $\dot{\gamma}=50$ s ⁻¹	Ath(Pa/s)
Sary mai 1								
Herschel-Bulkley	20	53.38	4.984	0.701	0.9988	0.72	2.613	2621.70
Herschel-Bulkley	30	9.23	0.692	0.902	0.9985	0.26	0.594	865.22
Ostwald De-Wale	40	-	0.033	1.007	0.9999	0.00	0.034	0.31
Newton	50	-	0.023	1.000	0.9999	0.00	0.023	0.49
Sary mai 2								
Herschel-Bulkley	20	181.78	7.812	0.813	0.9984	2.09	7.394	8722.13
Herschel-Bulkley	30	27.02	1.425	0.866	0.9993	0.32	1.384	1138.91
Ostwald De-Wale	40	-	0.035	1.002	1.0000	0.00	0.035	0.31
Newton	50	-	0.024	1.000	0.9999	1.24	0.024	0.49

The rheological parameters are reported as mean and standard deviation of three independent measurements

The down curves were fitted to the Hershel-Bulkley, Ostwald De-Wale, Newton models to describe the flow behavior of the samples. To find the best-fitted rheological model, the estimated statistical parameters such as correlation coefficient R² and standard deviation SD were compared. The Hershel-Bulkley model was found the most appropriate to fit the flow curves of Kyrgyz ghee at 20 and 30°C with R² ranged from 0.9984 to 0.9988 and the Newton model was best-fitted at 40 and 50°C with R² ranged from 0.9999 to 1. The yield stress (τ_0) and the consistency coefficients (K) value obtained by fitting the rotational speed versus apparent viscosity data of down curve to a Hershel-Bulkley (Eq. 1), Ostwald-De Wale (Eq. 2), and Newton models (Eq. 4) are presented in Table 1. The consistency coefficient K measures the average viscosity of the non-Newtonian fluid and in our study decreases with increasing the temperature from 7.812 to 0.033 Pa·sⁿ. The lowest K value was obtained for samples at 30°C. Taghizadeh & Razavi (2009) studied the rheological behavior of pistachio butter at 25 and 35°C the Herschel-Bulkley model was found to be the best to describe the rheological property with the coefficient of determination ranging from 0.952 to 0.999. The consistency coefficient K of pistachio butter without any emulsifier at 25°C was 17.14 Pa·sⁿ and was higher than K of Sary mai 2 at 20°C and was found as 7.812 Pa·sⁿ [13].

The effective viscosity was calculated according to the suitable flow models at a shear rate of 50 1/s. The effective viscosities of ghee decreased from 7.394 to 0.023 Pa·s

(sample “Sary mai 2”) with increasing temperature from 20 to 50°C. This behavior could be explained based on the subsequent reduction of fluid viscosity due to the melting of crystals of ghee and shifting of the flow behavior from pseudoplastic to shear-thinning nature without the yield stress with an increase in temperature. These findings are in agreement with Duhan et al. (2018) reported for Indian cow milk (Desi) ghee [12].

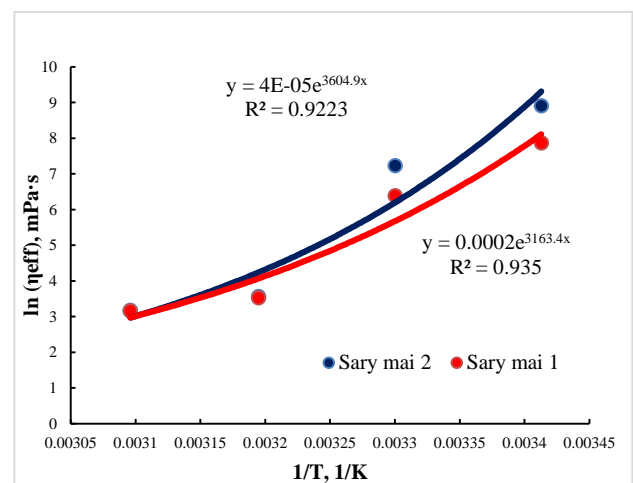


Figure 6. Arrhenius-type model fit for Kyrgyz ghee

The temperature effect on the viscosity of Kyrgyz ghee was estimated using Eq. 3 for temperatures between 20 and 50°C. As shown in Fig.6 the activation energy, E_a , and coefficient A were calculated for Sary mai 1 as 26.3 KJ/mol and 0.0002 respectively, with a correlation coefficient $R^2 = 0.9350$. For Sary mai 2 the activation energy was found as 29.9 KJ/mol, A was calculated as 0.00004 with $R^2 = 0.9223$. The high activation energy of ghee indicates that more energy is required for the product flow. Due to the crystallization of fat globules at low temperature the activation energy of Sary mai 2 stored at fridge temperature was higher than the sample stored at room temperature. Taghizadeh and Razavi (2009) calculated the activation energy of pistachio butter at 25–65°C at the range between 10.3–52.5 kJ/mol [13].

3.2. Dynamic shear rheological properties

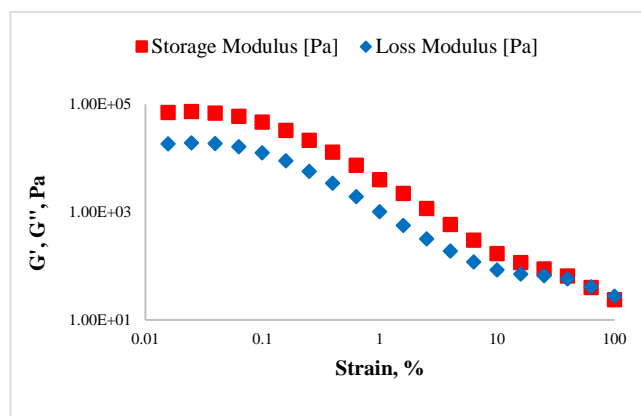


Figure 7. Amplitude-sweep of ghee with a LVE range and the crossover point $G' = G''$

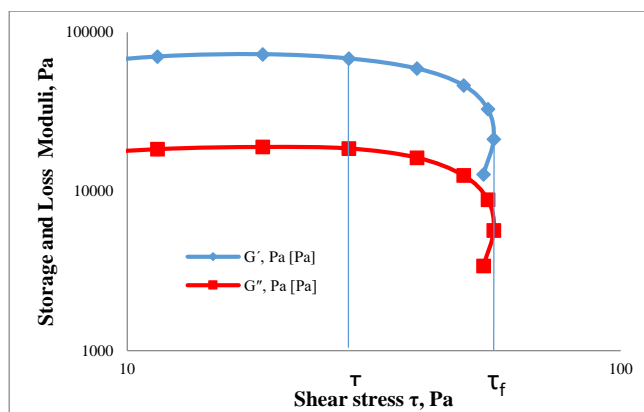


Figure 8. Amplitude sweep, presented with shear stress τ plotted on the x-axis, showing the yield point τ_y at the limit of the LVE region and the flow point τ_f at the crossover point $G' = G''$.

The amplitude-sweep was performed at 20°C for describing the deformation behavior of ghee in the non-destructive deformation range and at determining the upper limit of this range and determining the yield point and the flow point. As shown in Fig. 7 storage and loss moduli are nearly parallel in

the lower strain range from 0.01 to 0.1 % strain, this region called Linear Viscoelastic (LVE) region. Rohm (1993) found that the LVE behavior of commercial butter was present up to a critical shear strain of 0.001 % and that structure breakdown due to shear strain between 0.001 and 0.01 % was fully recoverable [17].

Upper LVE range the ghee as nonlinear elastic material do not show linear behavior in any range of stress. However, the storage modulus G' of ghee had higher values than loss modulus G'' , that indicated the visco-elastic structure with more solid-like behavior that was better described by storage modulus G' . These findings are in accordance with Herrera and Hartel (2012), who stated that milk fat has solid-like behavior with higher storage modulus G' (viscoelastic material). Nevertheless, the storage modulus G' of milk fat varied with all processing conditions such as the temperature of crystallization (25 to 30°C), cooling rate, and agitation rate. Moduli were higher for samples crystallized at a slow cooling rate, decreased with agitation rate, and were lower for the 30–70 % blend at all processing conditions used [18]. According to Macias Rodriguez (2019), margarine and milk butter at room temperature also behave as elastoplastic substances [9]. In the current study, with increasing deformation the crossover point G'/G'' achieved at 51 % strain, after this point the storage modulus G' decreases and is less than loss modulus G'' , that indicates the inner structure gets softer, the flow of samples commences. Fig. 8 shows that in the region between yield point and flow point, $G' > G''$. Within this yield zone, the initial structural strength of the LVE region has already decreased but the ghee sample still predominantly displayed the properties of solid matter. The yield point τ_y (or yield stress) – is the value of the shear stress at the limit of the LVE region. The flow point τ_f (or flow stress) – is the value of the shear stress at the crossover point $G' = G''$. At higher shear, the viscous portion will dominate and the sample flows. Both values are dependent on the measuring conditions, for example, on the preset (angular) frequency [11]. The flow stress from the rotation test and oscillation test are comparable (53.38; 55.3 Pa, respectively). From these observations, it can be concluded that ghee has solid-like (viscoelastic) and highly strain-dependent behavior at 20°C.

3. Conclusion

Rheological measurements showed that Kyrgyz ghee behaved as a non-Newtonian fluid with viscoelastic properties with yield stress value and the Hershel-Bulkley model was found to be superior in predicting the shear rate-stress data at 20–30°C and at 40°C the Ostwald model was best-fitted to the flow curves of ghee. According to the hysteresis area analysis, ghee samples performed time-dependent properties at 20–40°C which was highly dependent on storage conditions. At fridge temperature Kyrgyz ghee crystallizes and builds up hard consistency with high yield stress. Higher temperatures lead to the melting of fat crystals and time-independent

Newtonian properties at 50°C were measured. Thus, the rheological parameters of the Kyrgyz ghee samples were highly shear and temperature-dependent. The amplitude sweep also showed that the ghee has a viscoelastic structure solid-like and the structural stability was highly strain-dependent. Obtained rheological parameters are helpful for the establishment and optimization of technological parameters such as transport by pipe or pump and agitation process to produce ghee on the industrial-scale.

References

- [1]. Sserunjogi M.L., Abrahamsen R.K., Narvhus J., "A review paper: Current knowledge of ghee and related products," *International Dairy Journal*, 8(8), (1998), 677–688. doi:10.1016/S0958-6946(98)00106-X.
- [2]. Gosewade S., Gandhi K., Ranvir S., Kumar A., Lal D., "A study on the physico-chemical changes occurring in ghee (butter oil) during storage," *Journal of Dairy Science*, 70, (2017), 81–88.
- [3]. Mehta B.M., "Ragi (*Eleusine coracana* L.) - A natural antioxidant for ghee (butter oil)," *International Journal of Food Science and Technology*, 41(1), (2006), 86–89. doi:10.1111/j.1365-2621.2006.01348.x.
- [4]. Alganesh T.G., Yetenayet B.T., "Traditional butter and ghee production, processing and handling in Ethiopia: A review," *African Journal of Food Science*, 11(4), (2017), 95–105. doi:10.5897/ajfs2016.1544.
- [5]. Sharma H., Zhang X., Dwivedi C., "The effect of ghee (clarified butter) on serum lipid levels and microsomal lipid peroxidation," *An International Quarterly Journal of Research in Ayurveda*, 31(2), (2010), 134. doi: 10.4103/0974-8520.72361.
- [6]. Suryakumari C., Anusha A., Anitha P., Ravindra D., "Formulation and evaluation of cow ghee as a base fast and sustained release chloroquine phosphate suppositories", *World Journal of Pharmacy and Pharmaceutical Sciences*, 3(6), (2014), 1493–1509.
- [7]. Tabilo-Munizaga G., Barbosa-Cánovas G. V., "Rheology for the food industry," *Journal of Food Engineering*, 67, (2005), 147–156. doi: 10.1016/j.jfoodeng.2004.05.062.
- [8]. Macias Rodriguez B.A., "Nonlinear rheology of fats using large amplitude oscillatory shear tests," in *Structure-Function Analysis of Edible Fats*, Marangoni A.G., Ed., 2nd ed. Urbana: AOCS Press, 2019, pp. 169–195. <https://doi.org/10.1016/B978-0-12-814041-3.00006-X>
- [9]. Interstate standard for melted butter and milk fat, GOST 32262-2013.
- [10]. Rao M.A., "Rheology of fluid and semisolid foods: principles and applications". New York: Springer Science+Business Media, LLC, 2007.
- [11]. Mezger T.G., "The rheology handbook," Hannover: Vincentz Network, 2011.
- [12]. Duhan N., Sahu J.K., Naik S.N., "Temperature dependent steady and dynamic oscillatory shear rheological characteristics of Indian cow milk (Desi) ghee," *Journal of Food Science and Technology*, 55(10), (2018), 4059–4066. doi: 10.1007/s13197-018-3332-6
- [13]. Taghizadeh M., Razavi S.M.A., "Modeling time-independent rheological behavior of pistachio butter," *International Journal of Food Properties*, 12(2), (2009), 331–340. doi:10.1080/10942910701772048.
- [14]. Ronholt S., Kirkensgaard J.J.K., Pedersen T.B., Mortensen K., Knudsen J.C., "Polymorphism, microstructure and rheology of butter. Effects of cream heat treatment," *Food Chemistry*, 135(3), (2012), 1730–1739. <https://doi.org/10.1016/j.foodchem.2012.05.087>
- [15]. Moorthy A.S., "Melting and solidification of fats," in *Structure-Function Analysis of Edible Fats*, Marangoni A.G., Ed., 2nd ed. Urbana: AOCS Press, 2018, pp. 101–118. <https://doi.org/https://doi.org/10.1016/B978-0-12-814041-3.00004-6>
- [16]. Smanalieva, J., Ozbekova, Z., Kulmyrzaev, A., Fischer, P. "Investigation of fatty acid composition, thermal and rheological behavior of yak, cow and horse fats". *Manas Journal of Engineering*, 7(1), (2019), 24–33.
- [17]. Rohm H., "Rheological behaviour of butter at large deformations," *Journal of Texture Studies*, 24, (1993), 139–155.
- [18]. Herrera M.L., Hartel R.W., "Effect of processing conditions on physical properties of a milk fat model system: Rheology," *Journal of the American Oil Chemists' Society*, 77(11), (2000), 1189–1196. <https://doi.org/10.1007/s11746-000-0185-3>.

Investigation of hydrazine electrooxidation performance of carbon nanotube supported Pd monometallic direct hydrazine fuel cell anode catalysts

Omer Faruk Er,¹ Ali Cavak,¹ Adnan Aldemir,¹ Hilal Kivrak^{1,*}

¹ Van Yuzuncu Yil University, Faculty of Engineering, Department of Chemical Engineering, Van 65000, Turkey, hilalkivrak@yyu.edu.tr, hilalkivrak@gmail.com, ORCID: 0000-0001-8001-7854

ABSTRACT

In this study, carbon nanotube (CNT) supported Pd/CNT catalysts at varying Pd molar ratios (Pd involving among 0.1-20 wt %) are prepared via NaBH₄ reduction method. The surface of catalysts prepared for hydrazine electrooxidation are successfully characterized via N₂ adsorption-desorption measurements, X-ray diffractometer (XRD), X-ray photoelectron spectroscopy (XPS), and transmission electron microscope (TEM). Electrochemical measurements are performed using cyclic voltammetry (CV) and electrochemical impedance spectroscopy (EIS) techniques. According to the characterization results, for 5% Pd/CNT catalyst, the average particle size and the surface area are determined as 5.17 nm and 773.10 m² g⁻¹, respectively. Among Pd containing (0.1-20 wt %) CNT supported catalysts, 5%Pd/CNT catalyst exhibits the best current density as 6.81 mA cm⁻² (1122.63 mA mg⁻¹ Pd). Furthermore, 5% Pd/CNT catalyst shows the best charge transfer resistance (R_{ct}) compared to Pd/CNT catalysts. Pd/CNT catalysts are promising anode catalysts for direct hydrazine fuel cells.

ARTICLE INFO

Research article

Received: 28.09.2020

Accepted: 17.12.2020

Keywords:

Pd,
CNT,
hydrazine,
electrooxidation,
direct hydrazine fuel
cell,
anode

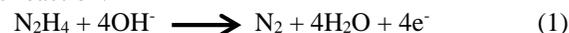
*Corresponding author

1. Introduction

The demand for energy, in which the vast majority of this demand is provided from fossil fuel is constantly increasing in the industrialized world [1, 2]. The use of fossil fuels that caused global warming and environmental pollution is constituted negative consequences for both nature and human life [3]. Fuel cell technologies could be employed to supply energy to cover the energy demand instead of fossil fuels [4].

Recently, the most commonly used fuels in fuel cell technology are hydrazine, formic acid [5], ethanol [6], methanol [7], glucose [8], and ethylene glycol [9] etc. Hydrazine is a preferable fuel due to its superior properties such as high energy density, low cost, zero CO₂ emission, convenient storage, and transportation ease [10, 11]. In addition, another feature of hydrazine is that its source (H₂ and N₂) is unlimited in nature. Hydrazine is not explosive and it has low toxicity in dilute aqueous solutions [11]. In direct hydrazine fuel cells (DHFC), catalyst poisoning products such as CO do not release, so the overvoltage of catalyst poisoning is low in DHFC [12]. Anode, cathode, and overall reaction of hydrazine electrooxidation are given as follows [13, 14]:

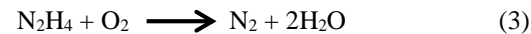
Anodic reaction:



Cathodic reaction:



Overall reaction:



As a result of reactions (1-3) occurring in the oxidation of hydrazine, only water and nitrogen are formed as products, and these products are released into the environment [15].

There are needs for low cost and more efficient catalysts with higher catalytic activity in hydrazine fuel cells. For this purpose, PtCu/C [16], P-Cu₂Ni/C [17], NiCoP/C [18], SeNCM [19], Ni₃S₂@Ni foam [20], Mn₂O₃-Fe₂O₃/CFs [21], Ni-Pt/C [22], nano-CuO/MGCE [23], Ni₃N nanoparticles [24], Co_{fiber}/Cu [25], Ni₂P@Ni₁₀Mo/Ni-Mo-O/NF [26], and Ni foam@Ag-Ni [27] catalysts were studied in DHFC for catalysts with low costs and higher catalytic activity. In addition, Yang et al. stated that the Ag/CNT catalyst prepared by modification Ag nanoparticles on CNT with benzyl

mercaptan showed high catalytic activity the hydrazine electrooxidation reaction [28]. In another study, Gao et al. remarked that Cu nanotube-graphene paper (Cu-GP) electrode developed by the facile electrodeposition method had high electrocatalytic activity and durability for DHFC in alkaline medium [29]. Furthermore, Asset et al. reported that NiMo/C catalyst prepared via wet impregnation process method, exhibited better catalytic activity compared to Ni/C catalyst

[30]. Liu et al. reported that the ternary CuNiCo LDH nanosheet array catalyst prepared via sulfurization-induced edge amorphization exhibited good catalytic activity and power durability[31]. The catalysts and maximum peak values compiled from the literature studies for hydrazine electrooxidation were given in Table 1.

Table 1: Catalysts and maximum peak values for hydrazine electrooxidation compiled from literature.

Catalyst	Preparation	Maximum Peak mA cm ⁻²	Reference
Pd black	---	4.12	[32]
Pd NCs	---	4.87	[32]
AuPd NCs	simple one-pot successive co-reduction	5.28	[32]
AuPd DANCs	simple one-pot successive co-reduction	9.57	[32]
Co@NM	electrochemical deposition	8.13	[33]
VGNH-45	scalable plasma-enhanced chemical vapor deposition	13	[34]
Bulk Au electrode	---	0.9	[35]
NPGL30	etching 12-carat white gold leaves	10.5	[35]
MnO/N-C	---	6.3	[36]
Pd/CNT	NaBH ₄ reduction	6.81	In this study

In this study, Pd/CNT catalysts were prepared at varying Pd weight loadings via NaBH₄ reduction method. The electrochemical performances of prepared catalysts were investigated via CV and EIS. These catalysts were characterized with advance surface characterization methods as XRD, XPS, and TEM to describe the surface chemical and physical properties. The particle size and the crystal structure of synthesized catalysts were determined via XRD and TEM.

2. Experimental measurement

2.1. Materials and Equipment

Potassium tetrachloropalladate (II) (K₂PdCl₄, 99.99%), Hydrazine (NH₂NH₂, 98%) sodium borohydride (NaBH₄, 99%), multi-walled carbon nanotube (MWCNT, 98%), KOH were purchased from Sigma-Aldrich and used as received. Nafion 117 solution (5%) was supplied from Sigma-Aldrich. Ag/AgCl reference electrode and Pt wire electrodes used in potentiostat were purchased from CH Instruments. Deionized water was distilled via water purification system (Milli-Q Water Purification System). All glass wares were washed with acetone and a wealth of rinsed with distilled water.

2.2. Preparation of catalysts and working electrodes

2.2.1. Synthesis of Pd/CNT catalysts

Pd/CNT catalysts were prepared by NaBH₄ reduction method. Pd metal precursor (Potassium tetrachloropalladate) was completely dissolved in pure water and then CNT was added. These mixtures were stirred in ultrasonic bath for two hours.

NaBH₄ was added to this mixture to reduce the salts in the medium. After the addition of NaBH₄, these mixtures were stirred in the ultrasonic bath for one hour and filtered. These catalysts were completely dried at 85 °C for 12 hours.

2.2.3 Preparation of working electrodes

The working electrode (glassy carbon electrode) was firstly polished by alumina. 3 mg of catalyst was distributed homogenously in 1 mL of 5% Nafion solution. Consequencely, a catalyst ink was obtained. Finally, 3 µl of catalyst ink was dropped on a working electrode and the electrode was dried at room temperature to remove the solvent.

2.3. Metal Characterization Techniques

Pd/CNT catalysts were characterized via N₂ adsorption-desorption, XRD, XPS, and TEM. Surface areas were measured through Micromeritics 3Flex equipment. The Pd diffractions on the surface that 5% Pd/CNT of the best ratio of these catalysts were determined using XRD. Particle size and surface metal distribution were found via TEM.

2.4. Electrochemical Measurements

All electrochemical measurements of Pd/CNT catalysts were determined by CV and EIS in 1 M KOH + 0.5 M N₂H₄ solution. These measurements were obtained using the three-electrode system in potentiostat CH660E. The electro-oxidation activities of these catalysts were performed by CV at the potential gap of -1.2 V to 0.8 V at 50 mv s⁻¹ scan rate. The electrochemical impedances of these catalysts were

obtained with EIS at 316 kHz and 0.046 Hz to 5 mV amplitude.

3. Results and discussion

3.1. Physical characterization

5% Pd/CNT catalyst was characterized by BET, XRD, XPS, and TEM. Fig. 1 shows the N_2 adsorption-desorption isotherm and XRD pattern of monometallic 5% Pd/CNT catalyst prepared via $NaBH_4$ reduction method. 5% Pd/CNT catalyst exhibited V-type adsorption-desorption shape with H1 type hysteresis loop (Fig. 1a) [5, 37]. Adsorption-desorption hysteresis loop is close to mesoporous pore structure. The average particle size, pore size, and pore volume of 5% Pd/CNT catalyst were found at 7.76 nm, 11.35 nm, $2.08 \text{ cm}^3 \text{ g}^{-1}$, respectively. Furthermore, BET surface area of 5% Pd/CNT was calculated as $773.10 \text{ m}^2 \text{ g}^{-1}$.

The XRD pattern of monometallic Pd/CNT catalyst is given in Figure 1b. It is found that the C (0 0 2) plane, which related to reflection of hexagonal carbon structure, diffraction peak located towards 25.6° [38]. The (1 1 1), (2 0 0), (2 2 0), and (3 1 1) planes, which shows face center cubic (fcc), belonging to Pd the diffraction peaks are subtended of 2θ values at 39.2° , 45.4° , 66.6° , and 79.7° , respectively [39]. In addition, Pd (1 1 0) diffraction peak was seen at 42.8° [40]. The crystal size for 5% Pd/CNT catalyst was calculated as 6.94 nm with the Scherrer's equation.

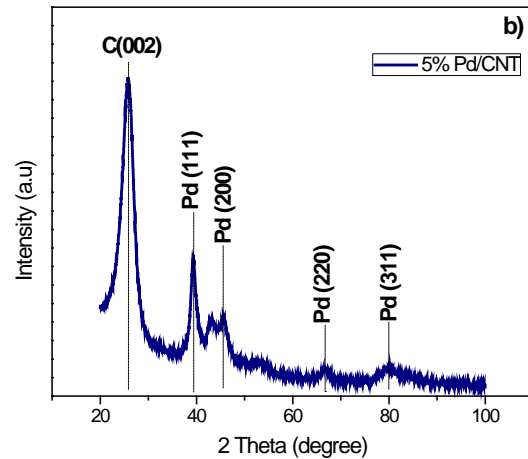
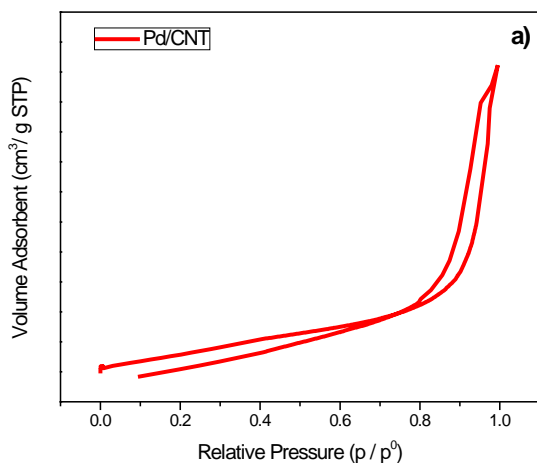


Figure 1. a) N_2 adsorption-desorption isotherm and b) XRD pattern of the monometallic 5% Pd/CNT catalyst.

Atomic differences on the CNT surface could be easily determined via XPS analysis [41]. The oxidation state of the Pd on CNT surface was determined by XPS analysis. Here, according to C 1s, which found at 284.4, was determined the binding energy of Pd (Fig. 2b). XPS spectra of Pd 3d, C 1s, O 1s, and general survey were given in Fig. 2 and the oxidation state of Pd 3d is presented in Table 2 for 5% Pd/CNT catalyst. The resolution of Pd 3d spectra was found for Pd^0 ($3d_{5/2}$ 335.6 eV; $3d_{3/2}$ 341.9 eV) and Pd^2 (PdO_2 339.0 eV) (Fig. 2a and Table 2). In addition, the undefined spectrum was seen at 351.2 eV that could be impurity remaining from the synthesis method (Table 2). The elemental state of Pd^0 on CNT surface was determined at relative density as 49.4 (Table 2). TEM was used to determine the particle size and morphological structure of 5% Pd/CNT catalyst. TEM images and particle size histogram of 5% Pd/CNT catalyst is given in Fig. 3. It is clearly seen that Pd nanoparticles were bonded with the exterior surface of CNT. Furthermore, from Fig. 3(b and c), one could note that Pd nanoparticles aggregated. In addition, Pd nanoparticles distributed homogeneously on the surface of CNT. It was found that the average particle size of 5% Pd/CNT catalyst as 5.17 nm (Fig. 3(f)).

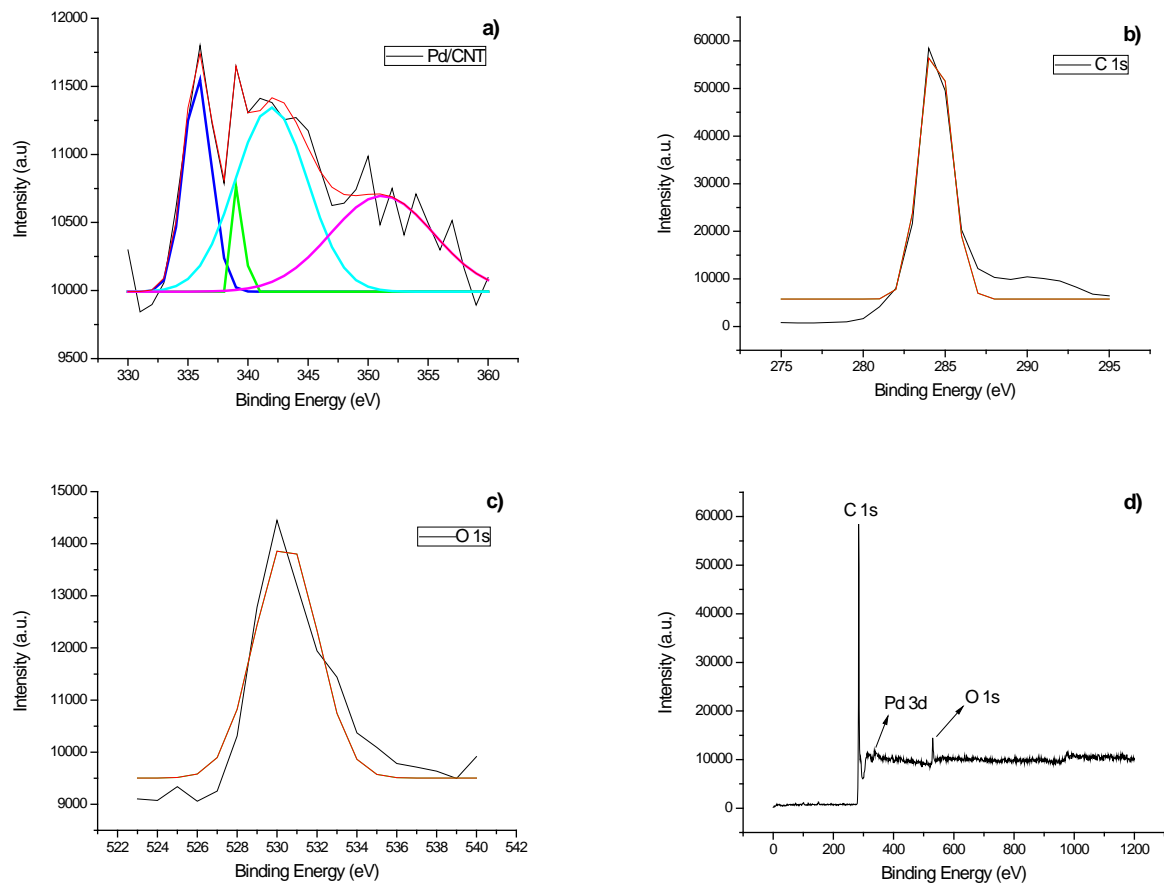


Figure 2. XPS spectra of a) Pd 3d, b) C 1s, c) O 1s, and d) general survey of Pd/CNT catalyst.

Table 2. Pd 3d binding energy of Pd/CNT electro-catalysts.

Catalyst	Species	Binding Energy (eV)	Possible Chemical State	Relative Intensity (%)	Reference
Pd/CNT	Pd 3d	335.6	Pd 3d _{5/2} (Pd ⁰)	24.5	[42]
		339.0	PdO ₂	24.7	[43]
		341.9	Pd 3d _{3/2} (Pd ⁰)	24.9	[42]
		351.2	Undefined	25.6	

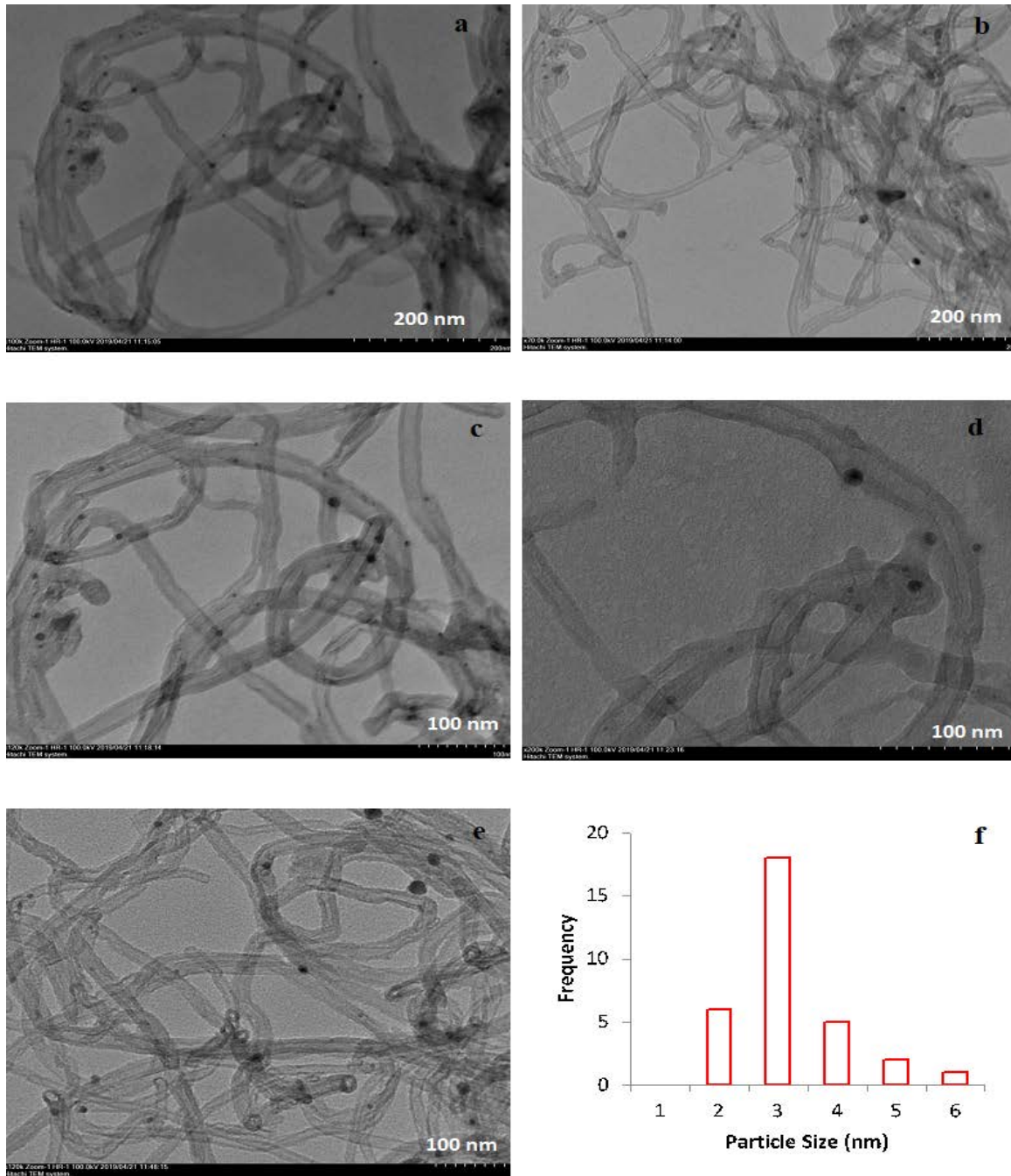


Figure 3. TEM images (a, b, c, d, and e) and particle size (f) of 5% Pd/CNT.

3.2. Electrochemical assessment

CV and EIS measurements were taken in 1 M KOH + 0.5 M N_2H_4 solution to determine hydrazine oxidation activities of Pd/CNT supported catalysts prepared at (0.1-20 wt %) Pt loadings via $NaBH_4$ reduction method. Initially, CV measurements of prepared catalysts were taken in 1 M KOH solution and in 1 M KOH + 0.5 M N_2H_4 solution at -1.0 V to 0.4 V potentials a scan rate of 50 mV s^{-1} , respectively. These results were presented in Fig. 4 and Table 3. The hydroxide

(OH⁻) adsorption-desorption peak was observed at among -0.4 V and 0.2 V for 0.1% Pd/CNT catalyst, but this peak was observed at -0.3 V and 0.2 V for 5% Pd/CNT catalyst (Fig. 4(a)). This could be explained by the fact that Pd nanoparticles are very well dispersed on the CNT surface, and thus lead to more OH⁻ adsorption. As seen, OH⁻ electrooxidation peaks for all prepared catalysts were seen. After reducing the surface oxidation of the catalyst, more Pd active sites were provided for adsorption and oxidizing the hydrazine. 5% Pd/CNT

catalyst among the prepared catalysts showed the highest performance as 6.81 mA cm^{-2} ($1122.63 \text{ mA mg}^{-1} \text{ Pd}$) for hydrazine electrooxidation (Fig. 4(b) and Table 3). In addition, the forward currents (I_f) and reverse currents (I_r) of these catalysts were studied. After evaluation of these results, we concluded that 5% Pd/CNT catalyst had the best activity for hydrazine electrooxidation (Table 3).

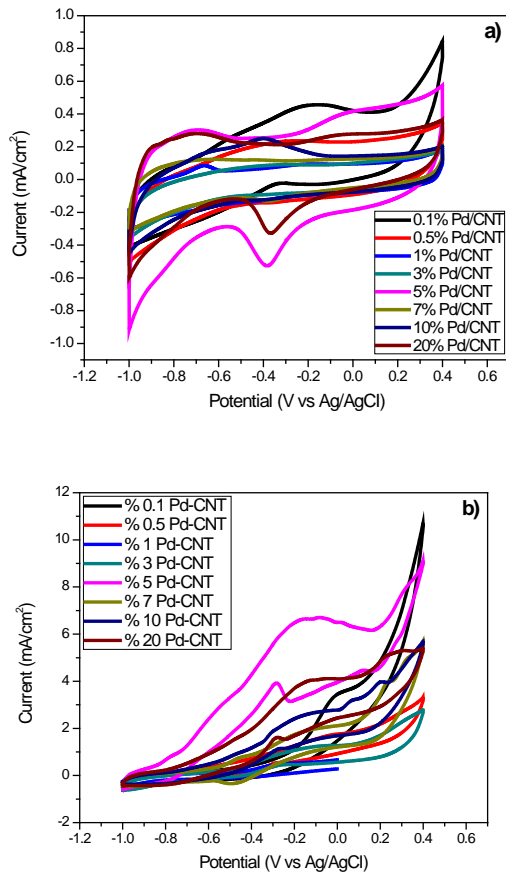


Figure 4. Cyclic voltammograms with a 50 mV s^{-1} scan rate in a) 1 M KOH solution on Pd/CNT catalysts and b) $1 \text{ M KOH} + 0.5 \text{ M N}_2\text{H}_4$ solution on Pd/CNT catalysts.

Table 3. Properties of the obtained peaks from CV results

Catalysts	Forward Peak		Reverse Peak		I_f/I_r	Peak Current Density (mA cm^{-2})
	I_f (mA cm^{-2})	E (V)	I_r (mA cm^{-2})	E (V)		
0.1% Pd/CNT	3.86	0.020	---	---	---	3.57
0.5% Pd/CNT	2.31	-0.004	1.12	-0.26	2.06	1.76
1% Pd/CNT	0.77	-0.203	0.24	-0.70	3.20	0.54
3% Pd/CNT	1.74	-0.015	1.10	-0.21	1.58	1.23
5% Pd/CNT	7.35	-0.081	4.40	-0.28	1.67	6.81
7% Pd/CNT	2.36	-0.047	1.42	-0.58	1.66	2.10
10% Pd/CNT	3.12	-0.031	2.02	-0.05	1.54	2.77
20% Pd/CNT	4.55	-0.031	2.06	-0.27	2.21	4.14

EIS method is the best method to investigate in a large variety of catalyst properties [44]. Nyquist plots were obtained at different potentials for 5% Pd/CNT catalyst and at 0.4 V for different percent Pd/CNT catalysts and presented in Figure 5. The Nyquist Plots obtained from EIS measurements were taken in $1 \text{ M KOH} + 0.5 \text{ M N}_2\text{H}_4$ solution. The Nyquist Plots are shaped usually as semicircle. These diameters of semicircles that correlate with charge transfer resistance (R_{ct}) could inform about the electrocatalytic activity of catalysts [45]. The smaller the diameter of the semicircles, the charge transfer resistance of the catalyst is smaller, which specified the high electrocatalytic activity of the catalyst. Thus, more the hydrazine electrooxidation reaction gets faster. From the measurements taken at different potentials on 5% Pd/CNT catalyst at 0.4 V, we observed that this catalyst displayed the best catalytic activity in hydrazine electrooxidation reaction (Fig. 5a). Furthermore, in the measurements taken at 0.4 V, it is found that among the Pd/CNT catalysts, 5% Pd/CNT catalyst possess the best the charge transfer resistance in hydrazine electrooxidation reaction (Fig. 5b). This could be explained by the fact that Pd nanoparticles are well distributed on the CNT surface and leads to oxidation of more hydrazine molecules.

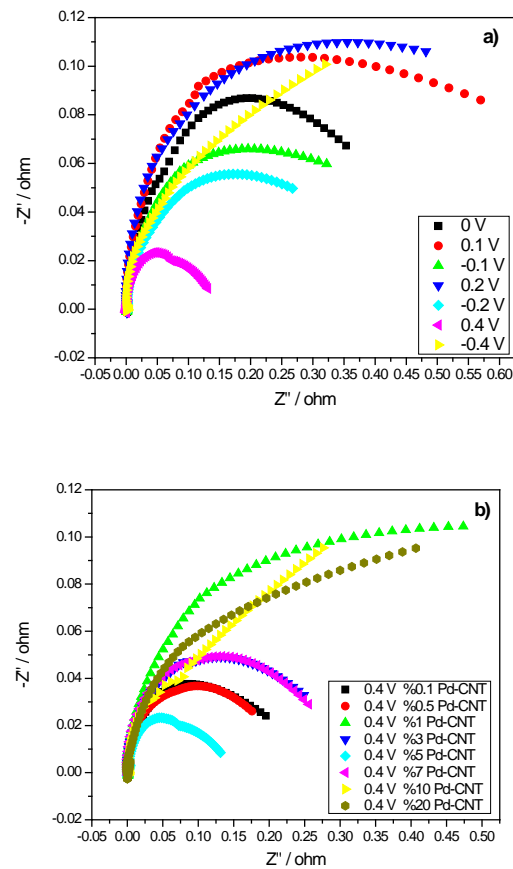


Figure 5. Nyquist Plots obtained in $1 \text{ M KOH} + 0.5 \text{ M N}_2\text{H}_4$ solution for electrodes modified with a) 5% Pd/CNT at different potentials and b) Pd/CNT catalysts at 0.4 V.

4. Conclusion

In this study, monometallic Pd/CNT supported catalysts were prepared via the NaBH₄ reduction method. These monometallic catalysts were characterized with advance surface characterization techniques as N₂ adsorption-desorption, XRD, XPS, and TEM. To investigate their hydrazine electrooxidation activities, electrochemical techniques as CV and EIS were employed. Among the Pd/CNT catalysts, 5% Pd/CNT catalyst showed the best performance in hydrazine electrooxidation. As a result, hydrazine electrooxidation measurements and characterization conclusions of these catalysts led the following results and insights:

- 5% Pd/CNT catalyst exhibited V-type adsorption-desorption shape with H1 type hysteresis loop, which is close to the mesoporous pore structure. This result indicates that 5% Pd/CNT catalyst has a large surface area.
- The average particle size of 5% Pd/CNT catalyst from XRD was determined as 6.94 nm. In addition, the average particle size from TEM for 5% Pd/CNT catalyst was obtained as 5.17 nm. It shows that XRD and TEM average particle sizes are close.
- 5% Pd/CNT catalyst, according to CV and EIS results, displayed the highest hydrazine electrooxidation activity and long term stability compared to other Pd/CNT catalysts in hydrazine electrooxidation reaction.
- This study is unique in terms of evaluating the effect of hydrazine electrooxidation in an alkaline medium.
- Pd/CNT catalysts are promising as anode catalysts for direct hydrazine fuel cells

Acknowledgment

O. F. Er thank to the council of higher education (YOK) for 100/2000 scholarship and the Scientific and Technological Research Council of Turkey (TUBITAK) for 2211-A scholarship.

References

- [1]. Er O.F., Caglar A., Ulas B., Kivrak H., Kivrak A., "Novel carbon nanotube supported Co@ Ag@ Pd formic acid electrooxidation catalysts prepared via sodium borohydride sequential reduction method", *Materials Chemistry and Physics*, 241, (2020), 122422.
- [2]. Ellis M.W., Von Spakovsky M.R., Nelson D.J., "Fuel cell systems: efficient, flexible energy conversion for the 21st century", *Proceedings of the IEEE*, 89, (2001), 1808-1818.
- [3]. Armeanu D.Ş., Gherghina Ş.C., Pasmangiu G., "Exploring the causal nexus between energy consumption, environmental pollution and economic growth: Empirical evidence from central and Eastern Europe", *Energies*, 12, (2019), 3704.
- [4]. Ulas B., Caglar A., Sahin O., Kivrak H., "Composition dependent activity of PdAgNi alloy catalysts for formic acid electrooxidation", *Journal of colloid and interface science*, 532, (2018), 47-57.
- [5]. Kivrak H., Atbas D., Alal O., Çögenli M.S., Bayrakceken A., Mert S.O., Sahin O., "A complementary study on novel PdAuCo catalysts: Synthesis, characterization, direct formic acid fuel cell application, and exergy analysis", *International Journal of Hydrogen Energy*, 43, (2018), 21886-21898.
- [6]. Sahin O., Duzenli D., Kivrak H., "An ethanol electrooxidation study on carbon-supported Pt-Ru nanoparticles for direct ethanol fuel cells", *Energy Sources, Part A: Recovery, Utilization, and Environmental Effects*, 38, (2016), 628-634.
- [7]. Kivrak H.D., "The effect of temperature and concentration for methanol electrooxidation on Pt-Ru catalyst synthesized by microwave assisted route", *Turkish Journal of Chemistry*, 39, (2015), 563-575.
- [8]. Huynh T.T.K., Tran T.Q.N., Yoon H.H., Kim W.-J., Kim I.T., "AgNi@ ZnO nanorods grown on graphene as an anodic catalyst for direct glucose fuel cells", *Korean Journal of Chemical Engineering*, 36, (2019), 1193-1200.
- [9]. Ulas B., Caglar A., Kivrak A., Kivrak H., "Atomic molar ratio optimization of carbon nanotube supported PdAuCo catalysts for ethylene glycol and methanol electrooxidation in alkaline media", *Chemical Papers*, 73, (2019), 425-434.
- [10]. Wang Y., Wang Q., Wan L.-Y., Han Y., Hong Y., Huang L., Yang X., Wang Y., Zaghbi K., Zhou Z., "KOH-doped polybenzimidazole membrane for direct hydrazine fuel cell", *Journal of Colloid and Interface Science*, 563, (2020), 27-32.
- [11]. Granot E., Filanovsky B., Presman I., Kuras I., Patolsky F., "Hydrazine/air direct-liquid fuel cell based on nanostructured copper anodes", *Journal of Power Sources*, 204, (2012), 116-121.
- [12]. Yamada K., Asazawa K., Yasuda K., Ioroi T., Tanaka H., Miyazaki Y., Kobayashi T., "Investigation of PEM

- type direct hydrazine fuel cell”, *Journal of power sources*, 115, (2003), 236-242.
- [13]. Yi Q., Chu H., Tang M., Zhang Y., Liu X., Zhou Z., Nie H., “A novel membraneless direct hydrazine/air fuel cell”, *Fuel cells*, 14, (2014), 827-833.
- [14]. Burshtein T.Y., Farber E.M., Ojha K., Eisenberg D., “Revealing structure–activity links in hydrazine oxidation: doping and nanostructure in carbide–carbon electrocatalysts”, *Journal of Materials Chemistry A*, 7, (2019), 23854-23861.
- [15]. Yin W.X., Li Z.P., Zhu J.K., Qin H.Y., “Effects of NaOH addition on performance of the direct hydrazine fuel cell”, *Journal of power sources*, 182, (2008), 520-523.
- [16]. Crisafulli R., de Barros V.V.S., de Oliveira F.E.R., de Araújo Rocha T., Zignani S., Spadaro L., Palella A., Dias J.A., Linares J.J., “On the promotional effect of Cu on Pt for hydrazine electrooxidation in alkaline medium”, *Applied Catalysis B: Environmental*, 236, (2018), 36-44.
- [17]. Wang W., Wang Y., Liu S., Yahia M., Dong Y., Lei Z., “Carbon-supported phosphatized CuNi nanoparticle catalysts for hydrazine electrooxidation”, *International Journal of Hydrogen Energy*, 44, (2019), 10637-10645.
- [18]. Liang B., Wang Y., Liu X., Tan T., Zhang L., Wang W., Nickel–cobalt alloy doping phosphorus as advanced electrocatalyst for hydrazine oxidation, *Journal of Alloys and Compounds*, 807, (2019), 151648.
- [19]. Wang T., Wang Q., Wang Y., Da Y., Zhou W., Shao Y., Li D., Zhan S., Yuan J., Wang H., “Atomically Dispersed Semimetallic Selenium on Porous Carbon Membrane as an Electrode for Hydrazine Fuel Cells”, *Angewandte Chemie*, 131, (2019), 13600-13605.
- [20]. Liu X., Li Y., Chen N., Deng D., Xing X., Wang Y., “Ni₃S₂@ Ni foam 3D electrode prepared via chemical corrosion by sodium sulfide and using in hydrazine electro-oxidation”, *Electrochimica Acta*, 213, (2016), 730-739.
- [21]. Li C., Li M., Bo X., Yang L., Mtukula A.C., Guo L., “Facile synthesis of electrospinning Mn₂O₃-Fe₂O₃ loaded carbon fibers for electrocatalysis of hydrogen peroxide reduction and hydrazine oxidation”, *Electrochimica Acta*, 211, (2016), 255-264.
- [22]. Lao S.J., Qin H.Y., Ye L.Q., Liu B.H., Li Z.P., “A development of direct hydrazine/hydrogen peroxide fuel cell”, *Journal of Power Sources*, 195, (2010), 4135-4138.
- [23]. Raof J.B., Ojani R., Jamali F., Hosseini S.R., “Electrochemical detection of hydrazine using a copper oxide nanoparticle modified glassy carbon electrode”, *Caspian Journal of Chemistry*, 1, (2012), 73-85.
- [24]. Lin X., Wen H., Zhang D.-X., Cao G.-X., Wang P., “Highly dispersed nickel nitride nanoparticles on nickel nanosheets as an active catalyst for hydrazine electrooxidation”, *Journal of Materials Chemistry A*, 8, (2020), 632-638.
- [25]. Zabielaite A., Balčiūnaitė A., Šimkūnaitė D., Lichušina S., Stalnionienė I., Šimkūnaitė-Stanynienė B., Naruškevičius L., Tamašauskaitė-Tamašiūnaitė L., Norkus E., Selskis A., “High Performance Direct N₂H₄-H₂O₂ Fuel Cell Using Fiber-Shaped Co Decorated with Pt Crystallites as Anode Electrocatalysts”, *Journal of The Electrochemical Society*, 167, (2020), 054502.
- [26]. Wen H., Cao G.-X., Chen M.-H., Qiu Y.-P., Gan L.-Y., Wang P., “Surface phosphorization of hierarchically nanostructured nickel molybdenum oxide derived electrocatalyst for direct hydrazine fuel cell”, *Applied Catalysis B: Environmental*, 268, (2020), 118388.
- [27]. Lei Y., Liu Y., Fan B., Mao L., Yu D., Huang Y., Guo F., “Facile fabrication of hierarchically porous Ni foam@ Ag-Ni catalyst for efficient hydrazine oxidation in alkaline medium”, *Journal of the Taiwan Institute of Chemical Engineers*, 105, (2019), 75-84.
- [28]. Yang G.-W., Gao G.-Y., Wang C., Xu C.-L., Li H.-L., “Controllable deposition of Ag nanoparticles on carbon nanotubes as a catalyst for hydrazine oxidation”, *Carbon*, 46, (2008), 747-752.
- [29]. Gao H., Wang Y., Xiao F., Ching C.B., Duan H., “Growth of copper nanocubes on graphene paper as free-standing electrodes for direct hydrazine fuel cells”, *The Journal of Physical Chemistry C*, 116, (2012), 7719-7725.
- [30]. Asset T., Roy A., Sakamoto T., Padilla M., Matanovic I., Artyushkova K., Serov A., Maillard F., Chatenet M., Asazawa K., “Highly active and selective nickel molybdenum catalysts for direct hydrazine fuel cell”, *Electrochimica Acta*, 215, (2016), 420-426.

- [31]. Liu W., Xie J., Guo Y., Lou S., Gao L., Tang B., "Sulfurization-induced edge amorphization in copper-nickel-cobalt layered double hydroxide nanosheets promoting hydrazine electro-oxidation", *Journal of Materials Chemistry A*, 7, (2019), 24437-24444.
- [32]. Chen L.-X., Jiang L.-Y., Wang A.-J., Chen Q.-Y., Feng J.-J., "Simple synthesis of bimetallic AuPd dendritic alloyed nanocrystals with enhanced electrocatalytic performance for hydrazine oxidation reaction", *Electrochimica Acta*, 190, (2016), 872-878.
- [33]. Zhao A., Sun H., Chen L., Huang Y., Lu X., "Development of highly efficient and scalable free-standing electrodes for the fabrication of hydrazine-O₂ fuel cell", *Materials Research Express*, 6, (2019), 085533.
- [34]. Akbar K., Kim J.H., Lee Z., Kim M., Yi Y., Chun S.-H., "Superaerophobic graphene nano-hills for direct hydrazine fuel cells", *NPG Asia Materials*, 9, (2017), e378-e378.
- [35]. Yan X., Meng F., Xie Y., Liu J., Ding Y., "Direct N₂ H₄/H₂O₂ fuel cells powered by nanoporous gold leaves", *Scientific reports*, 2, (2012), 941.
- [36]. Ding J., Kannan P., Wang P., Ji S., Wang H., Liu Q., Gai H., Liu F., Wang R., "Synthesis of nitrogen-doped MnO/carbon network as an advanced catalyst for direct hydrazine fuel cells", *Journal of Power Sources*, 413, (2019), 209-215.
- [37]. Sing K.S., Williams R.T., "Physisorption hysteresis loops and the characterization of nanoporous materials", *Adsorption Science & Technology*, 22, (2004), 773-782.
- [38]. Kivrak H., Alal O., Atbas D., "Efficient and rapid microwave-assisted route to synthesize Pt-MnOx hydrogen peroxide sensor", *Electrochimica acta*, 176, (2015), 497-503.
- [39]. Chen N., Deng D., Li Y., Liu X., Xing X., Xiao X., Wang Y., "TiO₂ nanoparticles functionalized by Pd nanoparticles for gas-sensing application with enhanced butane response performances", *Scientific reports*, 7, (2017), 7692.
- [40]. Lin J., Mei T., Lv M., Zhang C.A., Zhao Z., Wang X., "Size-controlled PdO/graphene oxides and their reduction products with high catalytic activity", *RSC Advances*, 4, (2014), 29563-29570.
- [41]. Wepasnick K.A., Smith B.A., Bitter J.L., Fairbrother D.H., "Chemical and structural characterization of carbon nanotube surfaces", *Analytical and bioanalytical chemistry*, 396, (2010), 1003-1014.
- [42]. Qi B., Di L., Xu W., Zhang X., "Dry plasma reduction to prepare a high performance Pd/C catalyst at atmospheric pressure for CO oxidation", *Journal of Materials Chemistry A*, 2, (2014), 11885-11890.
- [43]. Caglar A., Kivrak H., "Highly active carbon nanotube supported PdAu alloy catalysts for ethanol electrooxidation in alkaline environment", *International Journal of Hydrogen Energy*, 44, (2019), 11734-11743.
- [44]. Eshghi A., "Graphene/Ni-Fe layered double hydroxide nano composites as advanced electrode materials for glucose electro oxidation", *International Journal of Hydrogen Energy*, 42, (2017), 15064-15072.
- [45]. Qu W., Wang Z., Sui X., Gu D., "An efficient antimony doped tin oxide and carbon nanotubes hybrid support of Pd catalyst for formic acid electrooxidation", *international journal of hydrogen energy*, 39, (2014), 5678-5688.

Removal of anionic phenol red from water solution in the batch system by using N,N-dimethylacrylamide and 3-acrylamidopropyl-trimethyl ammonium chloride-based polymeric hydrogels

Tuba Erşen Dudu

Department of Chemical Engineering, Faculty of Engineering, Van Yuzuncu Yıl University, Van, 65080, Turkey,
tuba_ersen@hotmail.com, ORCID: 0000-0001-5564-2834

ABSTRACT

p(DMAAm-co-APTMAcI)-based hydrogels were synthesized with different molar ratios by the redox polymerization technique using N,N-Dimethylacrylamide (DMAAm) and 3-acrylamidopropyl-trimethyl ammonium chloride (APTMAcI) monomers and a crosslinker. In this study, the aim was to improve the swelling properties and dye sorption of the prepared hydrogels. The equilibrium swelling values of hydrogels were determined by the gravimetric method in deionized water and different pH values, and their structural characterizations were examined with Fourier transform infrared spectroscopy (FT-IR) and thermal gravimetric analysis (TGA) techniques. Sorption efficiencies and sorption capacities of the synthesized hydrogels were determined using aqueous solutions containing phenol red dye at 25 °C. In sorption studies, the effects of different concentrations (5-50 ppm) and different pH values (2-12) on sorption were examined. When the swelling analysis in deionized water was examined, there was a significant increase in the equilibrium swelling value of p(DMAAm-co-APTMAcI)-based hydrogel as the mole ratio of APTMAcI increased. In addition, the increase in the molar ratio of APTMAcI was found to increase the phenol red dye sorption capacity and removal percentage. It was observed that p(DMAAm-co-APTMAcI) (2:8) hydrogel had maximum sorption capacity in the range of 5-50 ppm and reached 122.2 mg/g. Experimental data showed that the synthesized p(DMAAm-co-APTMAcI)-based hydrogels were effective in removing dye from wastewater and could obtain increased dyestuff removal by synthesis with different molar ratios.

ARTICLE INFO

Research article

Received: 23.09.2020

Accepted: 13.12.2020

Keywords:

N,N-dimethylacrylamide, 3-Acrylamidopropyl-trimethyl ammonium chloride, hydrogel, phenol red, sorption.

1. Introduction

Today, the increase in industrialization brings some environmental problems. Especially pollution in water has reached threatening dimensions for humans. Dyestuffs usually have synthetic origin and complex aromatic structures. They have a stable structure since they contain more than one double bond and different functional groups. This causes dyestuffs not to easily biodegrade in nature [1-3]. Approximately 700,000 tons/year of dyestuff and pigment are stated to be produced worldwide and some of these are discharged into the environment [4, 5]. This pollutant, which is discharged into the environment and water sources, disrupts the esthetic appearance of the receiving environments, reduces light transmittance and solubility of gases, affects the photosynthetic activity of the water ecosystem and has toxic effects on living organisms [6, 7]. For this reason, it is important to treat wastewater containing dyes before it is

released into the environment to minimize the negative effects on the health of humans and living organisms [6].

Different methods such as coagulation-flocculation, oxidation, ozonation, membrane separation, reverse osmosis and adsorption/absorption are used to remove these dyes from wastewater [7-11]. Among these methods, adsorption/absorption comes to the forefront due to high dye removal potential [12, 13]. Especially in recent years, interest in the use of hydrogels as adsorbents/absorbents in the treatment of wastewaters with dyestuffs has increased [14]. Hydrogels are three-dimensional polymeric network structured materials that do not dissolve in water but can swell to an equilibrium volume in aqueous environments and maintain their existing shape [15, 16]. Adsorption/absorption in hydrogels generally results from the presence of ionizable functional groups of monomers forming the hydrogel. Studies about the use of hydrogels containing various types of

functional groups as sorbents in the adsorption/absorption process have gained momentum in recent years [17].

The present study was carried out in three steps. First, p(DMAAm-co-APTMAcI)-based hydrogels were synthesized with different molar ratios (as 8:2, 6:4, 4:6, 1:1, 2:8) by the redox polymerization technique. The equilibrium swelling capacities of the hydrogels synthesized in the first stage were examined in pure water and at different pH values, and their structural characterizations were completed with FT-IR and TGA devices. In the last stage of the study, the sorption efficiency of p(DMAAm-co-APTMAcI)-based hydrogels for phenol red dye was investigated.

1. Materials and Methods

1.1. Materials and hydrogel synthesis

In this study, N, N-Dimethylacrylamide (DMAAm, 100%, Sigma Aldrich) and 3-acrylamidopropyl-trimethyl ammonium chloride (APTMAcI, 75%, Sigma) as monomers, N, N'-methylene bis acrylamide (MBA, 99%, Merck) as crosslinker, ammonium persulfate (APS, 98%, Merck) as initiator and tetramethylethylenediamine (TEMED, 99%, Merck) as accelerator were used in the preparation of p(DMAAm-co-APTMAcI) hydrogel. All chemicals used in the experiments were of analytical purity. Deionized water was obtained from 18.2 M Ω .cm (Millipore Direct-Q3 UV) and used in solution preparation, swelling and sorption experiments. Thermo Scientific pH meter (USA) and ultraviolet spectroscopy (UV-Vis, Thermo Scientific GENESYS 10S, USA) devices were used to measure pH and to quantify amount of phenol red throughout sorption, respectively.

DMAAm and APTMAcI-based hydrogels were synthesized at different mole ratios in solution medium according to the redox polymerization technique at 25 °C. MBA was used as crosslinker in the preparation of hydrogels. Typical p(DMAAm-co-APTMAcI) (1:1) synthesis was as follows: 3 mg of MBA was dissolved in 1 mL (0.0097 mol) DMAAm monomer, 1.5 mL of distilled water was added to the DMAAm/MBA mixture and mixed well at 2500 rpm. Then this mixture had 2.41 mL (0.0097 mol) APTMAcI monomer added and was mixed again. Finally, 5 μ L TEMED was used as accelerator and 100 μ L (1.94.10⁻⁴ mol) APS solution was added as initiator. Once the reaction mixture was homogeneously mixed, it was transferred to 6 mm plastic pipettes. The polymerization reaction was allowed to proceed for 4 hours at room temperature (25 °C). These preparation steps are schematically given in Figure 1. After this time period, p(DMAAm-co-APTMAcI)-based hydrogels were cut into cylinders and the cylindrical hydrogel pieces were washed by being left in DI water for three days. After the cleaning procedure, hydrogels were dried in an oven at 40 °C to a constant weight and stored for later use [18, 19].

1.2. Characterization

The synthesized hydrogels were ground and powdered and then dried in an oven at 40 °C. The structure of the dried hydrogels and bonding achieved was confirmed using a Thermo Nicolet iS10 FT-IR Spectrometer (USA) in 4000–600 1/cm range.

Thermal gravimetric analyses were conducted with Setaram Labsys Evo Gravimetric Analyzer (TGA/DSC 1600 model, France) in 50-1000 °C range, with 10 °C/min heating rate in an argon atmosphere (flow rate was kept at 100 mL/min).

1.3. Swelling behavior

Swelling characterization of synthesized polymeric hydrogels was carried out by applying dynamic swelling tests at 25 °C in deionized water to cross-linked polymeric samples. Hydrogels based on p(DMAAm-co-APTMAcI) in dry form were weighed with a sensitivity of 0.0001 g and placed in a beaker containing distilled water and left to swell. The time when the polymeric hydrogels were immersed in water was taken as $t = 0$, and the polymeric hydrogels, which were removed from the water at certain intervals, were weighed with the same sensitivity after drying the excess water on the outer surface. Weighing continued regularly until mass values which did not change over time were obtained. With the help of data obtained at the end of dynamic swelling tests, S% - t graphics were drawn and swelling isotherms were created. Equilibrium percentage swelling value was calculated according to the following equation [20-23];

$$S\% = \left(\frac{M_t - M_0}{M_0} \right) \cdot 100 \quad (1)$$

where M_0 is the initial mass (g) of the hydrogel and M_t is the mass of hydrogel at the end of time t . The swelling tests for hydrogels were performed in three replicates and their mean values were used in conjunction with standard deviation values. In order to monitor the change in equilibrium swelling value of p(DMAAm-co-APTMAcI)-based hydrogels depending on pH, hydrogels with known dry weights were put in buffer solutions prepared at different pHs (with HCl (0.1 M) and NaOH (0.1 M)) and equilibrium swelling values were calculated according to Equation 1 after 24 hours [22, 23].

Swelling kinetics curves drawn as a result of dynamic swelling tests were generally assumed to be second-order and were calculated with the following equation [24].

$$\frac{dS}{dt} = k_s \cdot (S_{\max} - S)^2 \quad (2)$$

where dS/dt is the swelling rate of hydrogels; S_{\max} is the swelling value of hydrogel at equilibrium ($g_{\text{water}}/g_{\text{hydrogel}}$); S is the swelling value at time t ($g_{\text{water}}/g_{\text{hydrogel}}$); k_s represents

swelling rate constant ($g_{\text{hydrogel}}/(g_{\text{water}\cdot\text{min}}$); and r_0 is the initial swelling rate ($g_{\text{water}}/(g_{\text{hydrogel}\cdot\text{min}}$)).

As a result of the mathematical arrangement of the equation at the boundary conditions $S=0$ for $t=0$ and $S=S_{\text{max}}$ for $t= t_{\text{eq}}$;

$$\frac{t}{S} = A + B \cdot t \quad (3)$$

In this equation, $A (=1/(S_{\text{max}}^2 \cdot k_s))$ is the opposite of the initial swelling rate ($1/r_0$) and $B (=1/S_{\text{max}})$ is the opposite of the largest swelling value [24].

The basic laws used in explaining swelling kinetics and diffusion type of polymeric structures are Fick's laws. Swelling kinetics of hydrogels with swelling properties were examined with the help of the equation below [25].

$$F = \left(\frac{M_t}{M_e}\right) = k \cdot t^n \quad (4)$$

where M_e represents the mass of hydrogels that have reached equilibrium (g); k is a specific rate constant; n is a constant which shows the diffusion exponent; and t is time (min). In order to determine the diffusion type, the parameter n must be known. The diffusion exponent n can be found from the slope of the line on the $\ln F - \ln t$ graph when swelling has not yet reached equilibrium and in the time it takes for 60% of the solvent mass to enter the gel [25].

1.4. Sorption studies

Pollutants from industries such as textile, printing, plastic, food, paper, pharmaceutical, cosmetic and leather tanning are rich in dyes. Dyes are non-biodegradable, complex organic molecules and even carcinogenic. Therefore, the discharge of these pollutants into water sources, especially, causes environmental pollution of water and soil [26, 27]. In order to explain the phenol red dye sorption quantitatively, the effects of different initial concentrations (ppm) and pH values on sorption were examined. In all sorption studies, the sorption temperature, sorption time and mixing rate were kept constant at 25 °C, 24 hours and 150 rpm, respectively. After the interaction of 50 mg dry hydrogels with 50 mL solutions containing 5-50 ppm phenol red dye concentrations, the dye concentrations in the equilibrium solution were measured. In experiments, the sorption pH was chosen as the pH of phenol red. Moreover, dry hydrogels (50 mg) interacted with 50 mL of 50 ppm phenol red solutions with pH adjusted between 2-12 using HCl and NaOH, and the amounts of phenol red in equilibrium solutions were determined. In all sorption studies, the batch technique was used, and dye sorption capacities of hydrogels were determined at 428 nm wavenumber by UV-VIS measurements. The amounts of absorbed phenol red per unit mass of the hydrogels, q_e (mg/g), were calculated by the following equation [28];

$$q_e = \frac{(C_o - C_e) \cdot V}{M} \quad (5)$$

Where C_o represents the initial concentration of phenol red (ppm); C_e is the equilibrium concentration of phenol red (ppm); V represents the solution volume (L); and M is the hydrogel mass (g).

1.4.1. Sorption isotherms

The adsorption isotherm is generally the name given to the relationship between the amount of substance sorbed by the unit mass of the sorbent at constant temperature and the concentration of the solution at equilibrium. Therefore, sorption isotherms are used to create equilibrium isotherm models and to design sorption systems [29]. In this study, experimental isotherms showing the change in sorption with concentration were created and related parameters were derived by making use of their compatibility with Langmuir (Eq. (6)) [30] and Freundlich (Eq. (7)) [31] sorption models (see Table 1 for equations).

2. Results and discussion

2.1. Characterization

FT-IR spectra of p(DMAAm-co-APTMAcI)-based hydrogels synthesized with different molar ratios are given in Figure 2. As seen in Figure 2, as the mole ratio of DMAAm monomer decreased and the mole ratio of APTMAcI monomer increased, the intensity of some peaks changed and some peaks shifted. The characteristic peaks observed at 3391 1/cm, 2932 1/cm, 1617 1/cm and 1255 1/cm for all spectra were related to N-H stretching, C-H stretching, C=O and C-N stretching, respectively. In a study by Ersen Dudu et al. (2019), it was shown that p (DMAAm) hydrogel has characteristic N-H stretching, C-H stretching and C=O stretching peaks at 3467 1/cm, 2927 1/cm and 1616 1/cm, respectively [19]. In a study by Ersen Dudu et al. (2015), it was shown that p (APTMAcI) hydrogel has characteristic N-H stretching, C-H stretching, C=O stretching and C-N stretching peaks at 3276 1/cm, 2926 1/cm, 1643 1/cm and 1480 1/cm, respectively [23]. It was determined that the obtained spectra were in agreement with the literature.

Investigation of the thermal behavior of polymeric samples is important for polymers to be selected for their intended use and location. The results of the thermo-gravimetric analysis for the characterization and thermal stability of the network structure are shown in Figure 3. Hydrogels based on p(DMAAm) and p(APTMAcI) were shown to undergo thermal degradation in one step up to 500 °C and in three steps up to 700°C, respectively [19, 23]. The results obtained in this study were compatible with the literature [19, 21, 32]. p(DMAAm-co-APTMAcI) (8:2) was stable until 229 °C; however, above 229 °C there was a substantial loss in copolymer weight. p(DMAAm-co-APTMAcI) (6:4),

p(DMAAm-co-APTMACI) (4:6), p(DMAAm-co-APTMACI) (1:1) and p(DMAAm-co-APTMACI) (2:8) hydrogels, on the other hand, did not show stable behavior against temperature increase and the first degradation occurred at 50 °C. p(DMAAm-co-APTMACI) (8:2) and p(DMAAm-co-APTMACI) (4:6) hydrogels had a total of three decay steps and a total mass loss of 53.5% occurred up to 663 °C and 100% up to 484 °C, respectively. p(DMAAm-co-APTMACI) (6:4), p(DMAAm-co-APTMACI) (1:1) and p(DMAAm-co-APTMACI) (2:8) hydrogels had a total of four decay steps and a total mass loss of 100% up to 606 °C, 95.6% up to 832 °C and 92.1% up to 731 °C, respectively. In addition, the structural resistance of the copolymers decreased with the increase in temperature as the APTMACI mole ratio increased.

2.2. Swelling behavior

In the characterization of network structured polymers with swelling behavior, it is important to examine the swelling kinetics and to clarify the diffusion type and mechanism. The swelling values and equilibrium swelling data in deionized water of the hydrogels synthesized with different molar ratios are given in Figure 4a. As seen in Figure 4a, as the APTMACI ratio in the copolymer hydrogel increased, the equilibrium swelling values of the hydrogels increased. The main reason for this is that more hydrophilic groups are present in the APTMACI monomer than the DMAAm monomer [19, 21, 33]. As a result of the calculations made using Equation 1, the highest swelling value was obtained for p(DMAAm-co-APTMACI) hydrogel prepared at a ratio of 2:8 moles and this value were found to be 10601% after 540 minutes. According to Figure 4a, the hydrogel with the lowest equilibrium swelling value was p(DMAAm-co-APTMACI) (8:2) which reached 5383% after 480 minutes.

In addition to swelling values of p(DMAAm-co-APTMACI)-based hydrogels in deionized water, which were investigated for use as dye sorption material, the swelling behaviors in different pH media were examined and the results are given in Figure 4b. According to the results, the swelling properties of the synthesized hydrogels varied depending on the pH and the swelling capacities of the hydrogels were observed to increase as the amount of APTMACI monomer, which is known to be pH-sensitive, increased. According to the experimental results, it was established that the highest swelling value was reached by p(DMAAm-co-APTMACI) (2:8) and p(DMAAm-co-APTMACI) (4:6) hydrogels. As seen in Figure 4b, maximum swelling capacities of p(DMAAm-co-APTMACI) (2:8) and p(DMAAm-co-APTMACI) (4:6) hydrogels reached 11091% and 10870% at pH 6, respectively.

The swelling rate constant (k_s), the initial swelling rate (r_0) and the theoretical equilibrium swelling value (S_{max}), which determines the swelling rate of the crosslinked hydrogels, were calculated with the help of Equation 3 and presented in

Table 2. To calculate these values, the slopes and intersections of the lines obtained by drawing $t/S - t$ graphs were used. When Table 2 is examined, the initial swelling rate for p(DMAAm-co-APTMACI) (8:2) hydrogel was smaller compared to p(DMAAm-co-APTMACI) (2:8) and p(DMAAm-co-APTMACI) (4:6) hydrogels; however, this value increased with increasing functional monomer ratio in the copolymer structure. On the other hand, another intersection is the compatibility between the theoretical S_{max} values calculated from the second-order kinetic equation and the experimental S_{max} values. This also showed the suitability of the kinetic model applied to experimental data.

Examination of the diffusion mechanism of water and determination of the relevant parameters are important in many areas where hydrogels are used. Water diffusion in hydrogels in this study was examined using Fick's Law (Equation 4). The diffusion exponential n and diffusion constant k were found by calculating the slopes and intersections of the line obtained from the $\ln(M_t/M_e) - \ln t$ graphs, respectively (Table 3). Depending on the value of the diffusion exponent, the diffusion mechanism can be explained. If $n < 0.5$, Fick-type diffusion mechanism is valid and if this value is between 0.5 and 1.0, non-Fick-type diffusion is valid [30]. When Table 3 is analyzed, n values vary between 0.52 and 0.67. In this case, swelling processes for all copolymer hydrogels could be explained by non-Fick type diffusion. In non-Fickian diffusion, diffusion rate and rinse rate are approximately the same, and swelling is controlled by both diffusion and relaxation [34, 35].

2.3. Effect of concentration and pH on sorption

It is known that hydrogels, which are crosslinked polymeric systems, are very good water holders, as well as being used as absorbents in some applications. The sorption of phenol red dye from aqueous solutions was investigated using p(DMAAm-co-APTMACI)-based hydrogels and positive results were obtained. The graph showing the percent removal of phenol red from the synthesized polymeric hydrogels is given in Figure 5a and the isotherm analyses of absorbent are summarized in Table 4. In Figure 5a, the phenol red sorption capacity of hydrogels increased, but this increase decreased after a certain concentration. In addition, p(DMAAm-co-APTMACI) (2:8) hydrogel was found to have higher phenol red sorption capacity and removal percentage than other copolymeric hydrogels. In light of the data obtained, as the amount of APTMACI monomer increased, the number of functional groups increased and as a result, the sorption capacity of the hydrogel increased. The maximum sorption capacities of p(DMAAm-co-APTMACI) (2:8), p(DMAAm-co-APTMACI) (4:6), p(DMAAm-co-APTMACI) (6:4), p(DMAAm-co-APTMACI) (1:1) and p(DMAAm-co-APTMACI) (8:2) for removal of phenol red were 122.2 mg/g, 109.7 mg/g, 95.5 mg/g, 90.7 mg/g and 68.7 mg/g, respectively.

In experiments about determining the appropriate pH value to remove anionic dyes from aqueous solutions, the equilibrium dye-holding capacities for phenol red were determined by studying in different pH media. The results are presented in Figure 5b. As can be seen from Figure 5b, the highest phenol red dye holding capacity values were obtained for all hydrogels at pH 10. In addition, it was determined that the equilibrium dye sorption capacity increased with the addition of APTMACI. Among the copolymeric hydrogels, p(DMAAm-co-APTMACI) (2:8) hydrogel had the highest phenol red sorption capacity and this value was 40.9 mg/g at pH 10. These differences observed in the sorption capacities and rates of hydrogels as the amount of APTMACI increased were due to the increase in crosslink points within the copolymer hydrogel structure and the interaction of the dye molecules and hydrophilic groups of the hydrogel.

2.3.1. Sorption Isotherm

In order to determine the sorption behavior of p(DMAAm-co-APTMACI)-based hydrogels, hydrogels of certain weights were exposed to phenol red solutions with different concentrations. With the help of the experimental data obtained, the suitability of hydrogel sorption behaviors was examined using Langmuir and Freundlich isotherms. Data for Langmuir and Freundlich isotherms are shown in Table 4. As can be seen from Table 4, all of the R^2 values calculated for the Freundlich isotherm were between 0.9683 and 0.9902 and higher than the calculated R^2 values for the Langmuir isotherm. When these results are evaluated, the sorption of phenol red dye from aqueous solutions fitted the Freundlich isotherm when p(DMAAm-co-APTMACI)-based hydrogels were used. $1/n$ is a heterogeneity parameter and is commonly applied to correlate sorption data. The smaller the value of $1/n$, the greater the expected heterogeneity [36].

3. Conclusion

In order to investigate the effect of monomer ratio on swelling and dye removal efficacy, p(DMAAm-co-APTMACI)-based hydrogels were synthesized with different molar ratios by the redox polymerization technique using DMAAm and APTMACI monomers. The presence of functional groups in the copolymer structures and their temperature sensitivity were demonstrated qualitatively and/or quantitatively by FTIR and TGA analyses. The presence of APTMACI monomer containing functional groups with hydrophilic character increased the rate of equilibrium swelling in copolymeric hydrogels and the experimental S_{max} value of p(DMAAm-co-APTMACI) (2:8) hydrogel was observed to reach 10601%. Evaluations to determine the diffusion mechanism revealed that both diffusion and relaxation control (non-Fick type) was valid for all copolymer hydrogels. In order to investigate the sorption properties of cationic hydrogels, phenol red, which has anionic property, was chosen as a model dye. The sorption properties of hydrogels

were investigated in terms of the effect of phenol red concentration, pH value and mole ratios of monomers. In the sorption experiments, the maximum sorption capacity was reached with p(DMAAm-co-APTMACI) (2:8) hydrogel and this value was 122.2 mg/g. The APTMACI monomer, which showed more hydrophilic properties in light of the obtained data, was found to increase the equilibrium sorption values of the copolymer hydrogels. As a result of evaluating the equilibrium data, it was determined that the phenol red removal process fitted the Freundlich isotherm. As a result, these copolymeric hydrogel structures have the potential to be used in various separation and purification processes, especially in environmental applications.

References

- [1]. Gong R.M., Li M., Yang C., Sun Y.Z., Chen J., "Removal of cationic dyes from aqueous solution by adsorption on peanut hull", *Journal of Hazard Mater*, 121, (2005), 247-250.
- [2]. Sudipta C., Dae S.L., Min W.L., Seung H.W., "Congo red adsorption from aqueous solutions by using chitosan hydrogel beads impregnated with nonionic or anionic surfactant", *Bioresource Technology*, 100, (2009), 3862-3868.
- [3]. Wen-Tien T., Kuo-Jong H., Hsin-Chieh H., "Adsorption of organic compounds from aqueous solution onto the synthesized zeolite", *Journal of Hazardous Materials*, 166, (2009), 635-641.
- [4]. Aksakal O., Ucun H., "Equilibrium, kinetic and thermodynamic studies of the biosorption of textile dye (Reactive Red 195) onto *Pinus sylvestris* L", *Journal of Hazardous Materials*, 181, (2010), 666-672.
- [5]. Deveci T., Unyayar A., Mazmanci M.A., "Production of Remazol Brilliant Blue R decolourising oxygenase from the culture filtrate of *Funalia trogii* ATCC 200800", *Journal of Molecular Catalysis B: Enzymatic*, 30, (2004), 25-32.
- [6]. Badu M., Boateng I.W., Boadi N.O., "Evaluation of adsorption of textile dyes by wood sawdust", *Research Journal of Physical and Applied Sciences*, 3(1) (2014), 6-14.
- [7]. Dulman V., Cucu-Man S.M., "Sorption of some textile dyes by beech wood sawdust", *Journal of Hazardous Materials*, 162, (2009), 1457-1464.

- [8]. Yang Y., Wyatt D.T., Bahorshky M., "Decolorization of dyes using UV/H₂O₂ photochemical oxidation", *Textile Chemist and Colorist*, 30, (1998), 27-35.
- [9]. Konsowa A.H., "Decolorization of wastewater containing direct dye by ozonation in a batch bubble column reactor", *Desalination*, 158, (2003), 233-240.
- [10]. Ong S.A., Toorisaka E., Hirata M., Hano T., "Treatment of azo dye orange II in aerobic and anaerobic-SBR systems", *Process Biochemistry*, 40, (2005), 2097-2914.
- [11]. Kim T.H., Park C., Kim S., "Water recycling from desalination and purification process of reactive dye manufacturing industry by combined membrane filtration", *Journal of Cleaner Production*, 13, (2005), 779-786.
- [12]. Shirsath D.S., Shrivastava V.S., "Removal of hazardous dye Ponceau-S by using chitin: An organic bioadsorbent", *African Journal of Environmental Science and Technology*, 6(2), (2012), 115-124.
- [13]. Mohsen M., Maziad N.A., Gomaa E., Hassan Aly E., Mohammed R., "Characterization of some hydrogels used in water purification: correlation of swelling and free-volume properties", *Open Journal of Organic Polymer Materials*, 5, (2015), 79-88.
- [14]. Kavaklı P.A., Yılmaz Z., Şen M., "Investigation of heavy metal ion adsorption characteristics of poly(N,N Dimethylamino Ethylmethacrylate) hydrogels", *Separation Science and Technology*, 42, (2007), 1245-1254.
- [15]. Al-qudah Y.H.F., Mahmoud G.A., Abdel Khalek M.A., "Radiation crosslinked poly (vinyl alcohol)/acrylic acid copolymer for removal of heavy metal ions from aqueous solutions", *Journal of Radiation Research and Applied Sciences*, 7, (2014), 135-145.
- [16]. Wang W.B., Huang D.J., Kang Y.R., Wang A.Q., "One-step in situ fabrication of a granular semi-IPN hydrogel based on chitosan and gelatin for fast and efficient adsorption of Cu²⁺ ion", *Colloids and Surfaces B: Biointerfaces*, 106, (2013), 51-59.
- [17]. Demirbilek C., Özdemir Dinc C., "Synthesis of diethylaminoethyl dextran hydrogel and its heavy metal ion adsorption characteristics", *Carbohydrate Polymers*, 90, (2012), 1159-1167.
- [18]. Ersen Dudu T., Alpaslan D., Uzun Y., Aktas N., "Utilization of hydrogel-fungus composites as absorbents for removal of textile dyes from aqueous media", *International Journal of Environmental Research*, 11, (2017), 557-568.
- [19]. Ersen Dudu T., Alpaslan D., Aktas N., "Urea uptake and release by novel macrogels from dimethylacrylamide", *Communications in Soil Science and Plant Analysis*, 50, (2019), 2278-2293.
- [20]. Chang C., Duan B., Cai J., Zhang L., "Superabsorbent hydrogels based on cellulose for smart swelling and controllable delivery", *European Polymer Journal*, 46, (2010), 92-100.
- [21]. Olak T., Turan A., Alpaslan D., Ersen Dudu T., Aktas N., "Developing poly(Agar-co-Glycerol-co-Thyme Oil) based Organo-hydrogels for the controlled drug release applications", *Journal of Drug Delivery Science and Technology*, (2020), <https://doi.org/10.1016/j.jddst.2020.102088>.
- [22]. Alpaslan D., Ersen Dudu T., Aktas N., "Synthesis of smart food packaging from poly(gelatin-co-dimethyl acrylamide)/citric acid-red apple peel extract", *Soft Materials*, (2020), <https://doi.org/10.1080/1539445X.2020.1765802>.
- [23]. Ersen Dudu T., Sahiner M., Alpaslan D., Demirci S., Aktas N., "Removal of As(V), Cr(III) and Cr(VI) from aqueous environments by poly(acrylonitril-co-acrylamidopropyl-trimethyl ammonium chloride)-based hydrogels", *Journal of environmental management*, 161, (2015), 243-251.
- [24]. Kundakçı S., Ögüt H.G., Üzüm Ö.B., Karadağ E., "Equilibrium swelling characterization and dye uptake studies of acrylamide-co-methylenesuccinic acid hydrogels and semi-IPNs with PEG", *Polymer-Plastic Technology and Engineering*, 50, (2011), 947-956.
- [25]. Yanfeng C., Min Y., "Swelling kinetics and stimuli-responsiveness of poly(DMAEMA) hydrogels prepared by UV-irradiation", *Radiation Physics and Chemistry*, 61, (2001), 65-68.
- [26]. Ji F., Li C., Tang B., Xu J., Lu G., Liu P., "Preparation of cellulose acetate/zeolite composite fiber and its adsorption behavior for heavy metal ions in aqueous solution", *Chemical Engineering Journal*, 209, (2012), 325-333.

- [27]. Kurniawan A., Sisnandy V.O.A., Trilestari K., Sunarso J., Indraswati N., Ismadji S., "Performance of durian shell waste as high capacity biosorbent for Cr(VI) removal from synthetic wastewater", *Ecological Engineering*, 37, (2011), 940-947.
- [28]. Maziad N.A., Mohsen M., Gomaa E., Mohammed R., "Radiation copolymerization of hydrogels based in polyacrylic acid/polyvinyl alcohol applied in water treatment processes", *Journal of Materials Science and Engineering A*, 5(11-12), (2015), 381-390.
- [29]. Kuang Y., Zhang X., Zhou S., "Adsorption of methylene blue in water onto activated carbon by surfactant modification", *Water*, 12, (2020), 587. doi:10.3390/w12020587.
- [30]. Langmuir I., "The adsorption of gases on plane surfaces of glass, mica and platinum", *Journal of the American Chemical Society*, 40, (1918), 1361.
- [31]. Freundlich H.M.F., "Über die adsorption in losungen", *Zeitschrift für Physikalische Chemie*, 57, (1906), 385-470.
- [32]. Alpaslan D., Ersen Dudu T., Sahiner N., Aktas N., "Synthesis and preparation of responsive poly(Dimethyl acrylamide/gelatin and pomegranat extract) as a novel food packaging material", *Materials Science & Engineering C*, 108, (2020), 110339.
- [33]. Alpaslan D., Ersen Dudu T., Aktas N., "Synthesis, Characterization and Modification of Novel Food Packaging Material from Dimethyl acrylamide/Gelatin and Purple Cabbage Extract", *MANAS Journal of Engineering*, 6(2), (2018), 110-128.
- [34]. Khare A.R., Peppas N.A., "Swelling/deswelling of anionic copolymer gels", *Biomaterials*, 16(7), (1995), 559-567.
- [35]. Aydınoğlu D., "Investigation of pH-dependent swelling behavior and kinetic parameters of novel poly(acrylamide-co-acrylic acid) hydrogels with spirulina", *e-Polymers*, 15(2), (2015), 81-93.
- [36]. Nethaji S., Sivasamy A., Mandal A.B., "Adsorption isotherms, kinetics and mechanism for the adsorption of cationic and anionic dyes onto carbonaceous particles prepared from Juglans regia shell biomass", *International Journal of Environmental Science and Technology*, 10, (2013), 231-242.

Modelling, sensitivity and exergy analysis of triple-pressure heat recovery steam generator

Suha Orçun Mert,^{1,2*} Zehra Özçelik,³ Ceyda Kök²

¹ İskenderun Technical University (ISTE), Department of Mechanical Eng., Iskenderun, Hatay, Turkey, orcunmert@gmail.com, ORCID: 0000-0002-7721-1629

² İskenderun Technical University (ISTE), Institute of Energy, Iskenderun, Hatay, Turkey, ORCID: 0000-0002-5536-3488

³ Ege University, Department of Chemical Engineering, İzmir, Turkey, ORCID:0000-0001-9470-4161

ABSTRACT

Related to the increasing demand for environmental pollution and electrical energy, combined cycle power plants (CCPP) are increasingly important. So, It is necessary that increasing the performance of power plants, reducing carbon emissions and rising energy production. Any change related to the heat recovery steam generator design is important for essential components of the CCPP because of directly affects the performance of it. In this study, it has explained that the modelling, sensitivity and exergy analysis of a Heat Recovery Steam Generator (HRSG) in a CCPP. In the analyzes, three-pressure HRSG was modelled with the Aspen Plus simulation program. In addition to, sensitivity analyzes were done and evaluated. Also, energy and exergy analyzes were done for each component in the CCPP.

ARTICLE INFO

Research article

Received: 11.09.2020

Accepted: 13.12.2020

Keywords:

Combined cycle power plant,
heat recovery steam generator,
Sensitivity Analysis,
Exergy Analysis,
ASPEN Plus

*Corresponding author

1. Introduction

Electric energy is a form of energy that plays an important role in sustainable development. With the increase of population and industrial use, the demand for electrical energy in developed and developing countries is increasing. Electricity; is produced in power plants where fossil fuels such as oil, natural gas and coal are used and chemical energy is converted into electrical energy. However, the use of fossil fuels causes for variety problems, such as global warming, acid rains and thinning of the ozone layer. Therefore, many energy scenarios have been realized in order to increase the performance in power plants and use clean energy. These energy scenarios include fossil fuel technologies with low environmental impact, the use of renewable energy sources and efficient use of all energy sources. The CCPP, have a significant impact on the energy scenario, due to provides sufficient load response, good flexibility at different stages, good thermal efficiency and low environmental impact compared to other fossil fuels.

CCPP consists of three main devices. These are gas turbine, heat recovery steam turbine and steam turbine generator. Gas

turbine compresses the air and mixes with high temperature fuel. And mixtures of hot air and fuel moves through with the blades of gas turbine, causing the blades to rotate. Fast rotating turbine drives the generator that converts some of the energy into electricity. The Heat Recovery Steam Generator (HRSG) generates steam from the exhaust heat of the gas turbine and transmits it to the steam turbine. The steam turbine generator produces additional electricity from excessive heat exhaust.

In conventional power plants, turbines work efficiency of 33%. But, this efficiency is 50% or more for CCPP. So it shows that they burn half a fuel less than traditional power plants to produce the same amount of energy. According to literature, work efficiency in CCPP is increased from 30% to 90% to produce useful heat and electricity from the same fuel source at the same time. Thus, while producing fewer emissions from traditional plants, it contributed to the economy by using resources more efficiently [1].

HRSG is a crucial component for meeting both the requirements of the steam turbine and the constraints of the

gas turbine. So, it should be designed to maximize the transferred heat, ensure thermal efficiency and minimize cost. Any changes in HRSG design directly affects CCPP efficiency, net power and production costs. Various gas turbines are available for different operating conditions, such as exhaust gas and back pressure. For selected gas turbine, steam turbine and HRSG must work in accordance. Also, efficiency of the steam cycle largely depends on the HRSG design.

Operating at a temperature of about 650 °C and 13-20 MPa pressure, HRSG recovers heat from the gas turbine exhaust to produce steam. Although flow loop systems developed, heat recovery steam systems are implemented under subcritical conditions [2].

Advanced multi-pressure HRSGs are preferred due to provide high efficiency despite their high cost. Thermal efficiency is being increased by adding two or three parallel steam streams for high, intermediate and low pressure stages of steam turbines.

HRSG has been studied in many ways in the literature in recent years. Pressure level selection [3], modeling and design [4], effect of heat transfer surface on thermal performance [5] extensively studied. Also, the application of the genetic algorithm in a structural sense [6], application of thermodynamic and thermo-economic approaches for parameter design [7] has attracted attention in recent years. Exergy, environmental and economic analysis has been performed for CCCP. [8].

Today, HRSG with three pressure levels combining steam and gas turbines is considered the latest technology. Since HRSG has a major impact on the thermal efficiency of the steam cycle, many studies have been conducted on this subject [9,10]. Pelster et al. compared CCPP efficiency results of double and triple pressure HSRGs and steam reheat models [11]. Optimization of single, double and triple pressure HRSGs to improve heat recovery and exergy efficiency in CCPPs made by Sirinas et al. [12]. Ahmadi et al. made the thermodynamic analysis of double pressure HSRG. They used the multi-purpose optimization method to find the best design parameters. The functions considered for optimization are cost and exergy efficiency [13]. Three pressure CCGT optimizations were carried out by Alus and Petrovi. While optimizing Alus and Petrovi, they aimed to minimize the cost of electricity generation at the CCGT plants [14]. Alobaid et al. with real power plant data, three pressure HRSGs were created in detail in a digital model with Aspen Plus. Also these authors evaluated the control structure with Aspen Plus Dynamics [15]. Ali et al. performed energy and exergy analysis with triple pressure HRSGs. As a result of calculating the exergy destructions for each component of the HRSG, it was determined that high pressure components have higher exergy destruction than low pressure components [16].

Moosavi et al. In the hot summer, HRSG proposed a new method to improve performance. As a result, HSRG exergy destruction increased due to the high temperature difference in the flows, despite the increase in net power [17]. Boyaghchi et al. used sensitivity analysis to examine the effects of compressor pressure ratio. They observed that thermal and exergy efficiency increased when the compressor pressure ratio increased [18].

In this study; exergy analysis of the HRSG that three levels of pressure are applied has been comprehensively analyzed. Energy and exergy analyzes were performed for each component in CCPP. At the same time, the three-level HRSGs system was modeled with Aspen Plus software and sensitivity analysis was performed.

2. Modeling and simulation

2.1. Modeling in ASPEN PLUS

Advanced System for Process Engineering software (ASPEN) is used to model advanced system power plants. It is a software program developed in 1981 in collaboration with the Massachusetts Institute of Technology (MIT) and the United States Department of Energy [19].

ASPEN Plus simulation program; analyze the behavior of the process by making use of engineering relations such as chemical balance, mass and energy balances, reaction kinetics. True plant analysis can be simulated thanks to realistic operating conditions and thermodynamic data. This program helps to increase the efficiency of existing facilities and design better facilities.

ASPEN Plus; used to analyze fluid configurations and find new alternatives. In addition, results can be obtained in the form of PFD-style drawings, reports, graphs and spreadsheets.

2.2. Exergy Analysis

The first law of thermodynamics is required in the analyzes to evaluate energy efficiency. But, it does not give a complete conclusion about the potentials and limitations of use of various components of energy system analyzed by this law. This situation, impairs compatibility in design and manufacturing. Exergy is the maximum amount of energy it can absorb from any energy source.

Exergy or available energy refers to the most useful work a system can do when it comes to balance with its environment. However, the second law of thermodynamics, or exergy analysis, gives better results in the design and performance analysis of energy systems. Therefore, exergy is a measure of the system's potential to do business for a particular environmental state. Exergy analysis has gained great importance in the evaluation and design of thermal systems.

Exergy is not generally protected. Conversely, it disappears because of the irreversible situations in the system. In light of these, a general exergy analysis reveals how much energy loss occurs in the system and where it occurs. Thus, thermodynamic inefficiencies within the system are revealed. [20].

2.3. Modeling Sensitivity Analysis

Sensitivity analysis is performed to measure the effects of mathematical modeling or changes in system parameters on system outputs or performance. In short; sensitivity analysis is used to distribute changes in the outputs of a system to uncertain different sources in its inputs. One of the system parameters is changed at a certain rate while other parameters are fixed. And after the system is started, the percentage change of the predetermined system parameters is observed. Sensitivity analysis is used to investigate the robustness, accuracy of model results and to understand. Also, it examines the relationships between input parameters and performance of a system or model. Monitoring the change of model parameters is very important in determining the system inputs, which leads to uncertainty in system performance. Therefore, sensitivity analysis is given importance to eliminate the uncertainty of the parameters and increase the reliability of the system [21].

While responsiveness blocks have no effect on basic simulation, they provide additional information to the basic case results. Simulation, on the other hand, operates completely independently of sensitivity analysis. Multiple variable precision blocks for each value combination form a row in the sensitivity table. And these blocks form loops so that they are evaluated only once for each line in the sensitivity table. Aspen Plus program sorts the blocks automatically.

3. Case study

Figure 1 shows typical triple pressure HRSG. HRSGs are multi-pressurized with channel firing and other features, and can become more complex. This diagram shows main gas, steam and condensate flows, HRSG surfaces and steam drums. Flue gas comes from combustion turbine and enters HRSG, and then decreases its temperature by passing through heater, reheater, drum evaporator surfaces and economizer. The condensate comes from the combined cycle condenser and flows into the economizer drum. This steam first flows to the superheater then to high-pressure turbine. After high pressure turbine, it flows back to heater and intermediate pressure turbines. Important design parameters of HRSG are pinch points and approach temperatures. Reducing temperature helps increase cycle efficiency. Also, it includes optimization, complex heat transfer calculations and steam cycle heat balances to avoid operational problems.

Modeling a thermal system consists mainly in the calculation of its operating variables, in principle for a given stationary state. The detailed modeling and simulation of the HRSG is a complex problem, depending on several variables.

The operating parameters can be determined by means of both a thermodynamic and exergetic analysis [22]. ASPEN Plus was used for the calculation and evaluation of all results. Mass, energy, exergy and design equations and thermodynamic properties were enabled using related operating variables. These calculations were done for a steady state process at 15 C and 27% RH and the content of the used fuel gas was 82% CH₄, 10% C₂H₆, 2.2% C₃H₈, 2% C₄H₁₀, 0.8% C₅H₁₂, 2% CO₂, 1% N₂ as molar basis. Figure 1 shows the configuration of the HRSG designed with the ASPEN Plus Simulation Program.

3.1. Exergy Calculations

As with energy, exergy in any current can be divided into different components. When nuclear effects, magnetism, electricity, and surface tension are ignored, exergy (E):

$$E = E_k + E_p + E_{phy} + E_{ch} \quad (1)$$

It is defined as. In this equation, additional kinetic exergy corresponds to E_p potential exergy, E_{ph} physical exergy, E_{ch} chemical exergy. Kinetic and potential exergy are not taken into account. Physical exergy is defined as the maximum work achieved when a substance with a certain temperature and pressure in a current reaches the reference state through physical processes involving heat processes. Chemical exergy arises from the difference between the content of the current and the reference state [20].

$$E_{phy} = (H_1 - T_0 S_1) - (H_0 - T_0 S_0) \quad (2)$$

$$E_{ch} = E_{ch}^o + \sum(x \ln(x)) \quad (3)$$

In an isolated steady control volume, exergy balance occurs as follows:

$$E_i = E_o + W + E_D \quad (4)$$

Where, E_i exergy entering the system, exergy exiting from the E_o system, W is the transfer of work between the system and the environment, and E_D is the exergy destroyed in the system. Considering these techniques, exergy calculations were made in gas turbines, waste heat boilers and steam turbines on one of the two energy blocks in the combined cycle power plant. The reference state was chosen for this study in general atmospheric content (21% O₂, 79% N₂) at 20°C and 1 atm. Figure 2 shows basic combined cycle schematization.

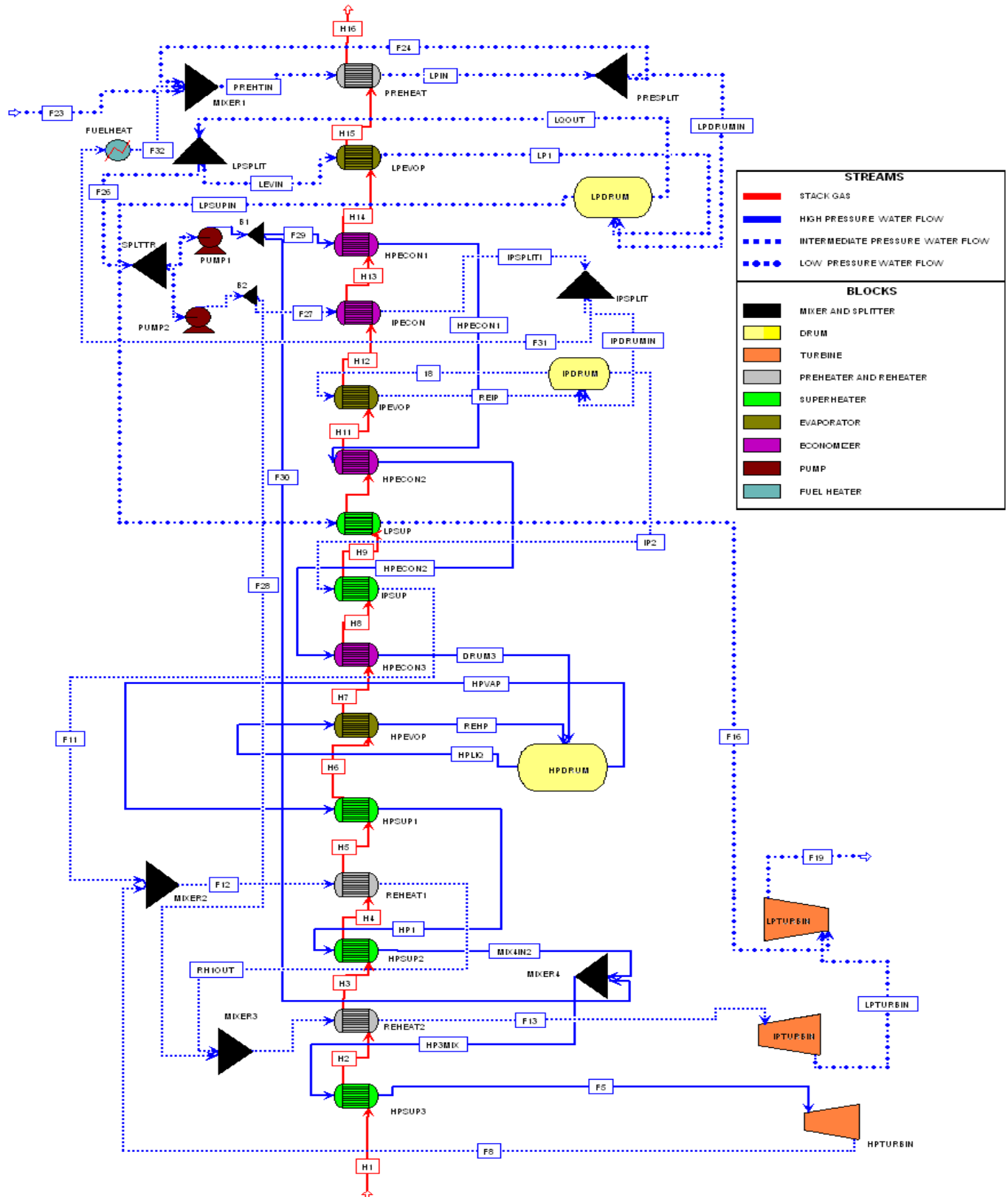


Figure 1. Heat Recovery Steam Generator Configuration

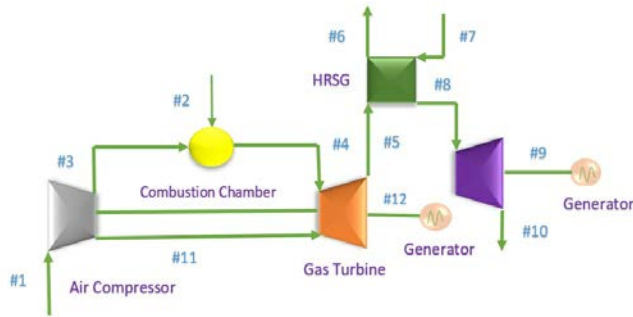


Figure 2. Basic Combined Cycle schematization

3.1.1. Gas Turbine

Gas turbine basically consists of three parts. These are; Compressor for air to be used in combustion and cooling; combustion chamber, section where the fuel is burned with compressed air and turbine.

Compressor: The air to be used in the combustion chamber is compressed in the compressor. The incoming air comes in atmospheric conditions (T = 293.15 K, P = 1 atm). The compressor works with 1/14 compression ratio. Equations (5) and (6) are used in compressor calculations.

$$E_1 + E_{11} = E_3 + E_D \tag{5}$$

$$\eta = (E_3 - E_1) / (E_{11}) \tag{6}$$

Combustion Chamber: It is accepted that full combustion occurs in the combustion chamber. Temperature, pressure and flow values were taken under operating conditions. The exergy of the fuel was calculated using (3) and (4). Calculations in the combustion chamber are made by using equations (7) and (8).

$$E_3 + E_2 = E_4 + E_D \tag{7}$$

$$\eta = E_4 / (E_3 + E_4) \tag{8}$$

Turbine: The turbine has an expansion up to approximately atmospheric pressure (1,044 bar), and the outlet temperature is 900 K, which is the operating condition. Input features are taken as T = 1570 K and P = 14 barg.

Table 1. The temperature and enthalpy changes in HRSG

		Energy Transfer Rate /Hot and Cold Stream [MW]	Gas side Enthalpy change [MW]	T _{gas i} [K]	T _{gas o} [K]	T _{steam i} [K]	T _{stm o} [K]
Unit 14	Superheater HP	954.9	954.9	899.0	861.9	763.8	841.5
Unit 8	Preheater	2832.5	2832.5	861.9	797.6	713.0	838.3
Unit 13	Superheater HP	1081.6	1081.6	797.6	757.7	683.0	767.9
Unit 7	Preheater	2492.0	2492.0	757.7	696.7	618.3	739.0
Unit 12	Superheater HP	1037.1	1037.1	696.7	657.2	598.7	683.0
Unit 11	Evaporator HP	4.6	4.6	657.2	654.6		

$$E_4 = E_{11} + E_5 + E_6 \tag{9}$$

$$\eta = (E_{11} + E_6) / (E_4 - E_5) \tag{10}$$

3.1.2. Heat recovery steam generator

Hot steam is produced at three different pressures in HRSG. These are LP (4.3 bar), IP (25 bar), HP (122 bar). For this, 15 different modules with different tasks are used. These modules work as heat exchangers or evaporators. These modules and in general, calculations for HRSG (11) and (12) were used.

$$E_5 + E_7 = e_6 + E_8 \tag{11}$$

$$\eta = (E_7 - E_8) / (e_6 - E_5) \tag{12}$$

3.1.3. Steam Turbine

There are three separate steam turbines operating on the same axle was used in the analysis for these. 838 K and 122 bar for HP, whose input conditions are operating values, 835 K for IP and 25.5 bar and finally 564 K and 5 bar for LP were taken. Output values are 624 K for HP and 566.5 K for 29.4 bar IP and 314 K and 0.0077 bar for 5 bar IP.

4. Results

4.1. Exergy Analysis Results

As a result of the calculations, the exergy values, exergy losses and efficiency at the inputs and outputs of the combined cycle equipment analyzed were done.

Table 1 assumes that the temperature does not change horizontally for HRSG gas side and temperature and enthalpy change values are calculated using energy balances. Gas side nomenclature is used for combustion products. In the combustion chamber, full combustion is accepted and the content of combustion products is 0,11 O₂ in mole fraction; 0,78 N₂; It was calculated as 0,04 CO₂ and 0,07 H₂O and used. In energy calculations, combustion products were considered ideal and enthalpy and entropy values were calculated under these conditions.

Unit 15	Economizer HP	885.4	885.4	654.6	617.9	547.7	596.7
Unit 6	Superheater IP	151.1	151.1	617.9	602.7	496.0	583.5
Unit 3	Superheater LP	351.0	351.0	602.7	579.5	424.0	559.4
Unit 10	Economizer HP	772.6	772.6	579.5	545.3	498.9	547.7
Unit 5	Evaporator IP	0.1	0.1	545.3	544.9		
Unit 4	Economizer IP	202.2	202.2	544.9	527.2	420.2	490.0
Unit 9	Economizer HP	1758.7	1758.7	527.2	474.9	422.2	498.9
Unit 2	Evaporator LP	0.2	0.2	474.9	474.4		
Unit 1	Preheater	3521.6	3521.6	474.4	401.0	333.0	416.0

Table 2 shows the exergy changes on the gas side and steam side in the modules. In general, exergy losses arising from heat transfer can occur, but the large differences calculated may have occurred from the acceptance of ideal gas conditions in the calculations of the gas side.

Another high loss is seen in HRSG. However, as mentioned earlier, this value was high due to calculation methods. In fact, this value is expected to be 3-5%.

Table 2. The exergy changes

Units	1	2	3	4	5	6	7	8	9	10	11	12	13	14	15
Gas side [MW]	71,8	1,3	16,0	14,7	1,7	11,1	35,9	36,6	44,6	26,0	29,7	29,9	36,6	21,8	26,0
Water / Steam Side[MW]	11,2	1,0	1,2	1,1	0,7	1,0	13,5	18,0	8,9	7,3	1,1	15,3	10,2	9,6	30,6

Table 3. The efficiency and loss values

Unit	Efficiency (%)	Loss (E _F)%	Loss for a Block (E _F)%
Compressor	2,0	73,6	2,0
Turbine	93,2	6,8	3,0
CC	7,3	1,1	30,5
HRSG	38,3	61,7	22,4
HP St. Turbine	96,4	3,6	0,1
IP St. Turbine	93,7	6,3	0,4
LP St. Turbine	72,6	27,4	1,7
Chimney			12,3
Overall	28,52	71,5	72,3

Combustion products entering HRSG, as can be seen in Figure 3, lose their exergy during HRSG and their temperature decreases. The final value reveals the magnitude of the exergy lost with the combustion products coming out of the 123 MW chimney. The lower this value, the higher the efficiency, but the chimney outlet temperature value cannot be reduced too much against the condensation risk of water vapor in the combustion products mixture.

4.2. Sensitivity Analysis Results

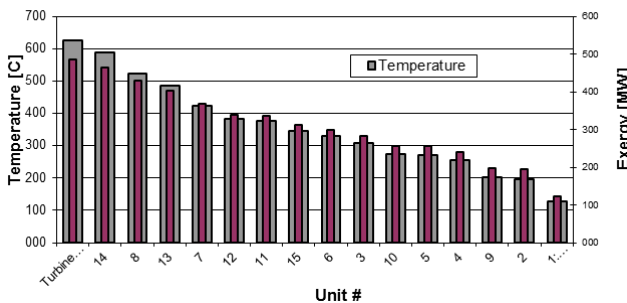


Figure 2. The Exergy and Temperature Change Through the HRSG

After the exergy calculations, exergy efficiency calculations and exergy losses are calculated in comparison to fuel exergy and are shown in Table 3. As can be seen, the highest exergy loss occurs in the combustion chamber. This value complies with the source values and continues to be a general problem of power plants. The improvements that can be made in this section will affect the total efficiency at a high rate and will support the more efficient use of energy, which is the problem of our age.

Figure 4 shows the produced power of three different pressure steams versus inlet water flowrate. At the same range intermediate pressure steam production is higher than the others. The second axis on the same graph is the chimney outlet temperature versus water flow rate graph. According to this result, high water flowrates reduced the outlet gas temperature. So, steam production increases simultaneously.

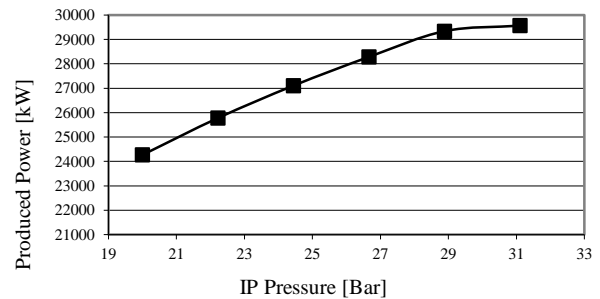


Figure 4. Effect of water inlet flowrate on the produced power and outlet gas temperature

The main results of this study is the produced power amounts when changing the pressures for different type of steams. Figure 5 shows how the intermediate pressure vapor cavities affect the amount of power generated. The result showed that the production amount remained constant after the amount of generated power increased to 29 bar. For electricity generation, the upper middle pressure range can be determined as 29 or 300 bar.

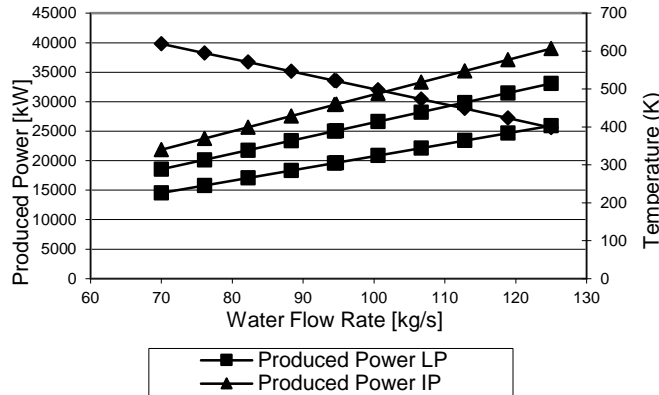


Figure 5. Variation of IP steam pressures on the produced power

The effect of HP steam pressure for the produced power is given in Figure 6. It is seen that with increasing the pressure rises the amount of power produced. The upper limit can be defined from users considering the efficiency of other units.

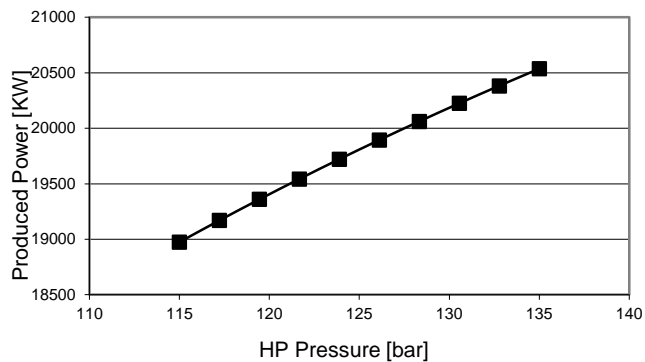


Figure 6. Variation of HP steam pressures on the produced power

Figure 7 shows that the variation of LP steam pressures on the produced power. Different behavior can be observed for this type of steam. Up to 5.5 bar, produced power amount increases, between 5.5 and 6 bar, small amount decreases, then produced power amount is constant. Using these sensitivity results, definite ranges for the system is selected.

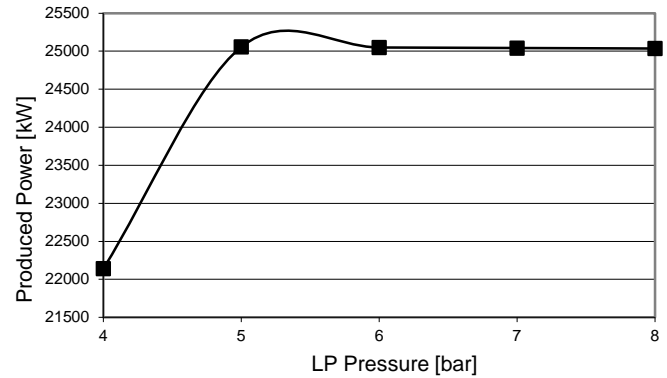


Figure 7. Variation of LP steam pressures on the produced power

Figure 8 shows the effect of LP drum vapor fraction on the produced power and outlet gas temperature. What the lines represent is shown in Figure 1.

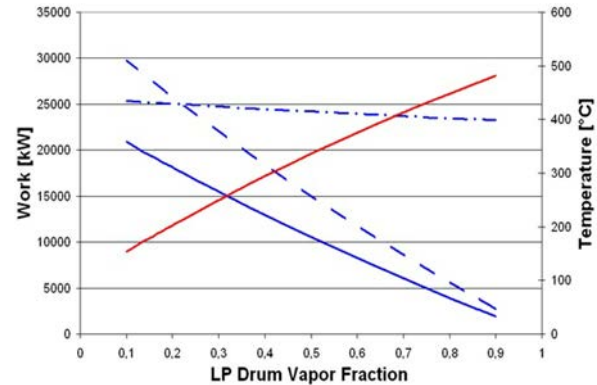


Figure 8. Effect of LP drum vapor fraction on the produced power and outlet gas temperature

5. Conclusion

In this study modelling, sensitivity and exergy analysis of a HRSG in a CCPP has been applied. The Three-pressure HRSG was modelled with Aspen Plus simulation program and sensitivity analysis was performed. At the same time, energy and exergy analyzes were made for each component in the CCPP.

A careful evaluation of processes using the concept of exergy enables us to identify the source of inefficiencies. By identifying the most wasteful processes, we are able to redesign the system to achieve the maximum possible savings. Often these improvements can lead to considerable savings.

From the results it is clear that the exergy and temperature of the hot gases in the HRSG decreased throughout the pot. In addition, a significant amount of exergy is transferred to the water/steam system. At the same time, exergy change has been shown depending on different aspects of HRSG. According to this result, it is understood that the exergy lost

on the gas side is not completely transferred to the water/steam side, but disappears.

The main reason of the losses in combustion chamber is raised from the relatively low firing temperature and if the construction material will resist much high temperature the efficiency of the system will rise.

Moreover the loss in the HRSG is causing from the heat transfer from combustion gases to water/Steam system and also the loss in the chimney is caused from the temperature of nearly 100°C. But this temperature cannot be pulled down since the combustion gases contains considerable amount of water vapor and if the temperature is allowed to be lower than 100°C condensation will occur and the system will fail so this loss is a compulsory one.

So by the exergy analysis it is seen that the exergy destruction (energy loss) is occurs at the combustion chambers with 30%, the HRSG with 22 % and from the chimney with 12,4 %. So, the efficiency of the power plant mostly depends on the efficiency of these equipments so any improvement on these equipments will increase the overall efficiency of the plant noteworthy.

It is seen that the effect of HP and IP pressure is more crucial from the produced power point of view from sensitivity analysis whereas the exergy efficiency reaches 28.2% overall. The tendency of the gaining higher efficiencies are still in the scope of the researchers and engineers.

References

- [1]. Kole A., "A review and study on advanced control and automation functions and future control for a modern combined cycle power plant", 2016 International Conference on Intelligent Control, Power and Instrumentation, (2017), 215-220.
- [2]. Rackley S.A., "Carbon capture from power generation. In: Carbon Capture and Storage" (2017).
- [3]. Nadir M., Ghenaiet A., "Thermodynamic optimization of several (heat recovery steam generator) HRSG configurations for a range of exhaust gas temperatures" Energy, (2015),685-695.
- [4]. Dumont M.N., Heyen G., "Mathematical modelling and design of an advanced once-through heat recovery steam generator", Computers and Chemical Engineering, (2004),651-660.
- [5]. Feng H., Zhong W., Wu Y., Tong S., "Thermodynamic performance analysis and algorithm model of multi-pressure heat recovery steam generators (HRSG) based on heat exchangers layout", Energy Convers Manag, (2014), 282-289.
- [6]. Durán M.D., Valdés M., Rovira A., Rincón E., "A methodology for the geometric design of heat recovery steam generators applying genetic algorithm". Appl Therm Eng, (2013),77-83.
- [7]. Naemi S., Saffar A.M., Behboodi K.S., Mansoori Z., "Optimum design of dual pressure heat recovery steam generator using non-dimensional parameters based on thermodynamic and thermoeconomic approaches" Appl Therm Eng, (2013), 371-384.
- [8]. Mohammadi K.A., Joda F., Bozorgmehry R., "Exergic, economic and environmental impacts of natural gas and diesel in operation of combined cycle power plants", Energy Convers Manag, (2016), 103-112.
- [9]. Manassaldi J.I., Arias A.M., Scenna N.J., Mussati M.C., Mussati S.F., "A discrete and continuous mathematical model for the optimal synthesis and design of dual pressure heat recovery steam generators coupled to two steam turbines", Energy, (2016), 807-823.
- [10]. Martelli E., Elsidio C., Mian A., Marechal F., "MINLP model and two-stage algorithm for the simultaneous synthesis of heat exchanger networks, utility systems and heat recovery cycles", Comput Chem Eng, (2017), 663-689.
- [11]. Pelster S., Favrat D., Von M.R. "The thermoeconomic and environomic modeling and optimization of the synthesis, design, and operation of combined cycles with advanced options", J Eng Gas Turbines Power, (2001),717-726.
- [12]. Srinivas T., Gupta A., Reddy B. V., "Thermodynamic modeling and optimization of multi-pressure heat recovery steam generator in combined power cycle" J Sci Ind Res, (2008).
- [13]. Hajabdollahi H., Ahmadi P., Dincer I., "An Exergy-based multi-objective optimization of a heat recovery steam generator (HRSG) in a combined cycle power plant (CCPP) using evolutionary algorithm" Int J Green Energy, (2011), 44-64.
- [14]. Alus M., Petrović M .V., "Optimization of the triple-pressure combined cycle power plant",Therm Sci, (2012),901-914.
- [15]. Alobaid F., Karner K., Belz J., Epple B., Kim H.G., "Numerical and experimental study of a heat recovery steam generator during start-up procedure", Energy, (2014), 1057-1070.
- [16]. Ali M.S., Shafique Q.N., Kumar D., Kumar S., Kumar S., "Energy and exergy analysis of a 747-MW combined cycle power plant Guddu", Int J Ambient Energy, (2018),1-10.

- [17]. Moosazadeh S.A., Mafi M., Kaabi N.A., Salehi G., Torabi A. M. "A new method to boost performance of heat recovery steam generators by integrating pinch and exergy analyses" *Adv Mech Eng*, (2018).
- [18]. Boyaghchi F.A., Molaie H., "Sensitivity analysis of exergy destruction in a real combined cycle power plant based on advanced exergy method" *Energy Convers Manag.* (2015),374-386.
- [19]. Sabia G., Heinze C., Alobaid F., Martelli E., Epple B., "ASPEN dynamics simulation for combined cycle power plant – Validation with hot start-up measurement" *Energy*, (2019).
- [20]. Kakaras E., Doukelis A., Leithner R., Aronis N., "Combined cycle power plant with integrated low temperature heat (LOTHECO)", *Applied Thermal Engineering*, (2004),1677-1686.
- [21]. Balaman Ş.Y., "Uncertainty Issues in Biomass-Based Production Chains", *Decision-Making for Biomass-Based Production Chains*, (2019),77-112.
- [22]. Bassily A.M., "Modeling, numerical optimization, and irreversibility reduction of a triple-pressure reheat combined cycle", *Energy*, (2007),778-794.

Dye removal from synthetic and dye bath wastewater by electrocoagulation method and isotherms

Tuba Öztürk,^{1,*} Hande Akbaş,¹ Gülşen Aydın Keskin²

¹ Department of Environmental Engineering, University of Tekirdag Namik Kemal, Corlu, Tekirdag, 59860, Turkey, ozturk_tuba@yahoo.com, ORCID: 0000-0003-1851-6120

² Department of Industrial Engineering, University of Balikesir, Balikesir, 10145, Turkey, ORCID: 0000-0001-6639-1882

ABSTRACT

In this study, treatment of wastewaters containing Setazol Black TNN, which is a reactive diazo dyestuff that is prevalently used in dyeing natural fibers in the textile industry, by the electrocoagulation method was examined. Experiments investigating the effectiveness of Al and Fe electrodes in treatment of real wastewaters collected from the dye bath of a yard dyeing facility and synthetic wastewaters prepared with Setazol Black TNN used in this bath were carried out by determining the optimum treatment conditions. The optimum current, pH and initial dye concentration in the synthetic wastewaters for the Al electrodes were 8 ampere (A), 7.57 and 50 mg/L, respectively, while these for the Fe electrodes were 8A, 9 and 100 mg/L, respectively. The optimum current, pH and thinning rate were seen in the dye bath wastewaters for the Al electrodes as 8A, 8 and 1/60 and for the Fe electrodes as 8A, 9 and 1/30, respectively. While carrying out the experiments using these experimental conditions, color and Chemical Oxygen Demand (COD) removal from the synthetic wastewaters and the dye bath wastewaters with long-running treatments was investigated. As a result of the treatment experiments, removal efficiencies of 96% and 57% respectively for color and COD for the Al electrodes and 99% and 61% for the Fe electrodes in the synthetic wastewaters, 87% and 55% for the Al electrodes and 89% and 55% for the Fe electrodes in the dye bath wastewaters were obtained. With this study, it was aimed to reveal not only the position and effectiveness of the treatment process for wastewaters containing intense color but also the effects of chemicals used in dye baths on removal efficiency. Moreover, it was determined that the Langmuir isotherm model was more convenient for the experimental data in the process. In the last part of the study, a correlation analysis was carried out between the color and COD removal efficiencies. Besides, the efficiencies for the use of Al and Fe electrodes respectively for both color and COD removal were compared, and comments were made for different groups by one-way ANOVA..

ARTICLE INFO

Research article

Received: 10.09.2020

Accepted: 13.12.2020

Keywords:

Correlation,
electrocoagulation,
isotherms,
one-way ANOVA,
reactive azo dye

*Corresponding author

1. Introduction

Wastewater constitutes the greatest environmental problem in the textile industry. Washing wastewater, process wastewater, cooling waters and rainwater are the main components of wastewater flows [1,2]. Process wastewaters in the sector originate to a significant extent from dyeing processes [2]. Wastewaters emerging from dyeing operations contain assistive chemicals such as residual colorants, inorganic salts, alkalis and surface-active substances and various byproducts [1-5]. The main group of pollutants in this wastewater flow is usually synthetic dyestuffs which have a high molecular weight, complex chemical structure and low biological solubility [1,2,6]. Reactive dyestuffs which contain a reactive group in their structure constitute the most significant and

greatest dyestuff class for the sector [1,7]. Reactive dyes are water-soluble anionic chemicals that react with functional groups and have high durability for wet processes such as washing and rubbing which can be rapidly covalently bonded to textile fibers in the presence of alkaline conditions [1,7,8]. Dyeing with these dyes is the result of covalent bond formation between the carbon atom of the coloring molecule and the sulfur, nitrogen or oxygen atom of the thiol, amino or hydroxyl group in the polymer creating the fiber [7,9]. Reactive dyestuff molecules contain four significant structural classes as the chromogen, water-solubilizing, reactive and bridging groups. Chromogens from these groups give the molecule its color and have a direct effect on the properties of the dye such as light fastness. For reactive dye molecules to be able to bond with textile fibers, they need to be water-

soluble. For this purpose, reactive dyes contain ionic groups such as one or more sulfonates that provide solubility in an aqueous environment. Reactive groups are some of the most fundamental structural groups of reactive dyes. These structures are specific groups that react with the textile fiber and provide bonding by establishing chemical bonds. Bridging groups are structures that are mostly constituted by amino groups which are used to bond the chromogen part of the dye molecule and the reactive group [9].

Dyes are also chemically named based on the chromogen groups in their structure which are unsaturated functional groups and create color by absorbing light in the ultraviolet region [6,10]. One of the most important chromophore groups used in dyes is the azo group, and dyes containing this chromophore structure are known as azo dyes. Approximately 80% of azo dyes, which constitute about 60-70% of all dyes that are produced, are used in the textile industry. Azo dyes are mostly aromatic but sometimes aliphatic or aliphatic-aromatic compounds that contain one or more azo groups (N=N) in their chromophore structures. The most important azo dyes are monoazo dyes that contain a single azo group in their structure [10-12]. Azo dyes are a large class of synthetic dyes that can provide color in a dense and broad tone range, can be synthesized relatively easily and with low costs with desired properties such as high light and washing fastness and contain more than 2000 chemical substances with high water-solubility [10,12,13].

The properties of dyes that are the reasons for their commercial preference make these dyes a great problem in the environmental sense. Reactive dyes, which constitute the largest dye class based on application methods, are the most environmentally problematic dye class which consumes the most water per unit fiber and leads to the discharge of most salts, alkalis, etc. per unit fiber among all dyes [5]. Azo dyes which constitute the most significant reactive dyes are those that are resistant to degradation. These dyes usually cannot be removed with classical treatment methods and are found with unchanged chemical structures in the output waters of treatment facilities. Azo dyes, which increase their concentration in nature by accumulation due to these properties, are also known as toxic chemicals that have mutagenic and carcinogenic effects. Removal of dyes, especially those containing an azo group in their chromophore structures, carries great importance especially because of their potential harms on human and environmental health [12,14,15].

This study examined the treatability of wastewaters belonging to the most intense pollutant-containing process of the textile industry, which is accepted as one of the most pollutant sectors all over the world, with the electrocoagulation method. In the experiments conducted with two different electrode materials as Al and Fe and two different wastewaters as synthetic wastewater (SW) and dye bath wastewater (DBW), it was

firstly aimed to determine the parameters effective on the treatment process that was used. After determining the optimum treatment conditions with 30-minute short-term experiments, 300-minute long-term experiments were carried out using the current and pH values at which the highest removal efficiency was achieved. This way, the efficiency of the electrocoagulation method was examined not only in terms of color but also about COD for the SW and the DBW containing concentrated dyestuffs and additional chemicals.

2. Materials and methods

2.1. Experimental procedure

The study was carried out with authentic wastewaters taken from the yarn dyeing bath of a facility that operates in the fields of yarn dyeing, fabric dyeing and fabric printing in the borders of the province of Tekirdağ, which is one of the most significant provinces of Turkey in terms of the textile industry, and synthetic wastewaters. Setazol Black TNN is a reactive diazo dye that is mostly used in dyeing natural fibers. The chemical structure of the dye whose chemical name is tetrasodium 4-amino-5-hydroxy-3,6-di [[4-[[2-(sulfonate oxy) ethyl] sulfonyl] phenyl] azo] naphthalene-2,7-disulfonate is given in Figure 1.

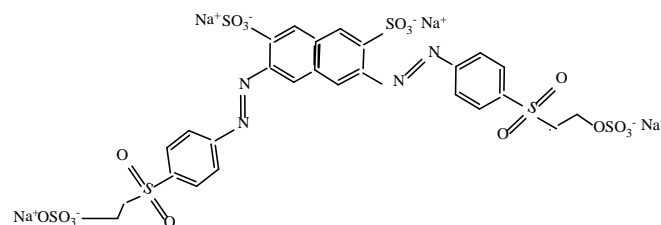


Figure 1. Chemical structure of Setazol Black TNN.

At yarn dyeing baths, based on the recipes prepared according to the type of the yarn and the dyestuff to be used, the fiber is prepared for the dye, bonding of the dye with the fiber is made easier, and impurities in the medium are eliminated. Table 1 presented the characteristic properties of SW and DBW.

Table 1. Electrocoagulation reactor input values of the samples

Parameter	Synthetic Wastewater (SW)
COD (mg/L)	1400
pH	7.70
Conductivity (mS/cm)	2.94

The electrocoagulation reactor in which the treatment study is carried out had a volume of approximately 3 L. Al and Fe electrode groups consisting of 14 parallel plates were used in the reactor. In these electrode groups, electrodes, each 2 mm thick, were placed 3 mm apart.

2.2. Analyses

In the study, color, measurements were made at three different wavelengths as 436, 525 and 620 nm with the help of a spectrophotometer (Aquamate Thermospectronic/US) [16]. COD analysis was carried out in a thermoreactor (Spectroquant TR-620/Germany) by using the method titled 5220 C "Close Reflux, Titrimetric Method" [17]. given in the Standard Methods. All experiments were conducted at room temperature, and the pH values of the specimens were adjusted by using 0.1 N H_2SO_4 and 0.1 N NaOH.

3. Results and discussion

At the first stage of the two-stage study, the color removal efficiencies of the Al and Fe electrodes for SW and DBW were examined. First of all, the optimum experimental conditions for the parameters as current, pH and initial dye concentration which are effective on the process yield for these two wastewaters and two electrode materials were determined. At the second stage of the study, using these optimum experimental conditions, the long-run treatment of these DBW and SW was examined by monitoring color and COD removal. This way, it was aimed to determine the dye removal efficiency of the electrocoagulation method and the effects of additional chemicals used at dyeing baths on removal efficiency.

3.1. Effect of current

When the reaction time is kept constant, the current that is applied becomes directly effective on the amounts of ions leaving the electrodes. Based on metal ions, the current controls important operational parameters such as the coagulant production rate, reaction speed, duration, size of the gas bubbles that are produced and size of the flocs. This way, it directs the progression of the process and determines the removal efficiency and operational cost of electrocoagulation [18-20]. The experiments where the optimum current was examined for the Al and Fe electrodes were carried out at room temperature (21°C) under 3, 5, 8 and 10 ampere current at a dye concentration of 50 mg/L and natural pH (7.57) for SW and with specimens diluted by 1/60 at natural pH (9.32) for DBW (Figure 2a-b).

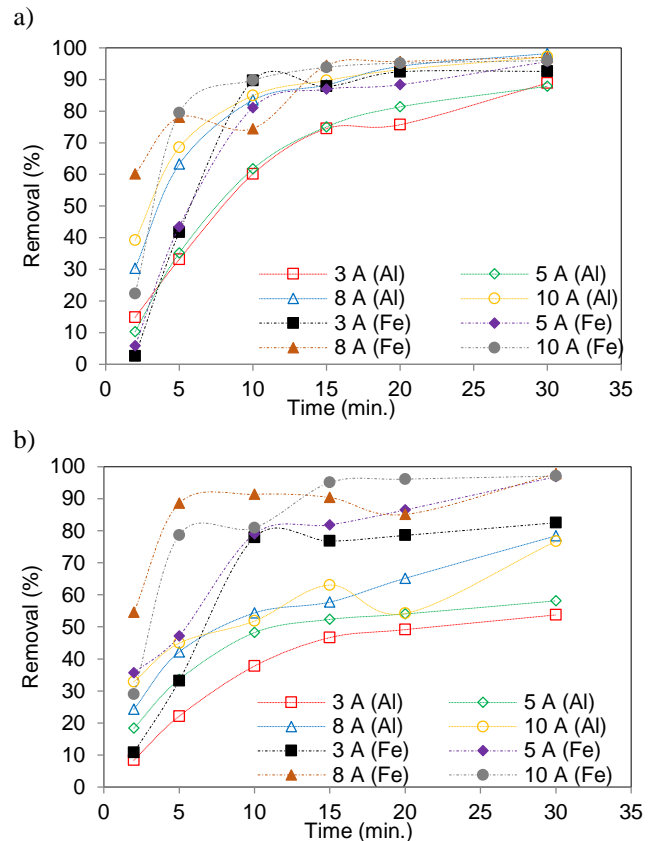


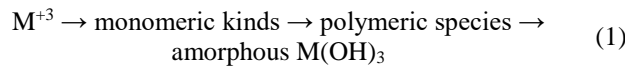
Figure 2. Effect of current on removal efficiency of (a) SW, (b) DBW.

Under 4 different currents varying in the range of 3-10 A, the removal efficiencies were obtained as 98% for the Al electrodes and 97% for the Fe electrodes in SW, while they were obtained as 78% for the Al electrodes and 98% for the Fe electrodes in DBW. Based on the results, the optimum current for both electrode types and both wastewater types was determined as 8 A. The aluminum and iron ions that emerge with the electrical current passing through the electrolyte during the electrocoagulation process form monomeric and polymeric hydroxyl complexes. Increased current passing through the system increases the quantity of ions that emerge, and in relation to this, it increases the formation of these complex compounds with high oxidative potential. These compounds, which are also excellent coagulants, lead to the formation of large floc networks that have a high pollutant removal capacity [20-22].

3.2. Effect of pH

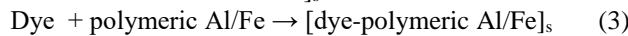
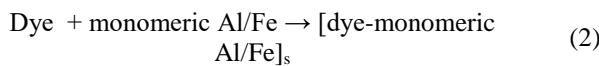
pH is one of the important operational parameters that are effective on the performance of all electrochemical processes, especially electrocoagulation. This is because, at suitable pH values, metal ions may form metal hydroxides that absorb and precipitate dissolved pollutants and species that coagulate in a broad spectrum with destabilized and aggregated suspended particles. In the electrocoagulation method, the pollutant

removal efficiency varies to a large extent based on the structure and quantities of the monomeric and polymeric compounds that are formed throughout the process. These monomeric, polymeric and oligomeric aluminum and iron species are transformed with complex and precipitation kinetics into insoluble amorphous $Al(OH)_3$ and $Fe(OH)_3$ based on the pH of the medium [18,23]. The complex mechanism that allows the formation of metal hydroxide flocs is expressed as follows in Eq. (1) [24].

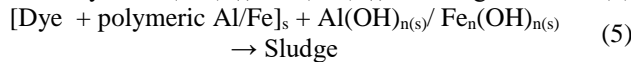
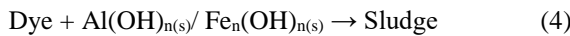


Dye removal mechanisms that are usually defined as precipitation for low pH values and adsorption for higher pH values are summarized as follows in Eqs. (2-5) [20,25-27].

Precipitation



Adsorption



Electrocoagulation is defined as a process with a buffer effect that has the capacity of balancing pH. In addition to this, process efficiency is explained by the formation of ionic species that do not precipitate or have high solubility which gain dominance in the medium based on pH [23,28].

The experiments where the optimum pH value was investigated were carried out at a dye concentration of 50 mg/L for SW, a dilution rate of 1/60 for DBW, at a current of 8 A and room temperature at pH values of 3, 5, 7, 8, 9 and natural pH for the Al electrodes and 3, 5, 7, 8, 9, 10 and natural pH for the Fe electrodes (Figure 3a-b).

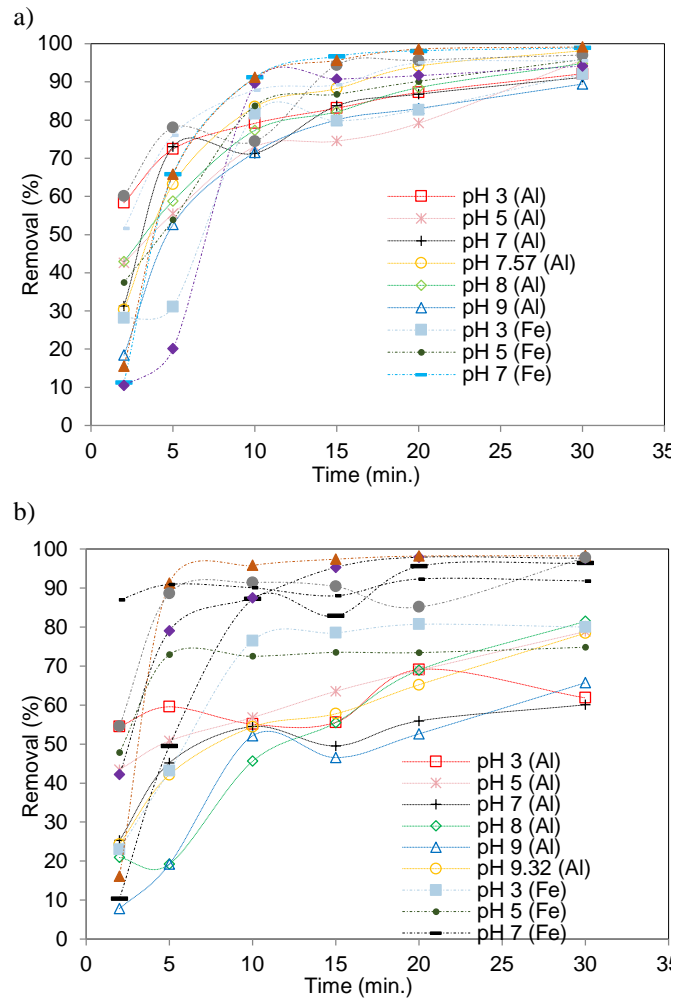


Figure 3. Effect of pH on removal efficiency of (a) SW, (b) DBW.

At the studied pH values, the removal efficiencies were obtained as 98% for the Al electrodes and 99% for the Fe electrodes in SW and 82% for the Al electrodes and 98% for the Fe electrodes in DBW. The optimum pH value was determined as the natural pH in SW and 8 in DBW for the Al electrodes, while it was determined as 9 for both wastewater types for the Fe electrodes.

3.3. Effect of initial dye concentration

The initial dye concentration, which provides a significant driving force to overcome the mass transfer resistance of the dissolved substances between the solid and liquid phase, constitutes one of the operational conditions that affect the removal efficiency in electrocoagulation, as in most other treatment methods [29]. Under the same current conditions and same electrolysis time, the same quantity of flocs is formed at different initial dye concentrations. The concentration of metal ions produced during the process shows a limiting effect for floc formation and is accepted as a limit factor. As the initial dye concentration increases, the quantity of flocs produced falls insufficient for adsorption and

sedimentation of all dye molecules. While electrocoagulation is generally a process with high efficiency in dye removal, studies have shown that, as the initial dye concentration increases, the removal efficiency decreases, and for the same efficiency to be achieved, longer treatment times are needed for higher concentrations [18,26,27,30].

The effects of the initial dye concentration were tested at a current of 8 A and room temperature at 5 different initial SW dye concentrations as 50, 100, 150, 200 and 300 mg/L at the natural pH (7.57) for the Al electrodes and at pH 9 for the Fe electrodes, while these effects were tested at 5 different DBW dilution ratios as 1/60, 1/30, 1/20, 1/15 and 1/10 at a pH of 8 for the Al electrodes and 9 for the Fe electrodes (Figure 4a-b).

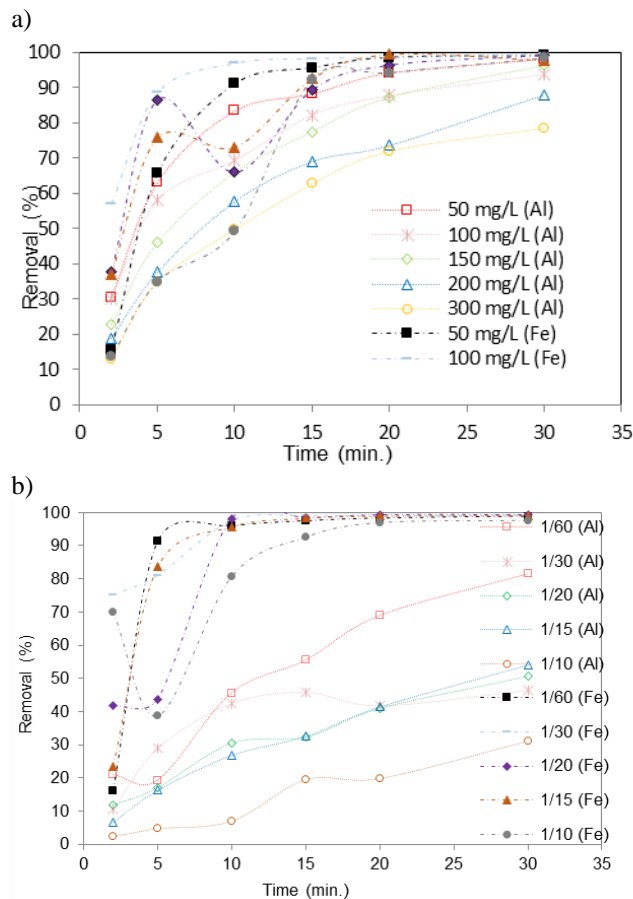


Figure 4. Effect of the initial dye concentration on removal efficiency of (a) SW, (b) DBW.

In the experiments carried out with different dye concentrations/dilution ratios, the removal efficiencies were obtained as 98% for the Al electrodes and 99.5% for the Fe electrodes in SW and as 82% for the Al electrodes and 99% for the Fe electrodes in DBW. Based on these results, the optimum initial dye concentration in SW was determined as 50 mg/L for the Al electrodes and 100 mg/L for the Fe electrodes. The optimum dilution ratio in DBW was determined as 1/60 for the Al electrodes and 1/30 for the Fe

electrodes. Considering the results, it is seen that the dye concentration and removal efficiency changed in inverse proportion to each other, which was in agreement with the information in the literature. However, it was seen that, in the experiments with the Fe electrodes, the highest removal efficiency was obtained with the second lowest dye concentration. This may be explained by that iron electrodes provide color to the wastewater.

At the second stage of the study, long-run treatments of SW and DBW were carried out without dilution and by using the optimum experimental conditions determined at the first stage. Color and COD removal efficiencies were examined in the experiments where Al and Fe electrodes were used. The treatment conditions were determined as a current of 8 A, the natural pH of SW for the Al electrodes and pH 9 for the Fe electrodes in SW experiments, while the conditions were determined as a current of 8 A, pH 8 for the Al electrodes and pH 9 for the Fe electrodes in the treatment of DBW (Figure 5a-b).

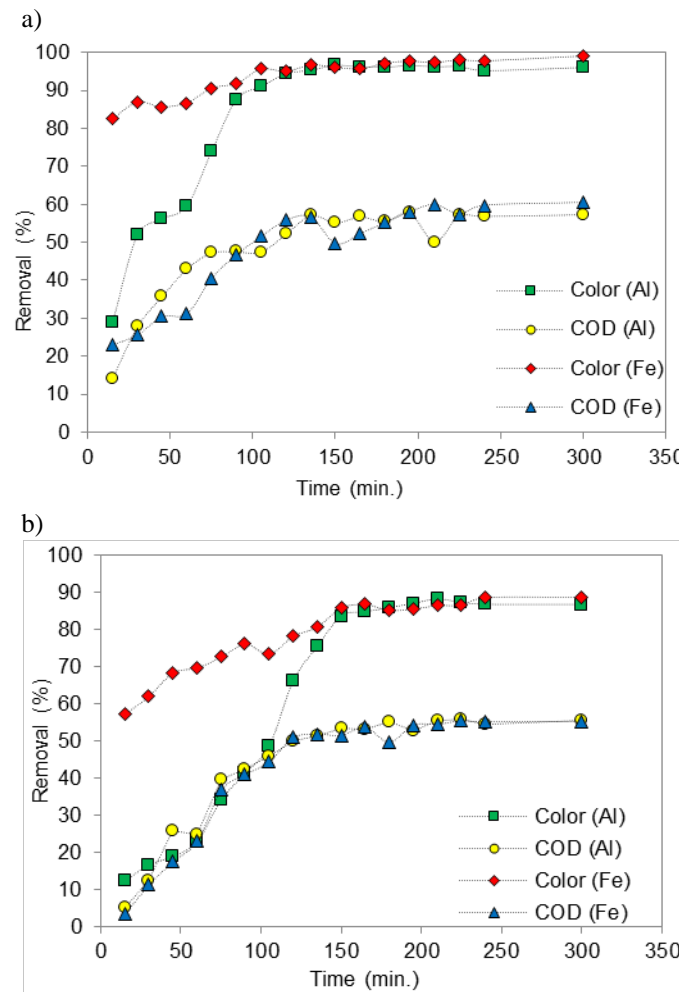


Figure 5. Color and COD removal efficiency in (a) SW, (b) DBW.

The color and COD removal efficiencies were found respectively as 96% and 57% with the Al electrodes and 99% and 61% for the Fe electrodes as a result of SW experiments lasting for 5 hours. Only after the 120th-135th minutes, the color and COD removal efficiencies reached the ranges of 94-95% and 52-57% for the Al electrodes and 95-97% and 56-57% for the Fe electrodes respectively. As a result of the DBW treatment experiments, the color and COD removal efficiencies were found respectively as 87% and 55% for the Al electrodes and 89% and 55% for the Fe electrodes. In the experiments, after the 120th-135th minutes, the color and COD removal efficiencies reached the ranges of 66-76% and 50-51% for the Al electrodes and 78-81% and 51-52% for the Fe electrodes.

3.4. Isotherms

Various isotherms, especially the Freundlich isotherm (FI) and Langmuir isotherm (LI), have been developed to reveal the progression of adsorption processes. These isotherms may

also be used to explain the reciprocal interactions between metal hydroxide and dye molecules in electrocoagulation. The linear FI and LI were given in Eqs. (6-7) below.

$$\ln q_e = \ln K_f + \left(\frac{1}{n}\right) \ln C_e \quad (6)$$

$$\frac{C_e}{q_e} = \frac{C_e}{q_m} + \frac{1}{K_L q_m} \quad (7)$$

In the study, by calculating FI and LI for different dye concentrations, their suitability with the experimental results was investigated. In the isotherms, q_e refers to the amount of adsorbed dye per unit adsorbent (mg/g), C_e is the dye concentration at equilibrium (mg/L), n is the adsorption intensity, K_f is Freundlich isotherm adsorption coefficient, q_m is the maximum dye amount adsorbed by unit adsorbent (mg/g), and K_L is Langmuir isotherm constant regarding adsorption energy (L/mg) [31-33]. The constants calculated from the isotherm curves in the study are given in Table 2.

Table 2. Langmuir and Freundlich isotherm constants

SW		Langmuir isotherm (LI)			Freundlich isotherm (FI)		
		q_m	K_L	R^2	K_f	n	R^2
	Al	555.556	0.146	0.983	126.474	2.793	0.901
	Fe	303.030	0.429	0.942	80.002	1.877	0.844
DBW		Langmuir isotherm (LI)			Freundlich isotherm (FI)		
		q_m	K_L	R^2	K_f	n	R^2
	Al	238.095	0.035	0.901	43.692	3.251	0.697
	Fe	285.741	0.385	0.920	78.668	1.730	0.777

The equilibrium constant as an important parameter determining the type of adsorption in Langmuir isotherm is calculated as shown in Eq. (8).

$$R_L = \frac{1}{1 + K_L C_0} \quad (8)$$

This constant shown as R_L is a dimensionless value calculated based on Langmuir isotherm constant (K_L) and the initial dye concentration (C_0). In the cases where this constant is found as $R_L > 1$, $R_L = 1$, $0 < R_L < 1$ or $R_L = 0$, the adsorption process is defined respectively as unfavorable, linear, favorable or irreversible [32,33]. The change in the R_L values in SW and DBW with the Al and Fe electrodes based on different dye concentrations is shown in Figure 6.

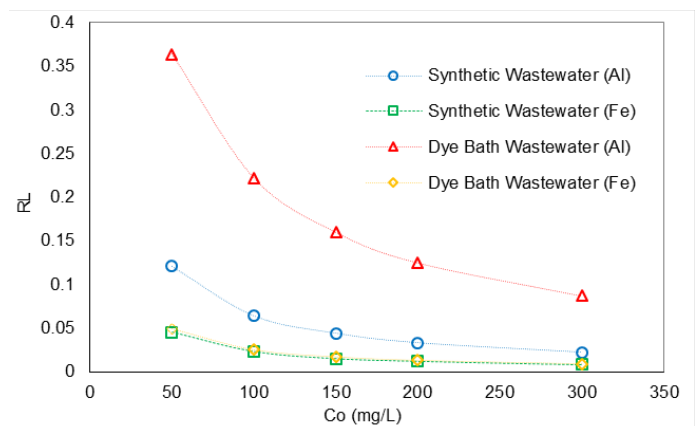


Figure 6. Change of R_L value according to initial dye concentration.

As seen in the results, the correlation coefficients for LI in SW were 0.983 and 0.942 respectively for the Al and Fe electrodes, while these were respectively 0.901 and 0.920 in DBW. Accordingly, the process was more compatible with LI, suggesting that the adsorption of dye molecules occurred on a homogenous surface as a single molecular layer than FI suggesting that it occurred on the regions with different

adsorption energy of a heterogenous surface in multiple molecular layers [31,34].

3.5. Statistical Analysis

In this study, the statistical analysis of COD and color removal from SW and DBW by Al and Fe electrodes was performed using "IBM SPSS Statistics 22", and the results were given in Table 3.

Table 3. Correlation analysis

		SW (Al)		SW (Fe)		DBW (Al)		DBW (Fe)	
		Color	COD	Color	COD	Color	COD	Color	COD
Color	Pearson Correlation	1	0.956**	1	0.979**	1	0.930**	1	0.954**
	Sig. (2-tailed)		0.000		0.000		0.000		0.000
	N	17	17	17	17	17	17	17	17
COD	Pearson Correlation	0.956**	1	0.979*	1	0.930**	1	0.954**	1
	Sig. (2-tailed)	0.000		0.000		0.000		0.000	
	N	17	17	17	17	17	17	17	17

** Correlation is significant at the 0.01 level (2-tailed).

In terms of correlation analysis, as expressed in Table 3, there was a positive relationship between the variables (color and COD) at the 0.01 significance level. The homogeneity of the variance was firstly analyzed for color removal, and a heterogeneous variance distribution was reached since the result was not homogeneous (Levene's: 23.552; $p < 0.001$). As a result of the one-way analysis of variance (ANOVA),

according to sig. $p < 0.05$, there was a statistically significant difference between SW (Al), SW(Fe), DBW (Al) and DBW (Fe). Post hoc analysis was performed to find out in which groups this difference occurred, and the results were presented in Table 4.

Table 4. Multiple comparisons dependent variable: color

(I) group	(J) group	Mean Difference (I-J)	Std. Error	Sig.	95% Confidence Interval	
					Lower Bound	Upper Bound
SW (Al)	SW (Fe)	-10.698	5.222	0.290	-26.123	4.726
	DBW(Al)	22.471	8.816	0.095	-2.434	47.377
	DBW (Fe)	4.486	5.594	0.966	-11.630	20.603
SW (Fe)	SW (Al)	10.698	5.222	0.290	-4.726	26.123
	DBW(Al)	33.171*	7.324	0.002	11.386	54.955
	DBW (Fe)	15.185*	2.684	0.000	7.505	22.865
DBW(Al)	SW (Al)	-22.472	8.816	0.095	-47.377	2.434
	SW (Fe)	-33.171*	7.324	0.002	-54.955	-11.386
	DBW (Fe)	-17.985	7.593	0.159	-40.211	4.241
DBW (Fe)	SW (Al)	-4.486	5.594	0.966	-20.603	11.630
	SW (Fe)	-15.185*	2.684	0.000	-22.865	-7.505
	DBW(Al)	17.985	7.593	0.159	-4.241	40.211

* The mean difference is significant at the 0.05 level.

According to the analysis results, there were significant differences between the group SW-Fe and DBW-Al and between SW-Fe and DBW-Fe in terms of wastewater mean value for the color. When the COD removal efficiencies were examined in the experiments, firstly, the homogeneity of the variances was analyzed, and homogeneous variance distributions were used (Levene's: 1.207; sig.=0.314 i.e. $p>0.001$). As a result of the one-way ANOVA, according to sig. $p>0.05$, there was no statistically significant difference between SW (Al), SW(Fe), DBW (Al) and DBW (Fe).

4. Conclusion

This study was carried out with DBW collected from a yarn dyeing bath where Setazol Black TNN, which is a reactive diazo dye, was used and SW prepared with the same dye. As a result of the experiments, the optimum current and pH for both electrode materials and the optimum initial dye concentration for SW and the optimum dilution ratio for DBW were determined. Considering the results, it was seen that the optimum values for SW and DBW were mostly the same, and in the pH determination experiments with the Al electrodes, the results were close as pH 7.57 and pH 8.

In the study, the treatment of DBW without dilution and SW prepared with the same color value as these wastewaters was studied as a 5-hour treatment by using the determined optimum experimental conditions and monitoring color and COD removal efficiencies. As a result of the long-run treatment experiments, treatment efficiencies of 96% and 57% for respectively color and COD for the Al electrodes and 99% and 61% for the Fe electrodes in SW, 87% and 55% for the Al electrodes and 89% and 55% for the Fe electrodes in DBW were obtained. Moreover, it was observed that, beginning with the 120th-135th minutes, in color and COD removal, respectively, removal efficiencies in the ranges of 94-95% and 52-57% for the Al electrodes and 95-97% and 56-57% for the Fe electrodes in SW, 66-76% and 50-51% for the Al electrodes and 78-81% and 51-52% for the Fe electrodes in DBW were reached. This study showed that, based on the results on the dye used here, the electrocoagulation method may be used as a treatment step for wastewaters containing intense concentrations of color. Moreover, the suitability of the study for FI and LI, which are the two most significant adsorption isotherm models, was also examined. It was determined that the experimental data were more suitable for LI model for both wastewater types and the Al and Fe electrodes. Finally, a correlation analysis was performed between color and COD for the Al and Fe electrodes and SW and DBW types. Besides, the yield ratios for the usage of Al and Fe electrodes respectively for both color and COD were compared and comments were made for different groups by one-way ANOVA. One-Way ANOVA test was performed using IBM SPSS Statistics 22 to test whether there was a significant difference between different electrode (Al and Fe) and wastewater types (SW and DBW) for color and COD

removal. According to the correlation analysis, there is a positive relationship between the variables (color and COD) on a significance level of 0.01. In one-way ANOVA tests performed separately for color and COD, since the significance for the color was < 0.05 , there was a significant difference between the variables, while for COD, there was no significant difference between the variables because the significance was > 0.05 .

Acknowledgements

This work was supported by Namık Kemal University (Scientific Research Projects Commission), Project No: NKUBAP.00.17.YL.12.04.

References

- [1]. EPA, "EPA office of compliance sector notebook project: Profile of the textile industry", EPA/310-R-97-009, Washington, (1997), pp. 13-51.
- [2]. Verma A.K., Dash R.R., Bhunia P., "A review on chemical coagulation/flocculation technologies for removal of colour from textile wastewater", *Journal of Environmental Management*, 93, (2012), 154-168.
- [3]. Vahdat A., Bahrami S.H., Arami M., Bahjat A., Tabakh F., Khairkhan M., "Decoloration and mineralization of reactive dyes using electron beam irradiation, part I: Effect of the dye structure, concentration and absorbed dose (single, binary and ternary systems)", *Radiation Physics and Chemistry*, 81, (2012), 851-856.
- [4]. Khandegar V., Saroha A.K., "Electrocoagulation for the treatment of textile industry effluent- a review", *Journal of Environmental Management*, 128, (2013), 949-963.
- [5]. Khatri A., Peerzada M.H., Mohsin M., White M., "A review on developments in dyeing cotton fabrics with reactive dyes for reducing effluents pollution", *Journal of Cleaner Production*, 87, (2015), 50-57.
- [6]. Khan R., Banerjee U.C., "Decolorization of azo dyes by immobilized bacteria. In: Erkurt, H. A. (ed.), *Biodegradation of azo dyes*", *The Handbook of Environmental Chemistry*, Springer: (2010), pp. 73-75.
- [7]. Choudhury A.K.R., "Textile preparation and dyeing", Science Publishers, (2006), pp. 376-377.
- [8]. Rizk H.F., İbrahim S.A., El-Borai M.A., "Synthesis, fastness properties, color assessment and antimicrobial activity of some azo reactive dyes having pyrazole moiety", *Dyes Pigments*, 112, (2015), 86-92.

- [9]. Christie, R. M., "Color chemistry", The Royal Society of Chemistry: Cambridge, (2001), pp. 24-146.
- [10]. Christie, R. M., "Colour Chemistry", 2nd edition, Royal Society of Chemistry, Cambridge, (2015), pp.72-75.
- [11]. Khan Z., Jain K., Soni A., Madamwar D., "Microaerophilic degradation of sulphonated azo dye-reactive red 195 by bacterial consortium AR1 through co-metabolism", *International Biodeterioration & Biodegradation*, 94, (2014), 167-175.
- [12]. Singh R.L., Singh P.K., Sing R.P., "Enzymatic decolorization and degradation of azo dyes-A review", *International Biodeterioration & Biodegradation*, 104, (2015), 21-31.
- [13]. Malakootian M., Mansoorian H.J., Hosseini A., Khanjani N., "Evaluating the efficacy of alumina/carbon nanotube hybrid adsorbents in removing azo reactive red 198 and blue 19 dyes from aqueous solutions", *Process Safety and Environmental Protection*, 96, (2015), 125-137.
- [14]. Chequer F.M.D., Lizier T.M., Felicio R., Zanoni M.V.B., Debonsi, H.M., Lopesi N.P., Oliveira D.P., "The azo dye disperse red 13 and its oxidation and reduction products showed mutagenic potential", *Toxicol in Vitro*, 29, (2015), 1906-1915.
- [15]. Shan B., Tong X., Xiong W., Qiu W., Tang B., Lu R., Ma W., Luo Y., Zhang S., "A new kind of h-acid monoazo-anthraquinone reactive dyes with surprising colour", *Dyes Pigments*, 123, (2015), 44-54.
- [16]. Aouni A., Fersi C., Cuarteres-Urbe B., Bes-Pia A., Alcaina-Miranda M.I., Dhabbi M., "Reactive dyes rejection and textile effluent treatment study using ultrafiltration and nanofiltration processes", *Desalination*, 297, (2012), 87-96.
- [17]. Standard Methods, "Standard methods for the examination of water and wastewater", American Public Health Association, 19th edition, APHA, AWWA, WPCF, Washington, (1995).
- [18]. Fajardo A.S., Martins R.C., Silva D.R., Martinez-Huitle C.A., Quinta-Ferreira R.M., "Dye wastewaters treatment using batch and recirculation flow electrocoagulation systems", *Journal of Electroanalytical Chemistry*, 801, (2017), 30-37.
- [19]. Khemila B., Merzouk B., Chouder A., Zidelkhi A., Leclerc J-P., Lapique F., "Removal of a textile dye using photovoltaic electrocoagulation", *Sustainable Chemistry and Pharmacy*, 7, (2018), 27-35.
- [20]. Khorram A.G., Fallah N., "Treatment of textile dyeing factory wastewater by electrocoagulation with low sludge settling time: Optimization of operating parameters by RSM", *Journal of Environmental Chemical Engineering*, 6, (2018), 635-642.
- [21]. Daneshvar N., Oladegaragoze A., Djafarzadeh N., "Decolorization of basic dye solutions by electrocoagulation: An investigation of the effect of operational parameters", *Journal of Hazardous Material*, 129, (2006), 116-122.
- [22]. Öztürk T., Veli S., Dimoglo A., "The effect of seawater conductivity on the treatment of leachate by electrocoagulation", *Chemical and Biochemical Engineering Quarterly*, 27, (2013), 347-354.
- [23]. Verma A. K., "Treatment of textile wastewaters by electrocoagulation employing Fe-Al composite electrode", *Journal of Water Process Engineering*, 20, (2017), 168-172.
- [24]. Katal R., Pahlavanzadeh H., "Influence of different combinations of aluminum and iron electrode on electrocoagulation efficiency: Application to the treatment of paper mill wastewater", *Desalination*, 265, (2011), 199-205.
- [25]. Ma H., Wang B. Wang Y., "Application of molybdenum and phosphate modified kaolin in electrochemical treatment of paper mill wastewater", *Journal of Hazardous Material*, 145, (2007), 417-423.
- [26]. Pajootan E., Arami M., Mahmoodi N.M., "Binary system dye removal by electrocoagulation from synthetic and real colored wastewaters", *Journal of the Taiwan Institute of Chemical Engineers*, 43, (2012), 282-290.
- [27]. Nandi B.K., Patel S., "Effects of operational parameters on the removal of brilliant green dye from aqueous solutions by electrocoagulation", *Arabian Journal of Chemistry*, 10, (2017), S2961-S2968.
- [28]. Zaied M., Bellakhal N., "Electrocoagulation treatment of black liquor from paper industry" *Journal of Hazardous Material*, 163, (2009), 995-1000.
- [29]. Ouaisa Y.A., Chabani M., Amrane A., Bensmaili A., "Removal of tetracycline by electrocoagulation: Kinetic and isotherm modeling through adsorption", *Journal of*

- Environmental Chemical Engineering, 2, (2014), 177-184.
- [30]. Mbacké M.K., Kane C., Diallo N.O., Diop C.M., Chauvet F., Combat M., Tzedakis T., “Electrocoagulation process applied on pollutants treatment-experimental optimization and fundamental investigation of the crystal violet dye removal”, Journal of Environmental Chemical Engineering, 4, (2016), 4001-4011.
- [31]. Hakizimana J.N., Gourich B., Chafi M., Stiriba Y., Vial C., Drogui P., Naja J., “Electrocoagulation Process in Water Treatment: A Review of Electrocoagulation Modeling Approaches”, Desalination, 404, (2017), 1-21.
- [32]. Yoosefian M., Ahmadzadeh S., Aghasi M., Dolatabadi M., (2017) “Optimization of Electrocoagulation Process for Efficient Removal of Ciprofloxacin Antibiotic Using Iron Electrode: Kinetic and Isotherm Studies of Adsorption”, Journal of Molecular Liquids, 225, (2017), 544-553.
- [33]. Zhang Y., Huang G., An C., Xin X., Liu X., Raman M., Yao Y., Wang W., Doble M., “Transport of anion azo dyes from aqueous solution to gemini surfactant-modified wheat bran: Synchrotron infrared, molecular interaction and adsorption studies”, Science of the Total Environment, 595, (2017), 723-732.
- [34]. Alshameri A., He H., Zhu J. Xi, Y., Zhu R., Ma L., Tao Q., “Adsorption of ammonium by different natural clay minerals: Characterization, kinetics and adsorption isotherms”, Applied Clay Science, 159, (2018), 83-93.

Effective clay material enriched with thiol groups for Zn(II) removal from aqueous media: A statistical approach based on response surface methodology

Ümit Ecer,¹ Şakir Yılmaz,^{1,*} Tekin Şahan¹

Van Yuzuncu Yil University, Faculty of Engineering, Department of Chemical Engineering, 65080 Van Turkey,
sakiryilmaz@yyu.edu.tr, ORCID: 0000-0001-9797-0959

ABSTRACT

In the present work, the removal of Zn(II) ions from aquatic environments onto 3-mercaptopropyl trimethoxysilane modified kaolin (MK) was investigated in a batch system. Moreover, the optimization and effects of independent parameters such as pH, initial Zn(II) concentration (C_0 , mg/L) and contact time (min) on the uptake of Zn(II) onto MK were examined by response surface methodology (RSM). Central composite design (CCD) in RSM, the most popular statistical technique, was successfully applied to optimize and model the selected parameters (pH, C_0 , contact time) for Zn(II)% adsorption onto MK. The number of experiments based on CDD was 20, a total of 20 sets which included fourteen factorial points and six center points were performed to obtain the maximum Zn(II) uptake from aqueous solutions. The optimum points obtained from CCD were 6.39, 50.09 mg/L and 76.10 min for pH, C_0 , and contact time, in their given order. In these optimal conditions, the maximum removal percentage was found to be 86.19%. The results indicated that the removal yield of Zn(II) from aqueous media onto MK was successfully performed by CCD in RSM. It can be concluded that MK is also a promising material for the uptake of other heavy metals similar to Zn.

ARTICLE INFO

Research article

Received: 25.09.2020

Accepted: 17.12.2020

Keywords:

Adsorption,
kaolin,
response surface
methodology,
thiol,
zinc

*Corresponding author

1. Introduction

Rapid industrialization and growing population have become critical environmental issues due to the increasing contamination of water resources by pollutants such as heavy metal ions [1]. Environmental pollution is one of the most significant issues for many forms of life [2], because the presence of heavy metals in aquatic media is a major concern owing to their toxic effects on all living organisms [3]. Zinc, a heavy metal, is found in various industrial effluents including those from galvanizing plants, leather industries, electroplating, paper mills, and mining [3, 4]. These toxic effluents in aqueous environments cause serious health risks like skin irritation, stomach cramps, anemia, cancer, nausea, brain damage, and accumulative poisoning [4]. Therefore, it becomes mandatory to remove Zn(II) ions as a toxic metal from aqueous environments.

Several traditional approaches were reported to eliminate heavy metal ions from aquatic environments like reverse osmosis, chemical precipitation, electrochemical treatment, membrane processes, and adsorption. These treatment

procedures have some disadvantages because of economic constraints, sludge disposal, and inefficiency at low heavy metal ion concentrations [5]. Among these techniques, the adsorption approach is considered more economic and effective for uptake of contaminants from wastewater owing to high efficiency, low cost, and simplicity of operation [6]. The effectiveness of the adsorption process depends on cost, nature, and regeneration of the selected adsorbent. Hence, adsorbents with low-cost and abundant in nature such as clay minerals have attracted attention in the field of adsorption process. These materials, however, have some drawbacks such as low removal rate, high regeneration cost, low surface area and long adsorption equilibrium time [4, 5, 7]. Recently, surface-functionalized natural clay minerals gained increasing attention via to enhance the adsorption capacity the adsorption process [8]. For example, Olu-Owolabi and Unuabonah [9] reported that sulfur and phosphorus modified bentonite had enhanced removal capability for Zn(II) adsorption after surface modification in comparison with raw bentonite. Jemima et al. [10] evaluated the removal performance for Cr(VI) by modifying montmorillonite clay with various cationic surfactants. They reported that modified-

montmorillonite materials had excellent adsorption performance compared to unmodified clay.

Conventional methods require extra experiments, extra time, and large doses of materials because only one independent parameter affecting the adsorption is changed while the other parameters are kept at fixed points during these processes. These methods are therefore disadvantageous. Statistical programs such as response surface methodology (RSM) are promising to overcome these problems [11, 12].

The objective of this study was to model and optimize the removal of Zn(II) ions onto 3-mercaptopropyl trimethoxysilane-modified kaolin (MK) by using response surface methodology (RSM). A central composite design (CCD) was used to determine optimal conditions for the independent parameters, such as pH, initial Zn(II) concentration, and contact time, that affect the removal of Zn(II) onto MK from aqueous environments.

2. Materials and methods

Clay minerals used as adsorbent in the current work were acquired from the JSC Glukhovetsky Kaolin Plant located in Ukraine. Prior to utilization as adsorbent, the obtained materials were washed with ultra-pure water and dried in a drying-oven at 120 °C for 18 h. The dried samples were then ground into fine powder using a mill and passed through a sieve. Finally, the prepared samples were modified based on the previously reported method in the literature [13].

Zn(II) stock solution (500 mg/L) was prepared by dissolving the calculated metal salt of $Zn(NO_3)_2 \cdot 6H_2O$ in 500 mL of ultra-pure water. The desired concentrations were prepared by using dilutions of the stock solution.

All tests were carried out by adding 0.25 g amount of MK in 50 mL to the heavy metal ion solution with desired pH, initial Zn(II) ions concentration (C_o , mg/L), and contact time (min). All tests for the three selected independent parameters of pH, C_o , and contact time were generated by CCD in RSM by taking fixed mixing rate of 700 rpm and room temperature. After that, the suspension of the adsorbent was separated by a centrifuge at 9000 rpm for 15 min. The obtained supernatant was analyzed by an atomic absorption spectrophotometer (AAS, Thermo Scientific iCE 3000 SERIES, USA). The removal percentage of Zn(II) with adsorption onto MK was determined by the following equation;

$$Zn(II)\% \text{ Adsorption} = \frac{(C_o - C_e)}{C_o} \times 100 \quad (1)$$

where C_o and C_e (mg/L) are the initial and equilibrium Zn(II) concentration in the solution (mg/L), respectively.

CCD in RSM is the most effective program and was applied to optimize the selected independent parameters. The levels of

the selected parameters were coded as +1 (upper), 0 (central), and -1 (bottom), as presented in Table 1. A second-order polynomial model typifying system behavior is represented as follows:

$$\hat{y}_n = \beta_o + \sum_{i=1}^3 \beta_i x_i + \sum_{i=1}^3 \beta_{ii} x_i^2 + \sum_{i=1}^3 \sum_{j=i+1}^3 \beta_{ij} x_i x_j \quad (2)$$

where \hat{y}_n is the predicted response (Zn(II)% adsorption), X_i ($i = 1-3$) are the independent parameters being studied, β_o , β_i , β_{ii} , and β_{ij} are the intercept, the linear, the quadratic, and the interactive effects, respectively.

3. Results and discussion

3.1. Characterization of adsorbent

MK characterization was already reported in our previous study [13]. Based on the obtained results, transform infrared (FTIR) spectroscopy analysis results indicated that the peak representing -SH stretching vibration was present at 2550-2600 cm^{-1} , which was not observed in unmodified kaolin. Furthermore, the characteristic peak observed at 2931 cm^{-1} was due to methoxy groups (-OCH₃) in MK. From energy-dispersive x-ray spectroscopy (EDX) results, the sulfur peak was different from raw kaolin, indicating that the surface of the kaolin was successfully covered with -SH groups. X-ray diffraction (XRD) analyses showed that the diffraction signal intensity was diminished, relating to the formation of silanol groups on the kaolin surface and methoxy groups.

3.2. Experimental and statistical analysis

The CCD approach in RSM was successfully performed to evaluate the optimal process points for Zn(II) onto MK. The three independent parameters (pH, C_o , and contact time) were selected to maximize Zn(II) adsorption onto MK. These parameters were segregated into three levels with a coded value (-1, 0, +1). From CCD, 20 experimental runs were carried out as given in Table 1. These tests designated by CCD were performed against percentage removal of Zn(II) for each independent parameter. The second-order model equation obtained from CCD which indicates the relationship between Zn(II) removal efficiency and independent variables is given in the following:

$$\begin{aligned} Zn\% \text{ adsorption} = & -47.54189 + 27.40655[pH] + 1.48875[C_o] + 0.48135[\text{Contact time}] \\ & + 7.08333E-003[pH][C_o] - 0.018409[pH][\text{Contact time}] + 3.00606E-003[C_o][\text{Contact time}] \\ & - 2.45621[pH]^2 - 0.015857[C_o]^2 - 2.98873E-003[\text{Contact time}]^2 \end{aligned} \quad (4)$$

Statistical analysis was used to evaluate whether the adsorption process was significant. For this purpose, the importance of the suggested quadratic model for the removal of Zn(II) onto MK was determined by the analysis of variance (ANOVA). The ANOVA results (Table 2) showed that the suggested model for the removal percentage of Zn(II) ions onto MK was dependent on the selected parameters. Moreover, low p -value (< 0.0001) and the determination of

coefficient (R^2) value of 0.96 demonstrated that the obtained model has good fit for predicting the removal percentage of Zn(II) onto MK.

Table 2 illustrates that the linear factors (A and C), the interaction of factor (BC), and the quadratic of factors (A^2 , B^2 , and C^2) are statistically significant model terms. However, it can be said that any independent parameter has little effect on the model equation, even if the other parameters were insignificant terms to the response.

Table 1. Uncoded and coded values of the independent parameters and CCD matrix corresponding to response values.

Parameters	Uncoded and coded values		
	-1	0	+1
pH (A)	2	5	8
C ₀ (mg/L, B)	20	50	80
Contact time (min, C)	10	65	120

Run	A	B (mg/L)	C (min.)	Zn(II)% removal
1	5(0)	50(0)	65(0)	84.50
2	5(0)	50(0)	65(0)	84.41
3	8(+1)	50(0)	65(0)	72.12
4	8(+1)	80(+1)	10(-1)	41.93
5	5(0)	50(0)	65(0)	83.95
6	5(0)	50(0)	65(0)	83.88
7	5(0)	20(-1)	65(0)	75.53
8	2(-1)	20(-1)	10(-1)	22.93
9	2(-1)	50(0)	65(0)	66.36
10	2(-1)	20(-1)	120(+1)	36.74
11	5(0)	50(0)	10(-1)	81.86
12	5(0)	80(+1)	65(0)	78.62
13	2(-1)	80(+1)	120(+1)	57.55
14	5(0)	50(0)	65(0)	84.62
15	8(+1)	80(+1)	120(+1)	63.43
16	5(0)	50(0)	65(0)	84.25
17	8(+1)	20(-1)	10(-1)	38.41
18	8(+1)	20(-1)	120(+1)	45.86
19	2(-1)	80(+1)	10(-1)	18.11
20	5(0)	50(0)	120(+1)	82.75

Table 2. ANOVA results.

Source	Sum of squares	df	Mean square	F value	p-value (Prob > F)
Model (significant)	9222.80	9	1024.76	27.19	< 0.0001
A-pH	360.72	1	360.72	9.57	0.0114
B-C ₀ (mg/L)	161.36	1	161.36	4.28	0.0654
C-Contact time (min.)	690.39	1	690.39	18.32	0.0016
AB	3.25	1	3.25	0.086	0.7750
AC	73.81	1	73.81	1.96	0.1919
BC	196.81	1	196.81	5.22	0.0454
A ²	1343.85	1	1343.85	35.66	0.0001
B ²	560.06	1	560.06	14.86	0.0032
C ²	224.78	1	224.78	5.97	0.0347

R² = 0.96

Adj. R² = 0.93 C.V. % = 9.53 Press = 2590.92
 Std. Dev. = 6.14 Adeq Precision = 14.82

The comparison of values predicted by the model vs observed for the removal percentage of Zn(II) is presented in Figure 1a. The observed data are quite close to the predicted data, indicating that the suggested model satisfactorily describes the correlation between independent parameters and adsorption of Zn(II) on MK. The normal probability plot of the residuals for Zn(II) adsorption is illustrated in Figure 1b. From Figure 1b, the errors are normally distributed, indicating that the obtained quadratic model could perfectly estimate the experimental values.

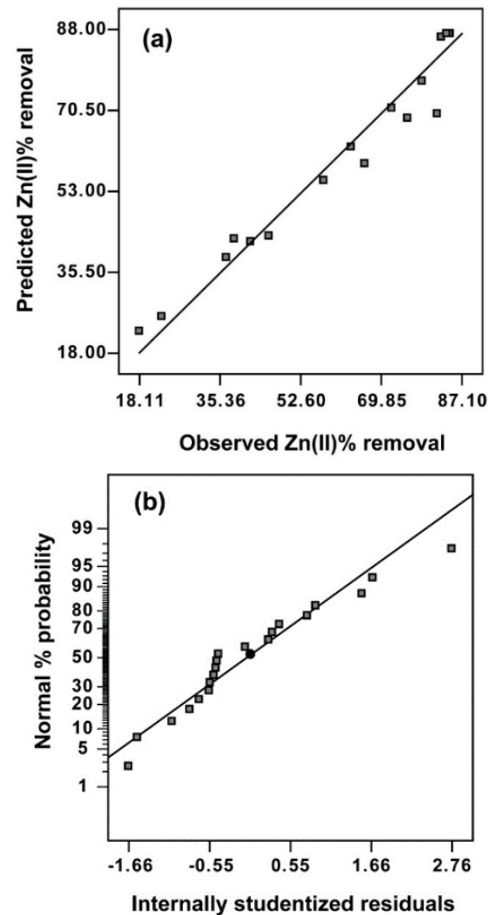


Figure 1. (a) Predicted versus observed values and (b) residual plots for Zn(II)% removal.

Figure 2a and b show the simultaneous effect of pH and C₀ on the removal efficiency of Zn(II) and the main effect of pH on the removal percentage of Zn(II), respectively. According to Figure 2a and b, increasing the pH of the solution from 2 to ~6 resulted in an increase in Zn(II)% removal. This is attributed to Pearson's Hard and Soft Acid-Base (HSAB) theory, indicating that -SH groups and Zn(II) ions have a strong bond for each other [13]. Moreover, the surface of MK is negatively charged at higher pH values. Therefore, the removal of Zn(II) gradually increases while pH increases due

to electrostatic attraction between negatively-charged MK and Zn(II) ions [14]. When the pH was increased to the upper level of 6, the removal rates for Zn(II) rapidly reduced. This can be explained by the Zn(OH)₂ formation of Zn(II) ions [1, 7].

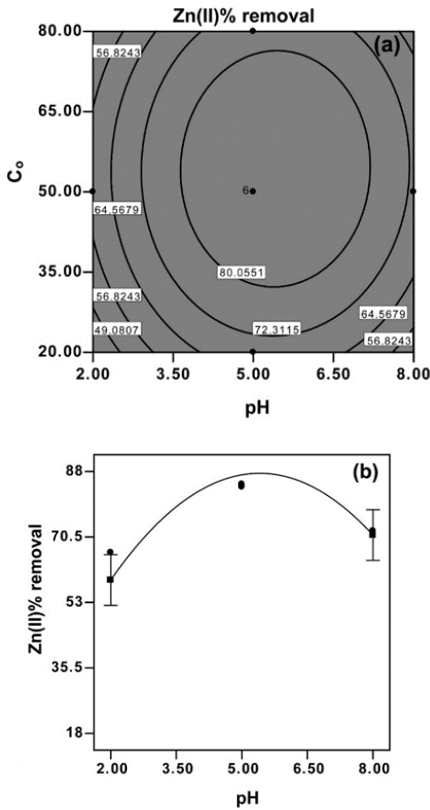


Figure 2. (a) Contour plot of pH and C_o , (b) the main effect plot of pH for Zn(II)% removal onto MK.

Similarly, the contour plot of C_o and contact time and the main effect of C_o on Zn(II)% removal onto MK is shown in Figure 3a and b, respectively. Analysis of the C_o effect revealed that as C_o increased in the ranges from 20 to 50 mg/L, the removal rate of Zn(II) increased; however, it decreased when C_o was more than 50 mg/L. The results imply that available binding sites for Zn(II)% removal were saturated with heavy metal ions and equilibrium was reached [14]. The correlation between the removal efficiency for Zn(II) ions and contact time vs pH and the main effect of contact time on Zn(II)% adsorption are given in Figure 4a and b, respectively. As can be understood from Figure 4a and b, Zn(II)% removal increased with an increase in contact time from 10 to 90-100 min and did not change significantly with contact time after 90-100 min. This observation confirmed that an equilibrium state results at about 90-100 min for Zn(II)% removal [15].

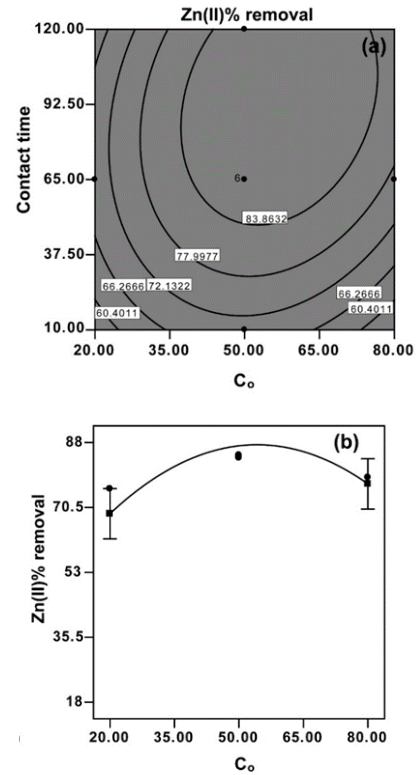


Figure 3. (a) Contour plot of C_o and contact time, (b) the main effect plot of C_o for Zn(II)% removal onto MK.

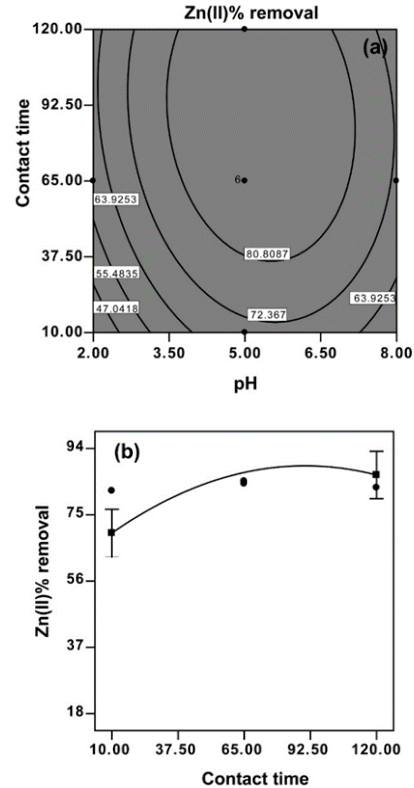


Figure 4. (a) Contour plot of pH and contact time, (b) the main effect plot of contact time for Zn(II)% removal onto MK.

3.3. Numerical analysis results

It is important to maximize the Zn(II) ion removal rate onto MK. This method utilized a quadratic model to maximize Zn(II)% removal within the selected experimental range. The numerical analysis approach in CCD was used to determine the optimal points for Zn(II)% removal onto MK. The optimal process points for Zn(II)% removal were found to be pH = 6.39, $C_0 = 50.09$ mg/L, and contact time = 76.10 min. At these points, the maximum Zn(II)% removal was found as 86.19%. Some tests were made to evaluate Zn(II)% removal at the obtained optimum adsorption points. The findings indicated that the removal percentage of Zn(II) onto MK is markedly increased compared to raw kaolin (49.15%).

The maximum values for Zn(II) adsorption with different adsorbents are given in Table 3. These results indicated that the adsorption performance of MK are substantially good for Zn(II) adsorption and it is an ideal material for removal of Zn(II) from aqueous media.

3.4. Adsorption mechanism

MK was used as an adsorbent to remove Zn(II) ions from aqueous environments. The revelation of the possible mechanism has major significance to evaluate the nature of the process and show how MK as adsorbent interacts with Zn(II) as adsorbate. Figure 5 shows the proposed model for Zn(II)% removal onto MK. During Zn(II) adsorption, Zn(II) ions first pass to the MK surface and reach the surface of MK by transfer from the boundary layer between the aqueous solution and MK. Subsequently, Zn(II) ions are affected by functional groups on MK. Then, Zn(II) ions are adsorbed onto MK. According to HSAB theory, there is strong interaction between thiol groups on the surface of MK and Zn(II) ions with each other [16]. Therefore, Zn-S bonding could be formed with -SH groups on the surface owing to the electrostatic interactions [17-19].

Moreover, the surface charge of the adsorbent is directly related to the solution pH. At low pH-values, the surface is positively charged and presence H^+ ions in the solution, leading to the decrease of Zn(II)% removal due to electrostatic repulsion between Zn(II) ions and positively charged adsorbent. On the other hand, an increase in pH of Zn(II) solution results in the reduction of positive surface charge, indicating that the electrostatic attraction between the negatively charged adsorbent surface and the positively charged Zn(II) ions. It is true that the predominant species of Zn(II) is $Zn(OH)_2$ at pH > 8, corresponding that decrease in adsorption yield compared to neutral conditions [2, 20].

Table 3. A comparison of Zn(II) adsorption for previous studies in literature.

Material	C_0 (mg/L)	Ads. Dosage (g/50 mL)	q_{max} (mg/g)	Zn(II) % removal	Ref.
Seed pods	50.13	0.15	13.04	78.02	[14]
Palm kernel shell based activated carbon	55	0.55	4.29	85.82	[3]
Oil palm empty fruit bunches	200	0.4	15.18	25.49	[21]
Maghemite ($\gamma\text{-Fe}_2\text{O}_3$)	50	0.24	4.79	45.41	[5]
Modified bentonite	50-200	0.5	35.21	43.88	[22]
Gracilaria Corticata	100	1	4.75	95	[12]
MK	50.09	0.25	8.64	86.19	This work

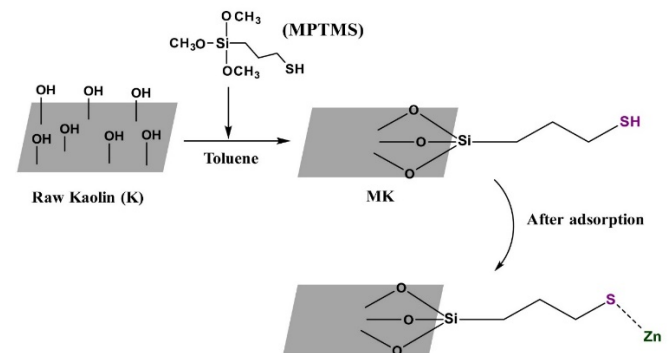


Figure 5. Possible adsorption mechanism for Zn(II) onto MK.

4. Conclusions

The influence of independent parameters such as pH, C_0 , and contact time on the removal of Zn(II) from aqueous environments by MK was studied using CCD based on RSM. A quadratic model for Zn(II)% removal was developed using CCD, indicating that the obtained model fitted well to experimental values. ANOVA results showed that p -value is quite low (< 0.0001). It can be said that the quadratic model is sufficient to predict experimental data. From numerical analysis results, the maximum removal rate of 86.19% for Zn(II) by MK was found at pH of 6.39, C_0 of 50.09 mg/L, and contact time of 76.10 min. Consequently, the results suggest that MK has potential use as adsorbent for the removal of heavy metal ions such as Zn from aqueous environments. Moreover, it can be said that RSM is a promising approach to optimize and model the independent parameters affecting adsorption technology.

References

- [1]. Vojoudi H., Badieli A., Amiri A., Banaei A., Ziarani G.M., Schenk-Joß K., "Pre-concentration of Zn(II) ions from aqueous solutions using meso-porous pyridine-enrobed magnetite nanostructures", *Food Chemistry*, 257, (2018), 189-195.
- [2]. Mousavi S.J., Parvini M., Ghorbani M., "Experimental design data for the zinc ions adsorption based on mesoporous modified chitosan using central composite design method", *Carbohydrate Polymers*, 188, (2018), 197-212.
- [3]. Karri R.R., Sahu J.N., "Modeling and optimization by particle swarm embedded neural network for adsorption of zinc (II) by palm kernel shell based activated carbon from aqueous environment", *Journal of Environmental Management*, 206, (2018), 178-191.
- [4]. Shanmugaprakash M., Venkatachalam S., Rajendran K., Pugazhendhi A., "Biosorptive removal of Zn(II) ions by *Pongamia* oil cake (*Pongamia pinnata*) in batch and fixed-bed column studies using response surface methodology and artificial neural network", *Journal of Environmental Management*, 227, (2018), 216-228.
- [5]. Ahmadi A., Heidarzadeh S., Mokhtari A.R., Darezereshki E., Harouni H.A., "Optimization of heavy metal removal from aqueous solutions by maghemite (γ -Fe₂O₃) nanoparticles using response surface methodology", *Journal of Geochemical Exploration*, 147, (2014), 151-158.
- [6]. Yılmaz Ş., Zengin A., Şahan T., "A novel material poly(N-acryloyl-L-serine)-brush grafted kaolin for efficient elimination of malachite green dye from aqueous environments", *Colloids and Surfaces A: Physicochemical and Engineering Aspects*, 601, (2020), 125041.
- [7]. Dev V.V., Baburaj G., Antony S., Arun V., Krishnan K.A., "Zwitterion-chitosan bed for the simultaneous immobilization of Zn(II), Cd(II), Pb(II) and Cu(II) from multi-metal aqueous systems", *Journal of Cleaner Production*, 255, (2020), 120309.
- [8]. Corda N., Kini M.S., "Recent studies in adsorption of Pb(II), Zn(II) and Co(II) using conventional and modified materials: a review", *Separation Science and Technology*, 55, (2020), 2679-2698.
- [9]. Olu-Owolabi B.I., Unuabonah E.I., "Adsorption of Zn²⁺ and Cu²⁺ onto sulphate and phosphate-modified bentonite", *Applied Clay Science*, 51, (2011), 170-173.
- [10]. Jemima W.S., Magesan P., Chiranjeevi P., Umapathy M.J., "Sorptions properties of organo modified montmorillonite clay for the reclamation of chromium (VI) from waste water", *Silicon*, 11, (2019), 925-933.
- [11]. Bezerra M.A., Santelli R.E., Oliveira E.P., Villar L.S., Escalera L.A., "Response surface methodology (RSM) as a tool for optimization in analytical chemistry", *Talanta*, 76, (2008), 965-977.
- [12]. Assadian F., Niazi A., Ramezani M., "Response Surface Modeling and Optimization of Effective Parameters for Zn(II) Removal From Aqueous Solution Using *Gracilaria Corticata*", *Journal of Chemical Health Risks*, 10, (2020), 213-224.
- [13]. Yılmaz Ş., Şahan T., Karabakan A., "Response surface approach for optimization of Hg(II) adsorption by 3-mercaptopropyl trimethoxysilane-modified kaolin minerals from aqueous solution", *Korean Journal of Chemical Engineering*, 34, (2017), 2225-2235.
- [14]. Liu X., Han B., Su C.-l., Han Q., Chen K.-j., Chen Z.-q., "Optimization and mechanisms of biosorption process of Zn(II) on rape straw powders in aqueous solution", *Environmental Science and Pollution Research*, 26, (2019), 32151-32164.
- [15]. Biswas S., Bal M., Behera S.K., Sen T.K., Meikap B.C., "Process optimization study of Zn²⁺ adsorption on biochar-alginate composite adsorbent by response surface methodology (RSM)", *Water*, 11, (2019), 325.
- [16]. Kořak A., Lobnik A., Bauman M., "Adsorption of mercury(II), lead(II), cadmium(II) and zinc(II) from aqueous solutions using mercapto-modified silica particles", *International Journal of Applied Ceramic Technology*, 12, (2015), 461-472.
- [17]. Hao J., Han M.-J., Wang C., Meng X., "Enhanced removal of arsenite from water by a mesoporous hybrid material – Thiol-functionalized silica coated activated alumina", *Microporous and Mesoporous Materials*, 124, (2009), 1-7.
- [18]. Li G., Zhao Z., Liu J., Jiang G., "Effective heavy metal removal from aqueous systems by thiol functionalized magnetic mesoporous silica", *Journal of Hazardous Materials*, 192, (2011), 277-283.
- [19]. Mirzaee S.S., Salahi E., Khanlarkhani A., "Kinetics, isotherms and thermodynamic modeling of Mn²⁺ and Zn²⁺ single and binary removal using mercapto functionalized silica aerogel", *Journal of Dispersion Science and Technology*, 40, (2019), 657-667.
- [20]. Rodríguez C.A., Sandoval-Paz M.G., Saavedra R., Trejo-Cruz C., De la Carrera F., Aragon L.E., Sirena M., Delplancke M.-P., Carrasco C., "Comprehensive study of growth mechanism and properties of low Zn content Cd_{1-x}Zn_xS thin films by chemical bath", *Materials Research*, 19, (2016), 1335-1343.
- [21]. Zamani S.A., Yunus R., Samsuri A.W., Salleh M.A.M., Asady B., "Removal of zinc from aqueous solution by optimized oil palm empty fruit bunches biochar as low

- cost adsorbent", *Bioinorganic Chemistry and Applications*, 2017, (2017), 7914714.
- [22]. Tohdee K., Kaewsichan L., Asadullah, "Enhancement of adsorption efficiency of heavy metal Cu(II) and Zn(II) onto cationic surfactant modified bentonite", *Journal of Environmental Chemical Engineering*, 6, (2018), 2821-2828.

Pumice and perlite co-substituted hydroxyapatite: Fabrication and characterization

Serap Gungor Koc

Department of Mechanical Engineering, Faculty of Engineering, Van Yuzuncu Yil University, Van, Turkey,
serapgungor@yyu.edu.tr, ORCID: 0000-0002-4547-0642

ABSTRACT

The purpose of this study was to combine hydroxyapatite (HA) with pumice and volcanic silicate perlite. Doped hydroxyapatite is inexpensive and easy to produce. A precipitation procedure was applied for synthesizing pure and doped hydroxyapatite. Samples were sintered at 1100°C for 1 h. These doped structures are characterized by X-ray Diffraction (XRD), Scanning Electron Microscopy (SEM-EDS) and X-ray Fluorescence. Higher SiO₂ and Al₂O₃ content was shown by XRF analysis. Nanoscale HA is obtained with density of 3.056 g/cm³. The XRD results revealed the existence of the HA, β-TCP and Ca₅(PO₄)₂SiO₄ phases. SEM images confirmed the sintering temperature and number of dopants had significant effect on grain sizes of the samples.

ARTICLE INFO

Research article

Received: 15.11.2020

Accepted: 21.12.2020

Keywords:

Biomaterials,
pumice,
perlite,
precipitation method

1. Introduction

In recent decades, porous ceramics materials are widely used in biomedical applications. Porosity provides reduced weight and widened surface area which allows better mechanical bonding with the host tissues. Hydroxyapatite (HA), Ca₁₀(PO₄)₆(OH)₂, which is in the group of calcium phosphate ceramics, considered biocompatible materials due to their ability to form strong bonds with osteogenic and hard tissues. HA is also used as a coating element in orthopedic and dental implants because of the structural similarities of the HA to apatite minerals in bone and tooth enamel [1-3]. Owing to the low fracture toughness and mechanical properties, HA is frequently used as a filling material in not load-bearing areas. Compressive strength and microhardness values of HA varies between 12 MPa-64 MPa and 85 HV-170 HV, respectively [4]. Recently, studies were carried out to strengthen the low mechanical properties of porous HA and to improve its biological properties. One of these studies is doping HA with different elements [5]. In order to improve internal structure, mechanical, antibacterial and biocompatibility properties HA doped with different cations such as Ti, Y, Ag, Mg²⁺, Sr²⁺ and Al³⁺ instead of Ca ions in the microstructure [6,7]. Mostly, synthetic HA powders are produced by hydrothermal, precipitation, hydrolysis of calcium phosphates, or sol-gel methods. Researches revealed that the mechanical properties of HA are primarily depending on the sintering temperature and particle size. Due to the longer mixing time in the precipitation method compared to other methods, materials

with smaller particle sizes (≤ 50 nm) produced, and therefore secondary phases not formed. The presence of secondary phases significantly reduces the mechanical strength of the material [8]. One of the methods that can be used to improve the mechanical properties of HA is doping with glass-ceramics obtained from silica or phosphate-based bioactive glasses. Studies revealed that composite materials strength and biocompatibility properties increased [9]. When the titanium implant is coated with silicon dioxide doped HA, the corrosion, surface roughness, and osseointegration properties increase compared to the pure HA [10].

In this study, HA has been doped separately with natural pumice and perlite. Pumice is a volcanic rock type that is porous, spongy, light, and highly resistant to atmospheric conditions. As the gases in its body leave the structure as it cools very quickly during its formation, numerous pores formed. Because of these pores, its permeability is low [4]. Pumice, which is resistant to physical and chemical factors, has a porosity ranging from 45% to 70%, and its solubility in water is very low. The density of natural pumice varies between 1.2-1.4 gr/cm³, and its compression strength varies between 1.72 ± 0.12 MPa. The pH value of pumice is around seven and does not show any toxic properties [11]. In vitro tests performed on MG63 cells have shown that pumice increases the proliferation and adhesion of the cells [12]. In another study, it has been demonstrated that the biocompatibility and mechanical properties of HA, which is

doped with 5% natural pumice by weight, compared to pure HA, have increased [13].

Perlite is a silica-based volcanic glass, and it is an amorphous, inert material with low bulk density. Perlite consists of 71-75% silicon dioxide, 12.5 to 18.0% alumina, 1 to 4% sodium and calcium oxide, and traces of metal oxide. The density of perlite, which does not show toxic properties, varies between 0.6-2.30 gm / l, and particle size around 0.2-4 mm [14]. Although, there are many studies focusing on different aspects of perlite, a few studies found on calcium phosphates. From a biomedical point of view, porous composite (ecopore) with perlite surface modified by etching, aminosilane, and combined with fibronectin showed non-toxic and promote human primary osteoblasts growth [15].

The purpose of this study is to synthesize hydroxyapatite (HA) doped with different contents of pumice and perlite to develop new nanocomposite bioceramics and to determine the optimum pumice and perlite contents which yield the best properties in terms of microstructures and mechanical properties. Pure and doped HA synthesized by a precipitation method. The synthesized materials were sintered at 1100°C for 1h. Presence of phases and bonds were characterized by x-ray diffraction (XRD). Grain sizes of the samples were obtained by scanning electron microscopy (SEM). Chemical components of the samples obtained by X-ray fluorescence (XRF).

2. Materials and Method

During the production of samples, HA was doped separately with pumice and perlite particles by using the precipitation method at 1%, 2.5%, and 5% by weight. Due to the longer mixing time in the precipitation method compared to other methods, materials with smaller particle sizes (≤ 50 nm) are produced and therefore secondary phases are not formed. The precursor used in experimental studies were supplied from Sigma-Aldrich. In order to synthesize pure HA, precursor chemicals $\text{Ca}(\text{NO}_3)_2 \cdot 4\text{H}_2\text{O}$ and $(\text{NH}_4)_2\text{HPO}_4$ were separately dissolved in deionized water. NH_4OH was added dropwise to the solution containing $(\text{NH}_4)_2\text{HPO}_4$ in order to pH value 11. NH_4OH was added in $(\text{NH}_4)_2\text{HPO}_4$ and two solutions mixed together to form one solution. The solution, which was stirred for one day at room temperature (24-25°C), was left for one day for precipitation. The wet cake obtained as a result of filtering was dried at 200 °C for 12 hours and then sintered at 1100 °C for 1 hour. After drying and sintering process, pure and doped powders were ground in agate mortar. Pumice and perlite powders were added separately to the ammonium phosphate solution in the amounts indicated in Table 1. The steps used in the production of pure HA are repeated in the production of doped HA. The XRF result, main element oxide percentages (%) of the pumice and perlite powders used in this study are given in Table 2 in terms of weight.

Table 1. The ratio of pumice and perlite added to the doped HA.

Sample	Pumice%mol	Perlite%mol
HA1.0Pumice	1.0	-
HA2.5Pumice	2.5	-
HA5.0Pumice	5.0	-
HA1.0Perlite	-	1.0
HA2.5Perlite	-	2.5
HA5.0Perlite	-	5.0

Table 2. The main oxide percentages elements of pumice and perlite powders (XRF).

	Oxides (Percentage by weight %)						
	SiO ₂	Al ₂ O ₃	Fe ₂ O ₃	CaO	CaCO ₃	K ₂ O	Na ₂ O
Pumice	74.12	13.12	1.66	-	6.04	3.82	1.25
Perlite	76.42	13.94	0.9	3.10	-	4.71	0.16

XRD analysis was carried out to determine the phases in the produced powders. For this purpose, phases were determined by using a scanning speed of 2 °/min at 10-80° 2 θ angles in a Panalytical/Empryan device. Zeiss brand Sigma 300 device was used in SEM analysis. The chemical components of the phases in the microstructure of the powders were determined by the SEM-EDS.

3. Result and Discussion

XRD patterns of the sintered samples (1100°C) were given in Figures 1-2. XRD peaks of the figure 1 consisting of the ICDD main standard peak group with the HA, $\text{Ca}_5(\text{PO}_4)_2\text{SiO}_4$ and β -TCP (ICDD:09-0432, 40-0393, 55-0898). After doping with pumice (1, 2.5 and 5 wt. % Pu-HA) composite composed of mainly HA, with β -TCP as a secondary phase. The diffraction lines of 1, 2.5 and 5 wt. %Pu-HA samples diminished and broadened in comparison with pure HA. That means, 1, 2.5 and 5 wt. %Pu-HA have smaller grain size than pure HA.

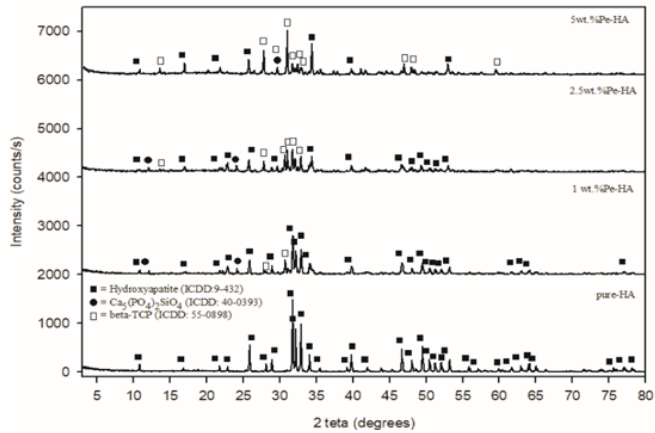


Figure 1. XRD pattern of pure-HA and pumice doped HA (1 wt. %, 2.5wt. % and 5wt. %).

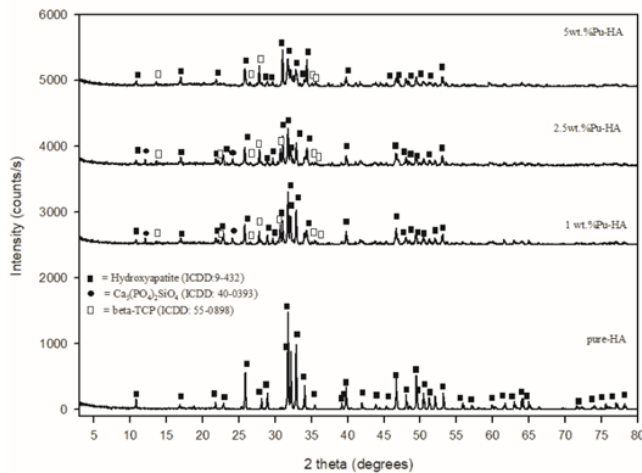


Figure 2. XRD pattern of pure-HA and perlite doped HA (1 wt. %, 2.5wt. % and 5wt. %).

XRD patterns of the HA doped with perlite and sintered at 1100°C (figure 2) are attributed to the phases of β -TCP and/or HA because peaks of β -TCP and HA are overlapping each other. In the case of 2.5wt. %Pe-HA and 5wt. %Pe-HA an increase of the β -TCP observed. Perlite addition increased the crystallinity. Due to perlite doping into peak apatite lattice, peak shift to higher 2θ values with an increase in perlite (5wt. %Pe-HA) content. As seen from the XRD patterns peaks are attributed to β -TCP and/or HA and as a third phase $\text{Ca}_5(\text{PO}_4)_2\text{SiO}_4$ was also observed. In the sample doped with 2.5wt. %Pe-HA ions, most of the HA peaks transformed into β -TCP phase. Because HA, pumice and perlites different thermal expansion coefficients of the crystalline phases (α) may also cause high stresses at the grain boundaries and increase the thermal decomposition of the HA phases [16]. The XRD results reveals that the decomposition rate of HA depends on the mass fraction of pumice among the composites [17].

Figure 3 and figure 4 shows the surface morphology of the pure-HA, (1wt. %-5wt. %) Pu-HA and (1wt. %-5wt. %) Pe-HA composites, respectively. The 1wt. %Pu-HA, 2.5wt. %Pu-HA and 5wt. %Pu-HA composites have porous surface with sponge-like views (Fig. 3b, c and d). When the pumice ratio increased the structure looks differs from homogeneous surface to scarce needle-shaped crystals. The sizes of the pores seem to be increased with respect to the pure-HA.

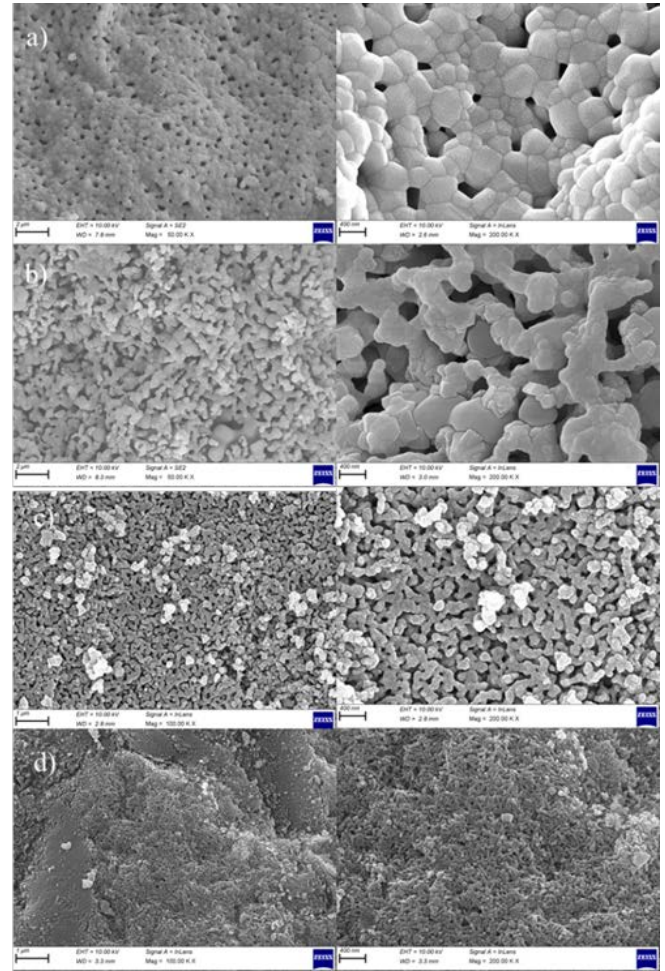


Figure 3. Scanning electron micrograph of the pure-HA (a), 1 wt. %Pu-HA (b), 2.5wt. %Pu-HA (c) and 5wt. %Pu-HA(d).

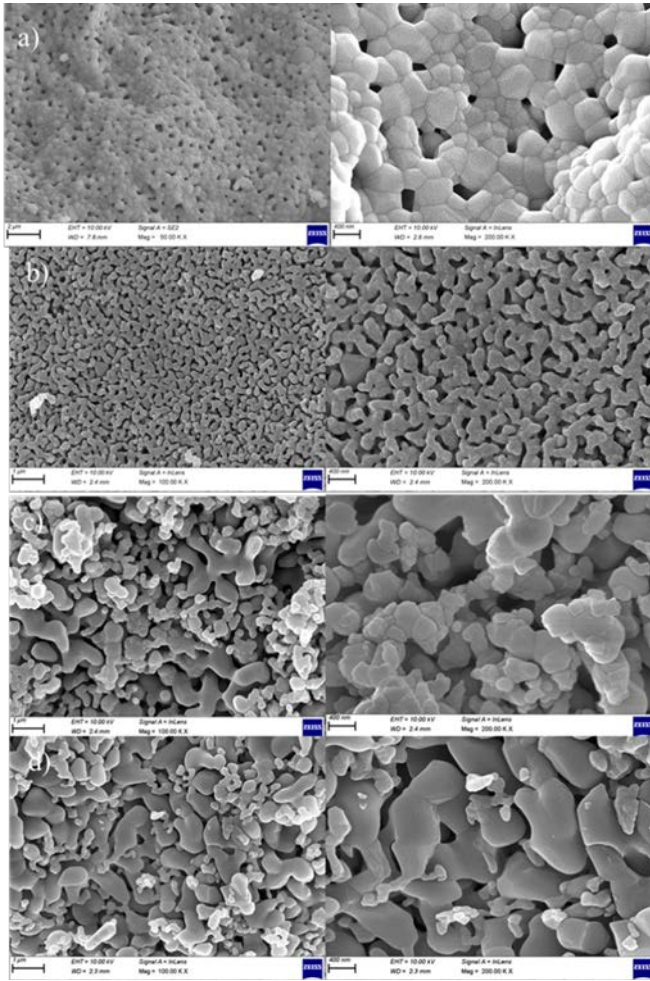


Figure 4. Scanning electron micrograph of the pure-HA (a), 1 wt. %Pe-HA (b), 2.5wt. %Pe-HA (c) and 5wt. %Pe-HA(d).

The changes that occurred in the grain size and morphology of HA due to the ion dopings were observed in SEM images and average grain size measurements. SEM images revealed that temperature and ion amounts of dopants had significant effect on grain sizes of the samples. There is a relationship between amount of dopant and sintering temperature with grain sizes of apatites. SEM results shows that perlite doped HA, especially, 1 wt. %Pe-HA and 2.5wt. %Pe-HA composites have porous surface with sponge-like views (Fig. 4b, c and d). In fig.4b it obvious that there are some cracks on the grains. The reason for cracks could be related to the transformation of HA into β -TCP [18].

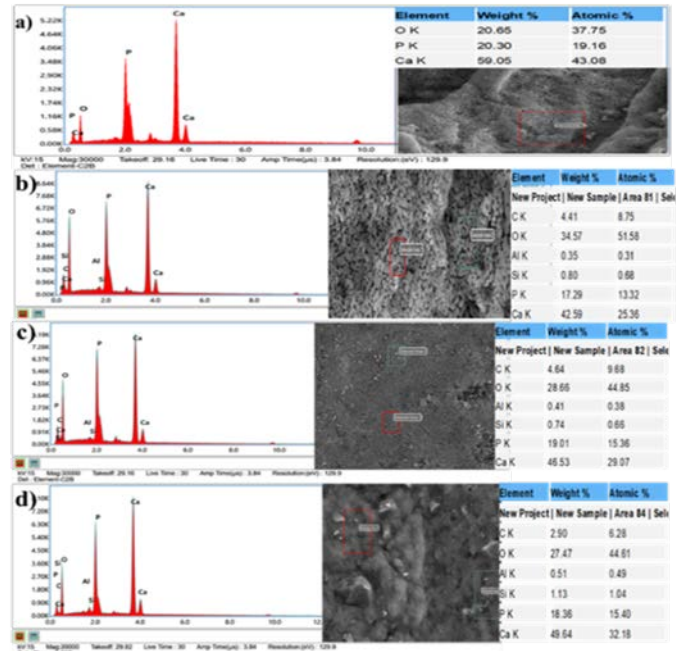


Figure 5. SEM-EDS results of the (a) pure-HA, (b) 1 wt. %Pu-HA, (c) 2.5wt. %Pu-HA and (d) 5wt. %Pu-HA.

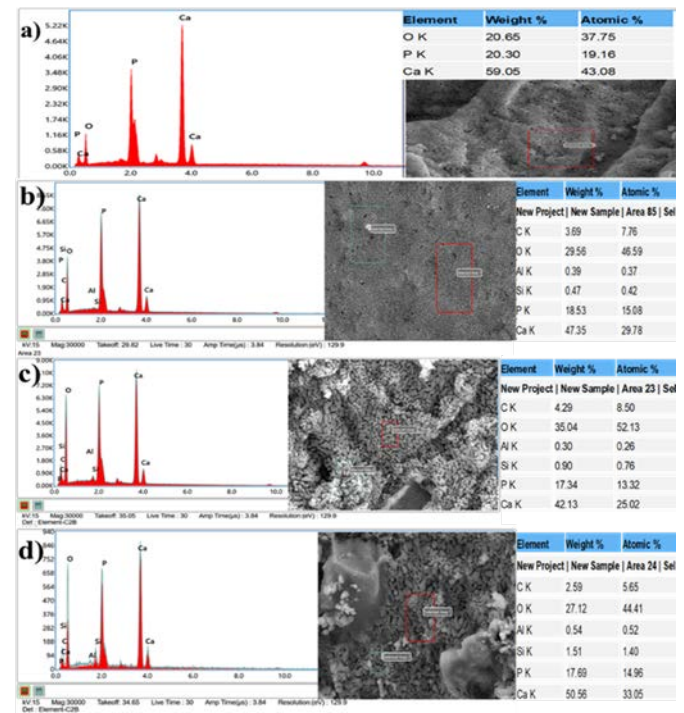


Figure 6. SEM-EDS results of the (a) pure-HA, (b) 1 wt. %Pe-HA, (c) 2.5wt. %Pe-HA and (d) 5wt. %Pe-HA.

The SEM-EDS spectra along with pure-HA, Pu-HA and Pe-HA results were given in fig. 5 and fig. 6. Figure 5'a (pure-HA) comprised of mainly Ca (43.08 at. %), O (37.75 at. %) and P (19.16 at. %). In fig.5(b,c,d) pumice doped HA composed of Ca (25.36-32.18 at.%), O (44.61-51.58 at.%), P

(13.32-15.40 at.%), Si (0.66-1.04 at.%), as well as smaller amounts of Al and C.

Table 3. Density distributions of pumice and perlite doped HA.

Sample (g/cm ³)	Density
HA	3.056
HA1.0Pumice	2.778
HA2.5Pumice	2.727
HA5.0Pumice	2.565
HA1.0Perlite	2.578
HA2.5Perlite	2.282
HA5.0Perlite	2.031

Several studies have been conducted to determine the density of HA. According to literature, the density of HA varies between 3.05-3.1 g/cm³. In those studies, the density of nanoscale HA is about 3.056 g/cm³ this results are compatible with our results (3.056 g/cm³). The lowest density among the doped samples were HA5.0Pumice and HA5.0Perlite which in combination with second phases in SEM results (Table 3) [19].

4. Conclusion

In this study, HA doped with pumice and perlite were synthesized by a precipitation method. Doping amount of pumice and perlite were kept at 1.0-5.0 wt.%. All samples were sintered at 1100°C for 1h. Microstructural and mechanical properties of the sintered samples were investigated via XRD, SEM-EDS and XRF methods. XRD patterns peaks are attributed to β -TCP and/or HA and as a third phase $\text{Ca}_5(\text{PO}_4)_2\text{SiO}_4$ was observed. The diffraction lines of 1, 2.5 and 5 wt. %Pu-HA samples diminished and broadened in comparison with pure HA. That means, 1, 2.5 and 5 wt. %Pu-HA have smaller grain size than pure HA. In this study, Pu-HA and Pe-HA non-toxic composites revealed a remarkable potential for biomedical applications as coating element and bone graft.

References

- [1]. Dorozhkin S.V., "Calcium orthophosphate-containing biocomposites and hybrid biomaterials for biomedical applications", *Journal of Functional Biomaterials*, 6, (2015), 708–832.
- [2]. Gervaso F., Scalera F., Padmanabhan S.K., Sannino A., Licciulli A., "High performance hydroxyapatite scaffolds for bone tissue engineering applications", *International Journal of Applied Ceramics Technology*, 9, (2012), 507–516.
- [3]. Ciobanu G., Ilisei S., Luca C., Carja G., Ciobanu O., "The effect of vitamins to hydroxyapatite growth on porous polyurethane substrate", *Progress in Organic Coating*, 74, (2012), 648–653.
- [4]. Gündüz, L., Yılmaz, İ., 1998. Orta Anadolu Pomza Oluşumlarının Endüstriyel Olarak Kullanılabilirlik Ölçütleri. 4. Endüstriyel Hammaddeler Sempozyumu 118-19 Ekim 2001, İzmir, TÜRKİYE, 214-215.
- [5]. Ciobanu G., Bargan A.M., Luca C., "New bismuth-substituted hydroxyapatite nanoparticles for bone tissue engineering", *JOM*, 67, (2015), 2534–2542.
- [6]. Tahmasebifar A., Gungor S., Evis Z., "The microstructural investigation of nano- calcium phosphates doped with fluoride ions". *Journal of the Faculty of Engineering and Architecture of Gazi University*, 30, (2015), 1-7.
- [7]. Koc G. S., "Synthesis and characterization of strontium and chlorine co-doped tricalcium phosphate". *Materials Letters*, 248, (2019),69-72.
- [8]. Ahn, E.S., Gleason, N.J., Nakahira, A. ve Ying, J.Y., "Nanostructure processing of hydroxyapatite-based bioceramics", *Nano Letters*, 1, (2001), 149-153.
- [9]. Georgiou G., Knowles J.C., "Glass reinforced hydroxyapatite for hard tissue surgery- part 1: mechanical properties", *Biomaterials*, 22, (2001), 2811-5.
- [10]. Bohur B.G., "HVOF Tekniğiyle Ti6Al4V Metal Altlık Yüzeyine Farklı Silika Kaynağı İçeren Biyoseramiklerin Kaplanması", Yüksek Lisans Tezi, Afyon Kocatepe Üniversitesi, Fen Bilimleri Enstitüsü, (2018).
- [11]. Kılınç-Aksay, E., 2005. İzmir-Menderes Yöresi Pomza Cevherinin Kullanımına Yönelik Teknolojik Özelliklerinin Araştırılması, Dokuz Eylül Üniversitesi Fen Bilimleri Enstitüsü Doktora Tezi, 6-7.
- [12]. Li X., Yang W., Zou Q., Zou Y., "Investigation on microstructure, composition, and cytocompatibility of natural pumice for potential biomedical application", *Tissue Engineering Part C*, 16-3, (2010), 427-34.
- [13]. Komur B., Lohse T., Can H.M., Khalilova G., Geçimli Z.N., Aydoğdu M.O., Kalkandelen C., Stan G.E., Sahin Y.M., Sengil A.Z., Suleymanoglu M., Kuruca S.E.,

- Oktar F.N., Salman S., Ekren N., Fıcaı A., Gundez O., "Fabrication of naturel pumice/hydroxyapatite composite for biomedical engineering". *BioMedical Engineering*, (2016), 15:81.
- [14]. Samar M., Saxena S., "Study of chemical and physical properties of perlite and its applications in India", *International Journal of Science Technology and Management*, 5:4, (2016), 70-80,
- [15]. Walter von M at. al. "In vitro behavior of a porous TiO₂/perlite composite and its surface modification with fibronectin". *Biomaterials*, (2005), 26, 2813-2826.
- [16]. Yang C., Guo Y.K., Zhang M.L., "Thermal decomposition and mechanical properties of hydroxyapatite ceramic". *Transactions Nonferrous Metals Society China*. 20, (2010), 254–8.
- [17]. Komur B. et. al. "Fabrication of naturel pumice/hydroxyapatite composite for biomedical engineering", *BioMedical Engineering*, (2016), 15, 81.
- [18]. Mestres G., Le Van C., Ginebra M.P., "Silicon-stabilized α -tricalcium phosphate and its use in a calcium phosphate cement: characterization and cell response". *Acta Biomaterials*, 8(3), (2012), 1169–79.
- [19]. Wu Y., Bose S. "Nano crystalline hydroxyapatite: Micelle templated synthesis and characterization". *ACS Publications*, 21, (2005), 3232-3234.

Investigation of engineering properties of blast furnace slag additive mortars

Hüseyin Boran,^{1,*} Osman Gunaydin,¹ Kadir Gucluer²

¹ Adiyaman University, Faculty of Engineering., Department of Civil Engineering, Adiyaman, Turkey, huseyinboran044@gmail.com, gunaydin@adiyaman.edu.tr, ORCID: 0000-0001-5007-1788, ORCID: 0000-0001-7559-5684

² Adiyaman University, Vocational School of Technical Sciences, Department of Construction, Adiyaman, Turkey, kgucluer@adiyaman.edu.tr, ORCID: 0000-0001-7617-198X

ABSTRACT

Cement, water and fine aggregate mixture is called mortar. Mortar samples suitable for the desired purpose can be obtained by adding various additives to the mortar samples. In this study, instead of standard sand, blast furnace slag (BFS) was used at 10%, 20% and 30% by weight in mortar samples. In order to determine the mechanical properties of the samples, compressive and flexural strength tests were applied. For the electrical resistivity values, a device with constant 30V voltage was prepared and the electrical resistivity values were measured. To determine the freeze-thaw resisting properties, it was applied sodium sulfate experiment. As a result, it was seen that the best values were obtained from 30% BFS additive samples in all series. The highest resistivity values are in the sample with 30% BFS doped with 0.1856 ohm.m and 0.268 ohm.m values. The highest freeze-thaw resisting value was seen in the sample with 30% BFS with 1.35%.

ARTICLE INFO

Research article

Received: 16.09.2020

Accepted: 15.12.2020

Keywords:

Mortar,
blast furnace slag,
electrical resistivity,
sodium sulphate test

*Corresponding author

1. Introduction

A mixture of water and cement is called cement paste. The new mixture obtained as a result of adding a fine aggregate to this mixture is called mortar. Mortars are special concretes that do not contain coarse aggregate. Currently, it is possible to gain main features according to the desired purpose by used mineral and chemical additives in production of mortar [1].

The cost of natural sand used as fine aggregate in recently developed concrete has increased the cost of construction. In this case, research has turned to studies for alternative materials that are cheap and easily accessible for natural sand [2]. To meet the global demand for concrete in the future, finding suitable alternatives to natural aggregates for preparing concrete can become a more difficult task. Therefore, the use of alternative sources for natural aggregates is becoming increasingly important. The use of granulated blast furnace slag (GBFS) aggregates in concrete by replacing natural aggregates is a promising concept because its impact strength is higher than natural aggregate. Steel slag aggregates are already used as aggregates in asphalt paved road mixes due to their mechanical strength, hardness, porosity, abrasion resistance and water absorption capacity [3].

Blast furnace slag (BFS) is a material produced by the melting of iron ore to produce iron metal [4]. The wastes as a result of the burning of limestone, coke and iron ore gangue generate BFS. The formation temperature of BFS is between 1400-1600 °C [5]. The fact that BFS has a crystal structure occurs when it is slowly cooled. In this case, it can be preferred as concrete aggregate and has mechanical properties similar to basalt. On the other hand, rapid cooling is required for the formation of glassy slag [5].

It is known that blast furnace slag improves the workability of fresh concrete, extends the setting time of cement paste, affects hydration rate and perspiration reduction, and strengthens durability values in hardened concrete. Looking at the literature; It has been said that it causes a decrease in the strength gaining speed especially in the first days and an extension of the concrete setting in cold weather conditions [6].

Studies up to now show that slag additive improves concrete characteristics such as durability, permeability, corrosion resistance, workability and strength [7]. The highest electrical resistivity can be achieved with cement mortars containing high levels of BFS. With C-S-H gels reducing the water content in the cement paste as a result of the hydration of free

Ca(OH)₂ and pozzolanic mineral mixtures (containing Al₂O₃, Fe₂O₃, SiO₂ etc.) and accelerates the formation of ettringite-monosulfate [8,9]. As a result of the reaction of BFS particles during hydration, Ca(OH)₂ content decreases and C-S-H gels increase. Thus, it is thought that BFS grains contribute to the formation of C-S-H gels [10].

When the use of BFS as aggregate in the literature and the sulphate strengths of using BFS and pumice instead of a certain amount of aggregate in concrete pipe production; It was observed that the weight loss was the lowest in BFS and pumice added samples. While samples kept in sulphate solution for 180 days showed the best resistance of samples with 15% BFS, while the most unstable sample was the witness sample [11]. Nataraja et al. [12] investigated the use of fine aggregate GBFS in cement mortar. In this study, they changed cement mortar 1: 3 and GBFS at 0, 25, 50, 75 and 100 ratios to natural sand for a fixed w / c ratio of 0%. In the study, they looked at 100% of natural sand change with GBFS for 0.4 and 0.6 w / c ratios. Flow properties of various mixtures and their compressive strength at various ages were investigated. From this study, they observed that the GBFS could be partially used as an alternative building material for natural sand in mortar applications. They found that the reduction in flowability can be compensated for by adding an appropriate percentage of super plasticizer. Babu and Mahendran [13] investigate the physical and mechanical properties of concrete by replacing fine aggregate with BFS and GBFS. Conclusions have been drawn based on the experimental results. Based on their results, it encourages the use of BFS up to 25% in concrete as a substitute for fine aggregate. The maximum compressive strength of 40.39 MPa was obtained by replacing 25% of the fine aggregate with BFS. The use of BFS will reduce the cost of concrete by 8 to 10%. Autade [14] investigated the use of steel slag in concrete instead of fine aggregate. He examined the change in the range of 0, 20, 40, 60, 80, 100%. He observed that the workability of concrete decreases as the percentage of substitution increases. There is a significant increase in compressive strength for 20% and 40% change; It has been stated that there is an increase of more than 20% in flexural strength and tensile strength. With regard to the strength parameters obtained at 80% and 100% substitution, it was stated as expected. 10% - 20% difference in compressive strength has been observed. Seker [15] GBFS is a by-product and its use as aggregate in concrete can be an economical and environmentally friendly solution in the local area. Thus, it will become more important to find suitable alternatives for future aggregates. When the results are examined, it has shown that it has properties similar to natural aggregates and will not cause any harm if it is included in concrete.

The purpose of this study is to use these wastes in the construction sector due to the difficulties of storing by-products that occur as a result of the use of industrial materials and damage to the environment. The selection of blast furnace

slag, which is one of these by-products, as aggregate is to protect the nature, reduce the need for natural aggregate raw materials and to obtain impermeable and high quality mortar samples in terms of durability properties by using thinner materials. For this purpose, BFS additive samples were produced, compressive and flexural strength tests were made, electrical resistivity measurements were carried out and sodium sulfate test was applied.

2. Material and method

In this study, Portland composite cement of CEM II 42.5 type consistent with TS EN 197-1 [16] was used as a binder. Chemical components of cement and BFS used in the study are given in Table 1. BFS's blaine fineness 2685 cm²/gr.

Table 1. Chemical component of cement and BFS

Oxide (%)	SiO ₂	Al ₂ O ₃	Fe ₂ O ₃	CaO	MgO	K ₂ O	Na ₂ O
Cement	19.2	3.88	4.25	62.8	3.42	0.34	2.1
BFS	40.1	12.8	0.9	39.6	4.2	1.2	0.05

CEN standard sand in accordance with TS EN 196-1 [17] was used in the prepared mortar mixtures. The samples have been prepared with reference to 225 gr water, 450 gr cement and 1350 gr standard sand given in TS EN 196-1 [17]. Samples were prepared by replacing 10%, 20% and 30% by weight BFS with standard sand. Mortar samples were prepared in a mixer and placed in molds of 40 × 40 × 160 mm using a shaking table. After the samples were kept in the mold in the laboratory for 24 hours, they were kept in the cure pool at 20±2 °C for 7, 28 and 90 days experiments. The samples produced 3 pieces for each series were first subjected to the flexural strength test and the average values of the results calculated with the help of formula (1) were taken and the flexural strength values were accepted. Compressive strength test was performed on the samples obtained after flexural strength and the average of the results calculated with the help of formula (2) was accepted as the value of compressive strength.

$$R_f = \frac{1.5 \times F_f \times l}{b^3} \quad (1)$$

Here; R_f: Flexural strength, (Newton / mm²), b: Side length of the square section of the prism (mm), F_f: The force applied to the middle of the prism when it breaks (Newton), l: The distance between the support cylinders (mm)

$$f_b = \frac{P_k}{A_0} \quad (2)$$

Here; f_b = Compressive strength (MPa), A₀ = Surface area (mm²), P_k = Load at break (N)

For electrical resistivity measurements, the resistivity values of the samples were calculated with the help of formulas (3) and (4) by giving a constant 30 V voltage to the samples.

$$\rho = R \times \frac{S}{L} \quad (3)$$

$$R = \frac{U}{I} \quad (4)$$

Here; ρ = electrical resistivity ($\Omega \cdot m$); R is the measured resistance (Ω); L , distance between copper electrodes (m); S , electrode conductor area (m^2); Voltage value (volts) on U Electrodes; I The current intensity (amperes) passing through the sample.

For the sodium sulphate test, the solution was prepared by adding 350 g of sodium sulphate to 1 liter of water in accordance with ASTM C88-05 [18]. The samples were weighed as it is the state of driving oven before the experiment. The samples placed in the solution were kept between 16-18 hours. The samples removed from the solution were placed in the oven and kept in the oven at 105 °C for about 4-6 hours until they reached their constant weight. This cycle was repeated 5 times, and as a result, the oven-dried samples were weighed. With the help of formula (5), freezing loss values were calculated. Finally, samples were subjected to compressive strength test. Compressive strength values of the samples were calculated with the help of formula (2).

$$\frac{(G_1 - G_2)}{G_1} \times 100 \quad (5)$$

G_1 : The oven-dry weight of the samples before sodium sulphate the test,

G_2 : The oven-dry weight of the samples after sodium sulphate the test

3. Findings

3.1. Compressive and Flexural Strength Findings

The compressive and flexural strength findings of the mortars used in 10%, 20% and 30% rates from BFS are given in Fig. 1 (a) and (b).

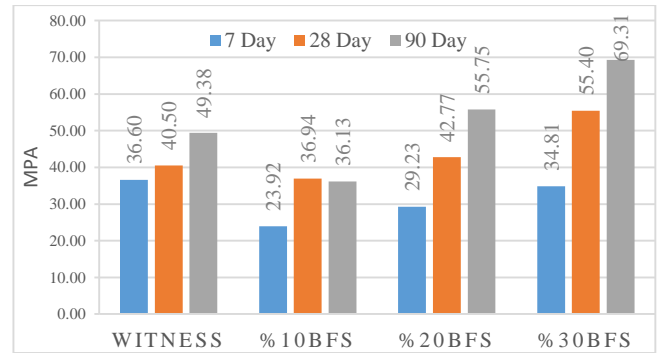


Figure 1 (a) Compressive strength findings

Looking at the compressive strength results, it was seen that the 7-day early strength was the highest with 36.6 MPa in the witness sample. It was observed that the samples with 20% and 30% BFS additive were higher than the witness sample at 28 and 90 days values, but the highest values were in the sample with 30% BFS additive with 69.31 MPa. In the literature studies, it has been stated that the use of BFS reduces early strengths, but this effect largely disappears in later ages [19]. Quasrawi et al. [20], in their study, as a result of the replacement of fine aggregate and BFS, samples with BFS additives at the rate of 15-30% obtained the best results for compressive strength. The results obtained support this view. It is reported that the early age strength of slag reinforced concrete is lower than that of normal Portland cement concrete, whereas the final strength is equal or higher than the strength of normal Portland cement concrete, provided that it is cured well [21-22]. It can be said that the use of BFS as a mineral additive in certain proportions and its use as fine aggregate yields better compressive strength results compared to witness samples.

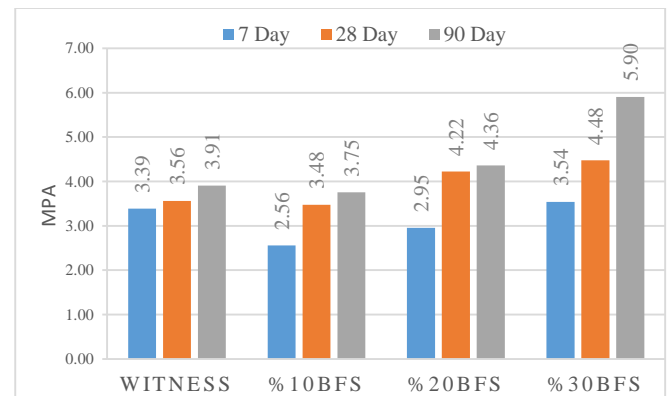


Figure 1 (b) Flexural strength findings

When the flexural strength findings were examined, it was seen that the witness sample was greater than 10% and 20% BFS added sample at 7-day early strength, but the highest value with 3.54 MPa was found in the sample with 30% BFS added. When the values of 28 and 90 days are examined, it

was seen that the lowest values were at 3.48 MPa and 3.75 MPa in the sample with 10% BFS and the highest values were in the sample with 4.48 MPa and 5.9 MPa with 30% BFS. When the comparison is made from the literature, Quasrawi et al. [20], in their study, as a result of the replacement of fine aggregate and BFS, samples with BFS additives at 30-50% have obtained the best results for flexural strength. The findings obtained support this view. Slag concretes with tensile strength have slightly higher tensile strength than Portland cement concrete for a given compressive strength [23]. It can be said that by using BFS as a mineral additive in certain proportions, its use as fine aggregate yields better flexural strength results compared to witness samples.

3.2. The Electrical Resistivity Findings

The electrical resistivity findings of the mortars used at 10%, 20% and 30% rates from BFS are given in Fig. 2.

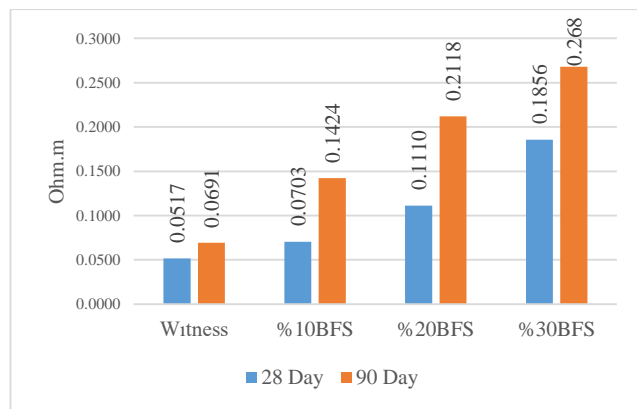


Figure 2 The electrical resistivity findings

When the electrical resistivity findings were examined, it was seen that the lowest values were in the witness sample with 0.0517 ohm.m and 0.0691 ohm.m values. The resistivity value increased with the increase in the amount of BFS. The highest values are in the sample with 30% BFS doped with 0.1856 ohm.m and 0.268 ohm.m values. Topçu et al. [10] in their study, they think that adding BFS to cement paste increases the electrical resistivity of the mixtures. Considering the values obtained above and the values obtained from this study, it can be said that preferring BFS as both mineral additive and fine aggregate gives better results than witness samples. Increasing electrical resistivity decreases electrical conductivity. As a result, it is seen that the most conductive sample is the witness sample and the least conductive one is the sample with 30% BFS doping.

3.3. Sodium Sulphate Findings

Findings of sodium sulphate belonging to the mortars used in 10%, 20% and 30% rates from BFS are given in Figure 3.

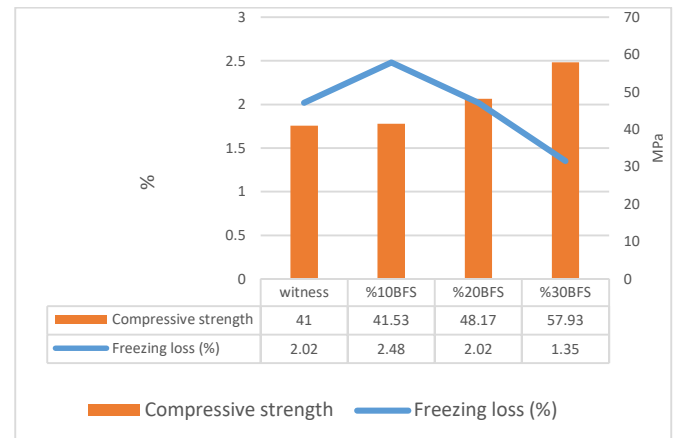


Figure 3 Sodium sulphate findings

Considering the sodium sulphate test findings, the lowest compressive strength is in the witness sample with 41 MPa. The increase in BFS positively affected the compressive strength. The highest compressive strength is 57.93 MPa with 30% BFS added sample. The increase in the amount of BFS caused a decrease in freezing loss. As a result, the lowest freezing loss value was seen in the sample with 30% BFS with 1.35%. Binici et al. [20] obtained the lowest mass loss among the samples with high contribution from blast furnace slag. They also stated that blast furnace slag additive contributes positively to durability and strength. These studies confirm the results obtained above.

4. Results

Considering the findings obtained by adding BFS to the mortar samples instead of fine aggregate at the rates of 10%, 20% and 30%,

- It has been observed that increasing the amount of BFS has a positive effect on compressive strength. The fact that the witness sample has the highest value in 7-day early strength is thought to be due to the fact that mineral additives have an effect on reducing the cement setting speed.
- When looking at 7, 28 and 90 days values, it was seen that the highest flexural strength values were 3.54 MPa at 7 days, 4.48 MPa at 28 days and 5.9 MPa at 90 days in the sample with 30% BFS.
- The increase in the amount of BFS has also increased the electrical resistivity value. It was observed that the highest value was at 0,268 ohm.m with 30% BFS additive sample. Parallel values were obtained with the compressive strength values. Since it is known that increasing the electrical resistivity decreases the electrical conductivity, the best

conductive witness sample is considered to be the least conductive 30% BFS additive sample.

- The increase in the amount of BFS, an increase in compressive strength has been observed under the presence of sodium sulphate. The lowest freezing loss with a value of 1.5% is in the sample with 30% BFS. In addition, it has been observed that the increase in the amount of BFS reduces the freezing loss.

- It is recommended to use the 30% BFS additive sample in mortar concrete since it is seen that the best values are obtained in terms of durability and strength.

- It can be said that the use of BFS, which is an industrial waste, in concrete or mortars at certain rates for recycling and environmental protection is not considered harmful in terms of its mechanical and durability properties.

References

- [1]. Baradan B., Yazıcı H. ve Aydın S., Beton. Dokuz Eylül Üniversitesi Mühendislik Fakültesi Yayınları, İzmir: 2015.
- [2]. Jadhav, P.A. ve Kulkarni, D.K., "Effect of Replacement of Natural Sand By Manufactured Sand on the Properties of Cement Mortar," International Journal of Advanced Engineering Technology, Vol. 3, No 3, (2013).
- [3]. Hiraskar, K.G. ve Patil, C. "Use of Blast Furnace Slag Aggregate in Concrete," International Journal Of Scientific & Engineering Research, Volume 4, Issue 5, (2013), s 95.
- [4]. Thomas D., Concrete Durability. CRC Press, 2014.
- [5]. Babu K. D. and Kumar V. S. R., "Efficiency of GGBS in Concrete", Cement and Concrete Research, 30, (2000), 1031- 1036.
- [6]. Erdoğan T. Y., Beton. Metu Press, 5. Baskı, 2015.
- [7]. Babu K. D. and Kumar V. S. R., "Efficiency of GGBS in Concrete", Cement and Concrete Research, 30, (2000), 1031- 1036.
- [8]. Salem T.M., "Electrical conductivity and rheological properties of ordinary portland cement-silica fume and calcium hydroxide-silica fume pastes", Cem Concr Res, 32, (2002), 1473-1481.
- [9]. McCarter W.J., Starrs G. and Chrisp T.M., Electrical conductivity, diffusion, and permeability of portland cement-based mortars, Cem Concr Res, 30, (2000), 1395-1400.
- [10]. Topçu İ. B., Uygunoğlu T. ve Hocaoglu İ., "Yüksek fırın cüruf katkılı çimento pastalarının elektriksel özdirençlerinin araştırılması", Politeknik Dergisi, 21(2), (2018), 257-264.
- [11]. Binici H. et al, "Kum Boyutunda Yüksek Fırın Cürufu ve Pomza Katkılı Beton Boruların Durabilite Özelliklerinin Araştırılması", Kahramanmaraş Sütçü İmam Üniversitesi Mühendislik Bilimleri Dergisi, 14.3, (2012), 33-44.
- [12]. Nataraja, M.C., Kumar, D.P.G., Manu, A.S. ve Sanjay, M.C., "Use Of Granulated Blast Furnace Slag As Fine Aggregate In Cement Mortar," International Journal of Structural and Civil Engineering Research. No.2, May, (2013).
- [13]. Babu, J.S. ve Mahendran, N., "Experimental Studies on Concrete Replacing Fine Aggregate with Blast Furnace Slags," International Journal of Engineering Trends and Technology (IJETT). Volume 10, Number 8, Apr, (2014).
- [14]. Autade, P. B., & Saluja, H. S. J. S. Effect of Steel Slag as a Replacement of Fine Aggregate in M40 Grade of Concrete, 2016.
- [15]. Şeker, O., "Granüle Yüksek Fırın Cürufunun Kendiliğinden Yerleşen Beton Özelliklerine Etkisi," Master's thesis, Bartın Üniversitesi, Fen Bilimleri Enstitüsü, 2019.
- [16]. Çimento-Genel Çimentolar-Bileşim, Özellikler ve Uygunluk Kriterleri, TS EN 197-1, 2002.
- [17]. Çimento Deney Metotları-Dayanım Tayini, EN 196-1, 2002.
- [18]. Standard Test Method for Soundness of Aggregates by Use of Sodium Sulfate or Magnesium Sulfate, ASTM C88-05, 2005.
- [19]. Yazıcı H., "Yüksek fırın cürufu katkılı harçların sülfat dayanıklılığının incelenmesi", DEÜ Mühendislik Fakültesi Fen ve Mühendislik Dergisi, 8, 1, (Ocak 2006), 51.
- [20]. Qasrawi, H., Shalabi, F., & Asi, I., "Use of low CaO unprocessed steel slag in concrete as fine aggregate," Construction and Building Materials, 23(2), (2009), 1118-1125.

- [21]. Soroka I., "Concrete in Hot Environments", National Building Research Institute, Faculty of Civil Engineering, Technion-Israel Institute of Technology, Haifa, Israel, 1993.
- [22]. Yeau K. Y. and Kim E. K., "An Experimental Study on Corrosion Resistance of Concrete with Ground Granulated Blast-Furnace Slag", Cement and Concrete Research, 35, (2005), 1391-1399.
- [23]. Newman J., and Choo B.S., "Advanced Concrete Technology", Elsevier Publishing, Great Britain, 2003.
- [24]. Binici H., Eken M. ve Dinçer A., "Silis Dumanı, Uçucu Kül ve Yüksek Fırın Cürufu Katkılı Betonların Bazı Durabilite Özellikleri", Çukurova Üniversitesi Mühendislik-Mimarlık Fakültesi Dergisi, 28(1), (2013), 11-21.

Forecasting COVID-19 Cases based on mobility

Mehmet Şahin

Iskenderun Technical University, ORCID: 0000-0001-7078-7396

ABSTRACT

Countries struggling to overcome the profound and devastating effects of COVID-19 have started taking steps to return to the "new normal." Any accurate forecasting can help countries and decision-makers make plans and decisions in returning to normal life. In this regard, it is needless to mention the criticality and importance of accurate forecasting. In this study, daily cases of COVID-19 are estimated based on mobility data, considering the proven human-to-human transmission factor. The data of seven countries, namely Brazil, France, Germany, Italy, Spain, the United Kingdom (UK), and the United States of America (USA), are used to train and test the models. These countries represent around 57% of the total cases in the whole world. In this context, various machine learning algorithms are implemented to obtain accurate predictions. Unlike most studies, the predicted case numbers are evaluated against the actual values to reveal the methods' real performance and determine the most effective methods. The results indicated that it is unlikely to propose the same algorithm for forecasting COVID-19 cases for all countries. Also, mobility data can be enough to predict the COVID-19 cases in the USA.

ARTICLE INFO

Research article

Received: 15.07.2020

Accepted: 13.12.2020

Keywords:

COVID-19;
forecasting;
mobility;
human-to-human
transmission;
coronavirus

1. Introduction

Coronavirus disease 2019 (COVID-19) pandemic, causing 6,799,713 confirmed cases and 397,388 deaths in 216 countries as of June 7, 2020, has had impacts that are difficult to recover in the short term [1]. The outbreak affected people's health and lifestyles and brought problems such as the global economic downturn, psychological distress, and adverse effects on daily activities [2]. To minimize or eliminate such problems, countries have taken various public policy decisions regarding health, social, and economical. When making such short- or long-term decisions, predictions regarding the outbreak are crucial inputs.

Considering valid parameters in estimates significantly affects the accuracy of the results, the mobility variable is considered significant in predicting COVID-19 cases. This situation can be explained as follows. Various factors contribute to the global spread of infectious diseases, including increased speed and reach of human mobility and increased volumes of trade and tourism [3]. As an infectious disease, COVID-19 caused the suspension of international and domestic flights and lockdown restrictions in many countries [4, 5]. Such radical decisions, proving that mobility is a significant parameter, were made to minimize mobility and hence human-to-human transmission [6]. Human-to-human transmission happens

through the respiratory droplets released when infected patients sneeze or cough [7].

Recent studies also claimed that mobility and human-to-human transmission are effective factors in the spread of COVID-19 [8-10]. In addition, Kraemer, Yang [11] analyzed the impact of human mobility in China and found that the mobility statistics provided a precise record of the spread of COVID-19 among Chinese cities in early 2020. Tagliazucchi, Balenzuela [12] considered mobility through utilizing cell phone data to model the expansion of the COVID-19 in Argentina.

It can be concluded that the mobility of people and the population are the primary sources of human-to-human transmission. Therefore, these two factors are included in the prediction models in this study. This study's main objective is to assess the impact of mobility and determine the most effective methods in predicting daily COVID-19 cases. In this context, numerous machine learning models are formed. To train and test the models, the data of seven countries, namely Brazil, France, Germany, Italy, Spain, the United Kingdom (UK), and the United States of America (USA), are used. These countries had approximately 57% of the total number of cases in the world as of May 26, 2020. Thus, more than half of the total COVID-19 cases are involved in the analysis. Although Russia has many confirmed cases, it was excluded

from the analysis as the detailed mobility data do not exist for the country.

There have been some studies based on forecasting COVID-19 cases. Yousaf, Zahir [13] estimated COVID-19 cases, recoveries, and deaths in Pakistan through Auto-Regressive Integrated Moving Average Model (ARIMA). In addition, some other studies predicted daily cases and deaths, alone or together in different countries. Salgotra, Gandomi [14] predicted confirmed cases and death cases in India; Ayinde, Lukman [15] proposed and compared several models for COVID-19 cases in Nigeria; Mandal, Jana [16] predicted cases in three states on India; Parbat and Chakraborty [17] implemented support vector regression to predict cases in India; Chimmula and Zhang [18] predicted COVID-19 transmission in Canada; and Fanelli and Piazza [19] predicted cases in China, France, and Italy. It can be inferred that different models were adopted to forecast COVID-19 cases in one country in general. Unlike other studies, in the present study, seven countries are included in the analysis, and the predicted cases are evaluated against actual cases. Also, updated real data are used. Considering the data size is significant in analyzing machine learning methods, the present study also contributes to the literature using the most recent and considering a broader timeframe than earlier studies. To the best of my knowledge, no reports or studies are available in literature at the time of preparing this study, which uses the most up-to-date and such broad data, addresses several countries, and evaluates the prediction results against real cases. Therefore, the purpose of this study constitutes the first successful and complete in determining the most effective methods for predicting daily COVID-19 cases considering seven countries by using updated data and evaluating the predicted results with real data.

2. Materials and methods

2.1. Study Area

Seven countries, namely Brazil, France, Germany, Italy, Spain, the UK, and the USA, are considered in the analysis. As mentioned earlier, these countries represent approximately 57% of the total cases worldwide as of preparing the present study. These are the countries most affected by the COVID-19 pandemic in terms of the total case. Figure 1 presents the daily cases of each country. Most cases were located in the USA, followed by Spain, Brazil, the UK, Italy, Germany, and France as of May 20, 2020 [20].

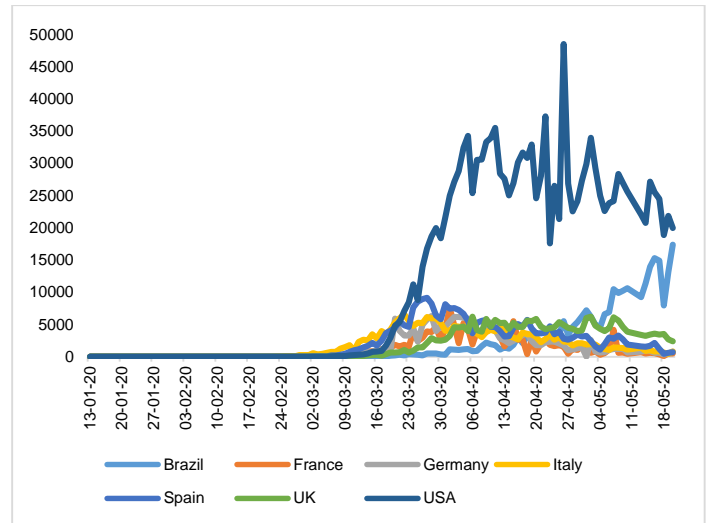


Figure 1. Daily COVID-19 cases in each country

2.2. Data

The mobility data were obtained from Apple Mobility Trends Reports (<https://www.apple.com/covid19/mobility>). Figures 2, 3, and 4 demonstrate the comparison of driving, transit, and walking indices of countries, respectively. The data for May 11 – 12 is not available. Therefore, the data from Jan 13, 2020 to May 10, 2020 were used for training the models, and the data from May 13, 2020 to May 20, 2020 were used to test the models. The beginning of the training data was determined, considering the incubation period of COVID-19 changes from 1 day to 14 days [21]. Besides, the daily cases were obtained from the EU Open Data Portal [20].

Figure 2 illustrates that countries' driving index differs; however, there is a similar trend for all. In other words, a sharp decrease in March and an increasing tendency afterward can be observed in the figure. Remaining the highest for a while and falling to the lowest values, Spain's index can be the summary of the story of this country once being the epicenter of COVID-19.

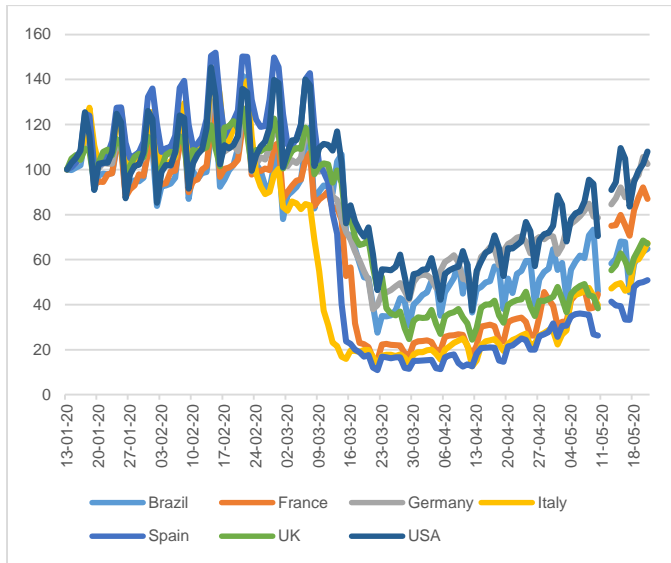


Figure 2. Driving index of countries

Figure 3 presents the comparison of transit indices of the countries. Higher values for Germany and Spain in the early stages are seen. Besides, the highest transit indices were measured in Germany in the later period.

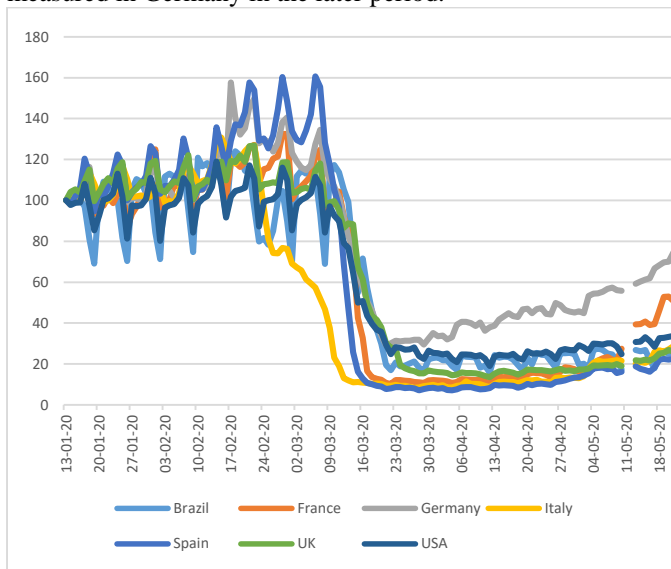


Figure 3. Transit index of countries

Figure 4 illustrates the comparison of the walking indices of the countries. This trend is similar to the previous two. The highest values in the UK in the early period, in Spain in the following period and Germany in the near future stand out.

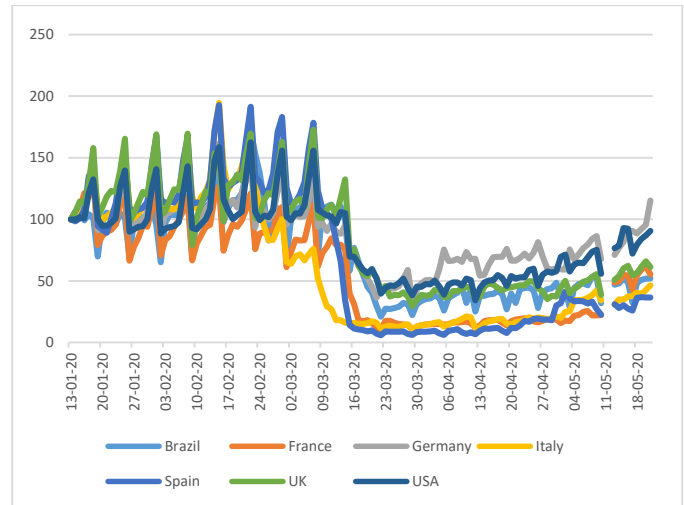


Figure 4. Walking index of countries

2.3. Description of the Methods

The methods are briefly described as follows:

1. *Linear Regression Models* deliver an output (prediction) based on a linear combination of inputs. The significant advantages of these models are ease of application and interpretability. However, these models can deliver misleading predictions if the relationship between input and output cannot be reasonably interpreted through a linear function.
2. *Gaussian Process Regression Models* are based on a practical and probabilistic approach to learning [22]. Gaussian process regression (GPR) models represent a probabilistic method appropriate for nonlinear regression problems. These models can deal with complex problems that have different features, including small samples, nonlinearity, and high dimensions. They can detect uncertainty and deliver compelling predictions.
3. *Support Vector Machine (SVM)* is implemented for regression, time-series, and classification problems owing to its optimal global capacity, flexibility, forecasting ability, and minimal overfitting issues being one of the common issues in modeling high-dimensional data [23].
4. *Decision Tree* defines a dependent variable as a function of numerous independent variables. As practical algorithms, Decision Trees allow dealing with different response data types, including numeric, categorical ratings. Also, they can process missing data in both independent and dependent variables. Boosted and bagged procedures are the two most commonly used approaches. Boosted is for joining multiple classifiers to deliver better

performance compared to the individual classifier alone. Bagged is for producing several versions of a predictor through bootstrap replicates of the training data set and integrating them to better accuracy. These two procedures differ in how data are resampled [24].

5. *Ensemble Learning (EL)* comprises various learners that help to deliver accurate predictions for a given problem. Less prone to a potential data overfitting problem than a single learner and improved generalization abilities make it preferable [25].

2.4. Implementation of the Algorithms

The mobility indices and populations of the countries are used as inputs to reveal whether these are enough to forecast daily COVID-19 cases through machine learning techniques. In this context, numerous machine learning methods are implemented. The training data are used to train each approach. Then, each model's performance is evaluated against actual data in each country observed from May 13, 2020 to May 20, 2020. Thus, the models are evaluated in general and country-specific. The performance of each model is assessed based on the mean absolute percentage error.

Table 1. Confirmed COVID-19 cases and forecasted cases in the USA

Date	Confirmed Cases	Rational Quadratic GPR	Linear Regression	Fine Tree	Cubic SVM	Ensemble Boosted Trees
5/13/2020	22048	23896	29392	24781	33100	24703
5/14/2020	20782	23519	30250	24781	33008	24703
5/15/2020	27143	22284	34311	24781	34630	23880
5/16/2020	25508	21777	34939	24781	38595	24703
5/17/2020	24487	23781	29449	28857	36104	24703
5/18/2020	18873	19360	30271	24781	33083	24703
5/19/2020	21841	17847	32074	24781	34357	24703
5/20/2020	19970	16229	33054	24781	34919	23880

To analyze the errors, mean absolute percentage errors were calculated, as given in Table 2. To be noted that only the best performing approach for each method group (linear regression, Gaussian process regression, support vector machine, decision tree, and ensemble learning) is given. The results reveal that the rational quadratic GPR provided the

Table 2. The mean absolute percentage errors of predictions in the USA

Rational Quadratic GPR	Linear Regression	Fine Tree	Cubic SVM	Ensemble Boosted Trees
12.07%	41.91%	16.24%	55.34%	13.82%

In addition, the lowest mean absolute percentage errors were provided for Brazil, the United Kingdom, and Germany by linear regression (20.69%), linear regression (30.14%), and rational quadratic GPR (47.03%), respectively. The errors for Spain, Italy, and France were at unacceptable levels. In other

3. Results and discussion

The results showed that it is impossible to forecast daily COVID-19 cases in all countries based on the mobility index through machine learning methods. This outcome may result from the spread of COVID-19 cases to be chaotic or an indication that the mobility index and population are not sufficient as inputs. The first case seems more relevant. Arias Velásquez and Mejía Lara [26] claimed that the COVID-19 pandemic has behaved in changing ways and unpredictable in all countries, depending on the factors used in its treatment. It is a fact that every country has written its own story during the COVID-19 pandemic. Countries differ in factors such as treatment methods, monitoring the number of infected patients, adequate health infrastructure, mortality rates, and the number of tests performed. All these factors directly or indirectly determine the number of COVID-19 cases in a country. Therefore, it can be inferred that it is more reasonable to evaluate each country separately with the results obtained.

The most accurate forecasting results were obtained for the USA. Table 1 presents the actual and predicted COVID-19 cases from May 13, 2020 to May 20, 2020 in this country.

most accurate predictions, followed by ensemble boosted trees and fine trees, considering that low mean absolute percentage error values indicate better estimations. Also, the percentage error of Cubic SVM is higher than 50%, meaning that forecasting is inaccurate.

words, the machine learning methods based on the mobility index data could not provide accurate results for these three countries. The forecasting accuracy might be improved by including more parameters in the analysis.

Some results can be outlined. First, numerous machine learning methods were implemented to forecast daily COVID-19 cases in seven countries. Based on these countries' results, it is not possible to recommend the same model for all countries. In other words, no model provided accurate predictions for all countries. This outcome is consistent with the study conducted by [27]. Shahid, Zameer [27] used machine learning methods to forecast COVID-19 cases and evaluated different models' performance, including deep learning. In this regard, they considered ten countries, namely Brazil, China, Germany, India, Israel, Italy, Russia, Spain, the UK, and the USA. According to their results, long short-term memory (LSTM) provided the best predictions for China's confirmed cases and deaths. However, primarily, the present study results reveal that rational quadratic GPR can be used to predict daily COVID-19 cases in the USA. This result may be consistent with the reason for the studies considering just one country in their analyses. In this context, Tomar and Gupta [28] implemented methods such as LSTM to predict the number of COVID-19 cases in India and posited that the proposed method was effective. Arora, Kumar [29] applied deep learning methods such as recurrent neural network-based LSTM to forecast and analyze COVID-19 positive cases in India, and the proposed method produced high accuracy with an error of less than 3% for daily prediction results and less than 8% for weekly results. Alzahrani, Aljamaan [30] implemented the ARIMA model to predict the spread of the COVID-19 pandemic in Saudi Arabia and found that the proposed ARIMA model outperformed other models. The results also indicated that mobility data were not enough to predict cases in Spain, Italy, and France. Several other studies implemented machine learning approaches for different countries. Ribeiro, da Silva [31] implemented machine learning methods for estimating the cumulative confirmed COVID-19 cases in Brazil and claimed that support vector regression and stacking-ensemble learning model could be used to estimate COVID-19 cases. Sujath, Chatterjee [32] applied machine learning methods to forecast cases in India and posited that multilayer perceptron provided more accurate results than linear regression. Tuli, Tuli [33] implemented machine learning models to forecast the growth and trend of COVID-19 pandemic considering various countries and obtained different results for each country. Wang, Zheng [34] applied logistic model and machine learning methods to predict the COVID-19 trend globally, in Brazil, India, Indonesia, Peru, and Russia and estimated that the global peak would be in late October. The number of studies can be extended. Last, machine learning methods can handle extensive data and provide successful results. A larger dataset might improve the accuracy of the forecasting.

The present study might have some limitations. First, the mobility parameters that reflect the impact of human-to-human transmission were considered in this study. Although the predicted results indicated that the mobility variables were enough to estimate COVID-19 cases in the USA, more

variables might improve forecasting results' accuracy. Meteorological parameters were found to be effective in COVID-19 cases [21, 35-38]. However, the fact that the COVID-19 pandemic has affected countries without regard to their development level reflects that the use of many parameters, such as economical in the COVID-19 prediction, can be misleading and unsuccessful. Second, each country has followed different strategies, and its strategies determine the expansion of COVID-19 cases. Thus, not including the specific actions taken by countries might cause inaccurate predictions in some countries. Last, due to machine learning methods producing significant results based on extensive data, conducting similar analysis after a while may increase the accuracy of results. Overall, it can be concluded that it may not be easy to propose a general model for forecasting COVID-19 cases in each country at the moment.

To sum up, the USA's recent protests have proven the mobility effect on the spread of COVID-19. Standing in the crowd for a long time increases the risk of transmission of COVID-19. It is believed that the protests created chaos, violence, and protests that can further trigger cases of COVID-19 [39]. The present study and tangible cases prove that the mobility data are crucial inputs on forecasting COVID-19 cases. Admittedly, additional variables may be required for higher accurate predictions.

4. Conclusions

Unlike other studies, this study analyzed whether COVID-19 cases could be predicted based on mobility data alone. In this context, various machine learning models were implemented to forecast daily COVID-19 cases in Brazil, France, Germany, Italy, Spain, the UK, and the USA. Using the real data of these countries, the models were trained and tested with the actual number of cases.

The results indicated that it was not possible to use the same model for all countries. This outcome is in line with the real-life situation as each country has followed different strategies to fight the COVID-19 pandemic. The results also revealed that the rational quadratic GPR could be used to predict COVID-19 cases in the USA. It is worth reminding that this model has achieved this only with mobility and population data. However, the mobility and population data alone could not yield useful results in estimating the number of cases in Spain, France, and Italy.

Including some other parameters such as meteorological and economical in the models, using different models, and analyzing each country separately may increase the results' effectiveness. These may be situations to consider for future work.

References

- [1]. World Health Organization, Coronavirus disease (COVID-19) Situation Report–139, (2020).
- [2]. El Zowalaty M.E., Järhult J.D., “From SARS to COVID-19: A previously unknown SARS-CoV-2 virus of pandemic potential infecting humans–Call for a One Health approach”, *One Health*, (2020), 100124.
- [3]. Findlater A., Bogoch I.I., “Human mobility and the global spread of infectious diseases: a focus on air travel”, *Trends in parasitology*, 34(9), (2018), 772-783.
- [4]. Alandijany T.A., Faizo A.A., Azhar E.I., “Coronavirus disease of 2019 (COVID-19) in the Gulf Cooperation Council (GCC) countries: Current status and management practices”, *Journal of Infection and Public Health*, 13(6), (2020), 839-842.
- [5]. Al-Tawfiq J.A., Memish Z.A., “COVID-19 in the Eastern Mediterranean Region and Saudi Arabia: prevention and therapeutic strategies”, *International Journal of Antimicrobial Agents*, 55(5), (2020), 105968.
- [6]. Zhu Y., et al., “The mediating effect of air quality on the association between human mobility and COVID-19 infection in China”, *Environmental Research*, 189, (2020), 109911.
- [7]. Wang J., Du G., “COVID-19 may transmit through aerosol”. *Irish Journal of Medical Science (1971 -)*, 189(4), (2020), 1143-1144.
- [8]. Phan, L.T., et al., “Importation and human-to-human transmission of a novel coronavirus in Vietnam”, *New England Journal of Medicine*, 382(9), (2020), 872-874.
- [9]. Riou J., Althaus C.L., “Pattern of early human-to-human transmission of Wuhan 2019 novel coronavirus (2019-nCoV), December 2019 to January 2020”, *Eurosurveillance*, 25(4), (2020), 2000058.
- [10]. Muhammad S., Long X., Salman M., “COVID-19 pandemic and environmental pollution: A blessing in disguise?”, *Science of The Total Environment*, 728, (2020), 138820.
- [11]. Kraemer M.U.G., et al., “The effect of human mobility and control measures on the COVID-19 epidemic in China”. *Science*, 368(6490), (2020), 493.
- [12]. Tagliazucchi E., et al., “Lessons from being challenged by COVID-19”, *Chaos, Solitons & Fractals*, 137, (2020), 109923.
- [13]. Yousaf M., et al., “Statistical analysis of forecasting COVID-19 for upcoming month in Pakistan”, *Chaos, Solitons & Fractals*, 138, (2020), 109926.
- [14]. Salgotra R., Gandomi M., Gandomi A.H., “Time Series Analysis and Forecast of the COVID-19 Pandemic in India using Genetic Programming”. *Chaos, Solitons & Fractals*, 138, (2020), 109945.
- [15]. Ayinde K., et al., “Modeling Nigerian Covid-19 cases: A comparative analysis of models and estimators”, *Chaos, Solitons & Fractals*, 138, (2020), 109911.
- [16]. Mandal M., et al., “A model based study on the dynamics of COVID-19: Prediction and control”, *Chaos, Solitons & Fractals*, 136, (2020), 109889.
- [17]. Parbat D., Chakraborty M., “A python based support vector regression model for prediction of COVID19 cases in India”. *Chaos, Solitons & Fractals*, 138, (2020), 109942.
- [18]. Chimmula V.K.R. Zhang L., “Time series forecasting of COVID-19 transmission in Canada using LSTM networks”, *Chaos, Solitons & Fractals*, 135, (2020), 109864.
- [19]. Fanelli D., Piazza F., “Analysis and forecast of COVID-19 spreading in China, Italy and France”, *Chaos, Solitons & Fractals*, 134, (2020), 109761.
- [20]. EU Open Data Portal. COVID-19 Coronavirus data 2020 [cited 2020 5/29/2020]; Available from: <https://www.ecdc.europa.eu/sites/default/files/documents/COVID-19-geographic-disbtribution-worldwide.xlsx>.
- [21]. Şahin M., “Impact of weather on COVID-19 pandemic in Turkey”, *Science of The Total Environment*, 728, (2020), 138810.
- [22]. Williams C.K.I., Rasmussen C.E., “Gaussian processes for machine learning”, MIT press Cambridge, MA., 2, (2006).
- [23]. Thissen U., et al., “Using support vector machines for time series prediction”, *Chemometrics and Intelligent Laboratory Systems*, 69(1), (2003), 35-49.
- [24]. Moisen G.G., “Classification and Regression Trees, in *Encyclopedia of Ecology*, S.E. Jørgensen and B.D.

- Fath, Editors, Academic Press: Oxford, (2008), 582-588.
- [25]. Wu X., et al., "Top 10 algorithms in data mining", *Knowledge and Information Systems*, 14(1), (2008), 1-37.
- [26]. Arias Velásquez R.M. Mejía Lara J.V., "Forecast and evaluation of COVID-19 spreading in USA with reduced-space Gaussian process regression", *Chaos, Solitons & Fractals*, 136, (2020), 109924.
- [27]. Shahid F., Zameer A., Muneeb M., "Predictions for COVID-19 with deep learning models of LSTM, GRU and Bi-LSTM", *Chaos, Solitons & Fractals*, 140, (2020), 110212.
- [28]. Tomar A., Gupta N., "Prediction for the spread of COVID-19 in India and effectiveness of preventive measures", *Science of The Total Environment*, 728, (2020), 138762.
- [29]. Arora P., Kumar H., Panigrahi B.K., "Prediction and analysis of COVID-19 positive cases using deep learning models: A descriptive case study of India", *Chaos, Solitons & Fractals*, 139, (2020), 110017.
- [30]. Alzahrani S.I., Aljamaan I.A., Al-Fakih E.A., "Forecasting the spread of the COVID-19 pandemic in Saudi Arabia using ARIMA prediction model under current public health interventions", *Journal of Infection and Public Health*, 13(7), (2020), 914-919.
- [31]. Ribeiro M.H.D.M., et al., "Short-term forecasting COVID-19 cumulative confirmed cases: Perspectives for Brazil", *Chaos, Solitons & Fractals*, 135, (2020), 109853.
- [32]. Sujath R., Chatterjee J.M., Hassanien A.E., "A machine learning forecasting model for COVID-19 pandemic in India", *Stochastic Environmental Research and Risk Assessment*, (2020).
- [33]. Tuli S., et al., "Predicting the growth and trend of COVID-19 pandemic using machine learning and cloud computing", *Internet of Things*, 11, (2020), 100222.
- [34]. Wang P., et al., "Prediction of epidemic trends in COVID-19 with logistic model and machine learning technics", *Chaos, Solitons & Fractals*, 139, (2020), 110058.
- [35]. Liu J., et al., "Impact of meteorological factors on the COVID-19 transmission: A multi-city study in China", *Science of The Total Environment*, 726, (2020), 138513.
- [36]. Goswami K., Bharali S., Hazarika J., "Projections for COVID-19 pandemic in India and effect of temperature and humidity", *Diabetes & Metabolic Syndrome: Clinical Research & Reviews*, (2020).
- [37]. Li H., et al., "Air Pollution and temperature are associated with increased COVID-19 incidence: a time series study", *International Journal of Infectious Diseases*, (2020).
- [38]. Wu Y., et al., "Effects of temperature and humidity on the daily new cases and new deaths of COVID-19 in 166 countries", *Science of The Total Environment*, 729, (2020), 139051.
- [39]. Farzan A.N., U.S. coronavirus cases surpass 1.8 million as concern over potential spread rises with turmoil, in *The Washington Post*. 2020, *The Washington Post*.

A blockchain based lifelong learning platform: The Smart University

Bora Aslan,^{1,*} Kerem Ataşen¹

¹ Kırklareli University, Kırklareli, Turkey, bora.aslan@klu.edu.tr, atasenkerem@klu.edu.tr, ORCID: 0000-0002-8069-8204, ORCID: 0000-0002-9918-2830

ABSTRACT

According to today's education system, the content, applicability, quality and performance measurement criteria of the courses may vary according to countries, educational institutions and educators. Because of incorrect performance measurement, hidden skills disappear before they appear. Thanks to the graduation diploma it is observed that people with less professional knowledge and skills come to better places than those who are more knowledgeable and skilled. In addition, due to the lack of a proper training plan and long periods of education for the target learning community, boredom and financial problems may arise. In this study, a blockchain-based lifelong learning platform whose content, processing, reliability, decentralized, open to continuous and rapid accessibility, and evaluation criteria and method is completely objective is proposed while trying to avoid material and temporal problems. Thanks to this platform, the diplomas to be received by the students who have successfully passed the end-of-education exams will be time-stamped, immutable, safe and traceable. At the same time, all these documents, storage of training contents, diplomas, certificates, post-training exams and all related files, will be kept accessible, secure and immutable thanks to IPFS, the Inter Planetary File System. Achievements, employer and employee pools to be created according to the achievements, and recruitment contracts to be realized will be controlled by smart contracts and absolute reliability and objectivity will be ensured. All these concepts will be made available through a decentralized application (DApp) which will run on a private blockchain network that requires a partial permission to be established.

ARTICLE INFO

Research article

Received: 18.05.2020

Accepted: 15.12.2020

Keywords:

Blockchain,
smart contracts,
DApp,
solidity,
education,
IPFS

*Corresponding author

1. Introduction

Education is known as an important field of study that is open to development and change in the process from past to present in terms of its content and outputs. According to the classical education methods, the quality and duration of the education may vary as well as the people who teach at the same courses in schools with the same curriculum and the same subjects. The most important aspect of the educating process is the quality of the educating provided. This requires individuals to respond to the needs and demands of the society at the desired level with the knowledge, skills and experience acquired in line with the education they receive [1]. These changes, which can be observed in the quality of educational institutions, may also vary in the examinations conducted and the evaluation of these exams in order to determine how much the trainees have learned from education and how much they can apply. To summarize, there is no generally accepted infrastructure for educational institutions to carry out their training and to test the people who receive the training [2]. In addition, when

people want to study at a university after graduating from a university, they repeat the previous processes. Again, these people wait for the dates specified in the academic calendar to start their education and any other related processes. Because all of these procedures are distracting and time consuming, people are distracted from studying and documenting their competence in that field.

Due to the weakness of the education system and the lack of measuring capabilities, people may not be able to discover their real hidden areas of interest or qualify for training in institutions providing specific interests [3]. As a result of such situations, people would not have a diploma to document their skills and knowledge, they cannot rise in the institutions they work because of some legal regulations and cannot get the money they deserve in return for their labour. As a summary, it is seen that the person is more educated than the employed position required. [4].

In this study, a blockchain based lifelong learning platform was proposed as a solution to these shortcomings. With a university to be implemented on this platform, the professional knowledge competence of the people who receive equal training in terms of content, method and quality will be determined by smart contracts on this blockchain based platform. In this way, subjective professional knowledge measurement and assessment will be replaced by an objective assessment, while unjust progression, rise and income based on evaluation will be eliminated. Since the data recorded in the blockchain is time stamped, the education contents and diplomas can be tracked backwards and transparently. Thanks to its blockchain tamper proof feature, any positive or negative interventions to educational contents or diplomas will be prevented strictly.

2. Method

At the present time, the data about the trainings and final exams given by universities or recognized educational institutions around the world are stored centrally. Central storage of data undermines confidence in data privacy, security, and non-changeability. The request for instant access to data may be delayed at high request moments and cause the data to be completely inaccessible for a certain period of time due to a possible technical failure [5]. In this study, blockchain technology, decentralized applications running on blockchain (DApp) that associated with smart contracts and Inter Planetary File System (IPFS) as a storage environment are proposed as solutions for such situations [5].

a. Blockchain

Blockchain is a distributed ledger technology in which the transactions that are required to be kept in record are encrypted and stored in structures called blocks. In this distributed ledger, the blocks are linked chronologically to form a chain of blocks. The first block in the chain is called the Genesis block. Each block after the Genesis block contains the encrypted information of the preceding block. In this way, all blocks in the blockchain can be accessed retrospectively [6]. Blockchain is not a database. Because in blockchain logic, there is no way to edit or delete any data you added before. In addition, all transactions with blockchain records contain timestamps. This is a crucial feature for reliability and confirmability.

b. Smart Contracts and DApp

According to Szabo, smart contracts are digital contracts, which are the digitalized version of classical contracts that operate when the necessary conditions are met [7]. In the context of blockchain, smart contracts are scripts stored on the blockchain. It is not possible to run smart contracts on every blockchain platform, as well as blockchain platforms such as Ethereum, Hyperledger Fabric, NEM, Stellar, iOLite, Neblio, and Lisk. To upload a smart contract to the blockchain, Ethereum runs a special creation transaction that identifies the

contract to the blockchain. At the end of this process, a contract account is created and a unique 160-bits address is assigned to this account. After these processes have been completed, the code of the contract is deployed to blockchain. From this moment it is not possible to intervene in the smart contract [8]. If a change in the contract is desired, only the modified version of the contract can be uploaded to the blockchain, which means creating a new 160-bits contract account with a unique address. Different contract or wallet accounts can then interact with them by sending contract-calling transactions to known contract addresses.

Unlike today's centralized web or mobile applications (Web 2.0 - CAPP), DApps are transparent, distributed, flexible, decentralized applications that do not run on a central server or machine with better incentive structure [9]. The data used by such applications is also kept in a blockchain in a decentralized manner like the application itself. In this way, in case of failure of a web server seen in conventional systems, the period of inaccessibility of the application will be overcome. Since the applications will run in a decentralized blockchain network, any disappearance of machines will not cause the application and related data to be inaccessible. Examples of the decentralized counterparts of today's popular central practices are given in Table 1.

Table 1. Centralized Applications and Decentralized Counterparts

	CAPP	DAPP
Browsers	Chrome, Firefox	Brave
Storage Services	Dropbox, Yandex Disk	Storj, IPFS
Video and Audio Calling	Skype, Google Voice	Experty
Social Network	Facebook, Twitter	Steemit, Akasha
Messaging	Whatsapp, BIP	Status
Operating Systems	Android, IOS	EOS, Essentia.One, Nynja
Home Office Platforms	Up, Bionluk	Ethlance

c. IPFS

IPFS is an end-to-end (P2P) hyper-media protocol that is being developed to make the web more transparent, faster, and more reliable, with the ultimate goal of replacing HTTP [10]. According to the Hyper-Text Transfer Protocol (HTTP) used in today's web, a file that is desired to be downloaded is downloaded from only one computer. However, this file can be downloaded in pieces from multiple computers at the same time. IPFS makes it possible to distribute large volumes of data with high efficiency.

Using IPFS and blockchain together, data can be stored in IPFS according to the blockchain philosophy. In a transaction that will be registered to blockchain about this data, only permanent non-modifiable cryptographic IPFS links can be stored to represent the data. [11]. Since each file in the IPFS system and each block that forms this file consists of a cryptographic hash value, and the blockchain is timestamped, the data will not need to be kept in a chain.

d. Operating of the System

The system consists of the member educating institutions that will form a special blockchain network that requires partial permission, a DApp that will run on the blockchain network of these training institutions and interacts with smart contracts, and the IPFS components where all the data such as diplomas, participant information will be kept, as well as training, exam contents. This blockchain network is a special blockchain network that requires partial permission, since the institutions to be included in the system will be selected and identified, but no member participating in the network will need to obtain permission for block writing and transaction validation [12].

In Turkey, it is planned to use Blockchain Research Network (BAG) blockchain, being established in TÜBİTAK BİLGEM coordination, for the running of this Smart University platform. That blockchain is under construction. The Smart University DApp Application will be developed to run on this semi private blockchain network. Through this application, the world-wide accepted educational contents of the student will be stored on IPFS. The results of the exams to be determined by smart contracts and the diplomas to be obtained upon graduation will also be kept on this IPFS. By shifting the data load to IPFS and using only cryptographic IPFS links in the blockchain, the scalability problem of the blockchain will be overcome.

According to the lessons received by the learner and exam results, the potential employee pool for employers and the potential employer pool for students will be realized through smart contracts. In the event of a possible recruitment process, the contract to be signed by the parties will again be a smart contract, preventing unfairness and data monopolization which may make employer institutions advantageous in case of a dispute. In addition to all these opportunities, if this system is accepted globally, it will not be necessary to study for years to obtain a diploma and the student who has reached sufficient maturity and knowledge will be able to get started without unnecessary waiting. The operating of the blockchain-based lifelong learning platform is schematically illustrated in Figure 1.

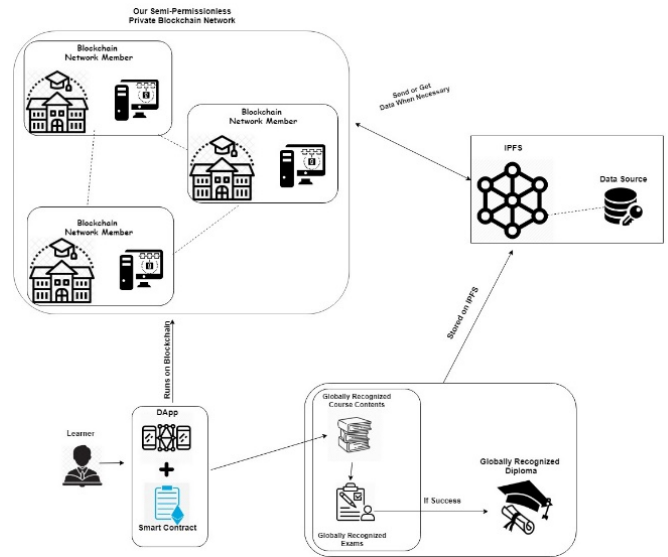


Figure 1. The Smart University Operation Flow

3. Discussion and conclusion

Blockchain technology and other related technologies that have started to develop with this technology have not been fully accepted in our country yet and will take time to be accepted. In addition, the IPFS structure is not yet stable and will take time to become stable. The Blockchain Research Network blockchain is under development by TÜBİTAK BİLGEM and it will take some time to finish the development and make it stable. A standard for the creation of globally recognized educational contents, end-of-education examinations, and selected institutions that will produce content and exam questions according to this standard should be identified. These institutions should have incentive awards in return for their efforts. In this system, a system-specific crypto currency can be generated and used to purchase training. It is possible for all educational institutions that recognize this system to accept and apply for the undergraduate diploma of the students who will apply for postgraduate education, and for employers to be able to recognize and receive this diploma. The tamper-proof and time-stamped properties of the blockchain will eliminate the possibility that the diplomas are false or fake. Since the achievements in the courses will be taken into consideration while creating the target employer, employee and workplace pool, it is aimed to improve the labour-performance harmony between employer and employee according to today's conditions.

The positive or negative aspects of conducting the trainings in the classroom or online have been observed through some researches [13]. The fact that the exams are held online allows the exam questions to be easily copied and stored to make higher grades in next exams. As a result of this situation, it may be necessary to create different exam questions for each

student who takes the same course at the same or different times and will take the exam at the same or different time. This problem can be solved in a way that the lessons can be taken at various times but the exams can only be held at certain times. There are courses that are appropriate for online training and performance measurement, as well as courses that are inappropriate, requiring laboratory practice and group work. Students who are interested in these courses and want to work in related fields may not be able to get full efficiency from this platform.

4. Future works

The ultimate goal of the Smart University platform, which is planned to be tested among the selected pilot training institutions (BAG members) and employers, is to become acceptable to all educational institutions and employers in the country. After achieving country-wide acceptance, smart university platforms can be linked to other countries. Block chain networks running on these platforms can communicate with each other to ensure a worldwide data integrity. Ensuring the integrity of this data means that there are people with recognized diplomas worldwide. In this way, people's knowledge can easily be accepted by other countries which recognize this platform as a global quality.

References

- [1]. Sallis E., Total quality management in education. Routledge, 2014.
- [2]. Shriberg M., "Institutional assessment tools for sustainability in higher education: strengths, weaknesses, and implications for practice and theory," Higher education policy, 15, 2, (2002), 153-167.
- [3]. Boyd R. D., Myers J.G., "Transformative education," International journal of lifelong education, 7, 4, (1988), 261-284.
- [4]. Dolton P., Vignoles A., "The incidence and effects of overeducation in the UK graduate labour market," Economics of education review, 19, 2, (2000), 179-198.
- [5]. Ren K., Thomson A., Abadi D.J., "An evaluation of the advantages and disadvantages of deterministic database systems," Proceedings of the VLDB Endowment, 7, 10, (2014), 821-832.
- [6]. Crosby M., Pattanayak P., Verma S., Kalyanaraman V., "Blockchain technology: Beyond bitcoin," Applied Innovation, 2, 6-10, (2016), 71.
- [7]. Szabo N., "Formalizing and securing relationships on public networks," First Monday, 2, 9, (1997).
- [8]. Wood G., "Ethereum: A secure decentralised generalised transaction ledger," Ethereum project yellow paper, 151, (2014), 1-32.
- [9]. Raval S., "Decentralized applications: harnessing Bitcoin's blockchain technology." O'Reilly Media, Inc., (2016).
- [10]. Benet J., "IPFS-content addressed, versioned," P2P file system. CoRR, abs/1407.3561, (2014).
- [11]. Chen Y., Li H., Li K., Zhang J., "An improved P2P file system scheme based on IPFS and Blockchain," in 2017 IEEE International Conference on Big Data (Big Data), (2017), 2652-2657: IEEE.
- [12]. Usta A., Doğantekin S., "Blockchain 101," Kapital Medya Hizmetleri A. fi, (2017).
- [13]. Kirtman L., "Online versus in-class courses: An examination of differences in learning outcomes," Issues in Teacher Education, 18, 2, (2009), 103-116.

On the recursive sequence $x_{n+1} = \frac{x_{n-14}}{1 + x_{n-2}x_{n-5}x_{n-8}x_{n-11}}$

Burak Oğul, ^{1,*} Dağıstan Şimşek ²

¹ Department of Mathematics, Faculty of Science, Kyrgyz Turkish Manas University, Bishkek, Kyrgyzstan, burak_1745@hotmail.com, ORCID: 0000-0002-3264-4340

² Department of Industrial Engineering, Faculty of Engineering and Natural Sciences Konya Technical University, Konya, Turkey, dsimsek@ktun.edu.tr

ABSTRACT

In this paper, given solutions for the following difference equation

$$x_{n+1} = \frac{x_{n-14}}{1 + x_{n-2}x_{n-5}x_{n-8}x_{n-11}}, \quad n \in \mathbb{N}$$

where the initial conditions are positive real numbers. The initial conditions of the equation are arbitrary positive real numbers. We investigate periodic behavior of this equation. Also some numerical examples and graphs of solutions are given.

ARTICLE INFO

Research article

Received: 05.06.2020

Accepted: 18.11.2020

Keywords:

Difference equation
recursive sequence.

*Corresponding author

1. Introduction

The study and solution of nonlinear rational difference equation of high order is quite challenging and rewarding. Lately there's a lot of interest in studying the global attractivity, boundedness character, periodicity and the solution form of nonlinear difference equations. For some works in this field, for example: [1-45].

Elabbasy et al. [10-11] investigated the global stability, periodicity character and gave the solution of some special cases of the following difference equations

$$x_{n+1} = ax_n - \frac{bx_n}{cx_n - dx_{n-1}}, \quad x_{n+1} = \frac{\alpha x_{n-k}}{\beta + \gamma \prod_{i=0}^k x_{n-i}}.$$

In [15] Elsayed dealt with the dynamics and found the solution of the following rational recursive sequences

$$x_{n+1} = \frac{x_{n-5}}{\pm 1 \pm x_{n-1}x_{n-3}x_{n-5}}.$$

Simsek et. al. [31,32,33,34], studied the following problems with positive initial values

$$x_{n+1} = \frac{x_{n-3}}{1 + x_{n-1}}, \quad x_{n+1} = \frac{x_{n-5}}{1 + x_{n-2}}, \quad x_{n+1} = \frac{x_{n-5}}{1 + x_{n-1}x_{n-3}}, \quad x_{n+1} = \frac{x_{n-3}}{1 + x_n x_{n-1} x_{n-2}}$$

respectively.

In this work the following non linear difference equation was studied

$$x_{n+1} = \frac{x_{n-14}}{1 + x_{n-2}x_{n-5}x_{n-8}x_{n-11}} \tag{1}$$

where $x_{-14}, x_{-13}, \dots, x_{-1}, x_0 \in (0, \infty)$ is investigated.

2. Main results

Let \bar{x} be the unique positive equilibrium of the equation (1), then clearly

$$\bar{x} = \frac{\bar{x}}{1 + \bar{x}\bar{x}\bar{x}\bar{x}} \Rightarrow \bar{x} + \bar{x}^5 = \bar{x} \Rightarrow \bar{x}^5 = 0 \Rightarrow \bar{x} = 0$$

so, $\bar{x} = 0$ can be obtained.

For any $k \geq 0$ and $m > k$ notation $i = \overline{k, m}$ means $i = k, k + 1, \dots, m$.

Theorem 1: Consider the difference equation (1). Then the following statements are true.

a) The sequences

$$(x_{15n-14}), (x_{15n-13}), \dots, (x_{15n-1}), (x_{15n})$$

are being decreasing and

$$a_1, a_2, \dots, a_{14}, a_{15} \geq 0$$

are existed and such that

$$\lim_{n \rightarrow \infty} x_{15n-14+k} = a_{1+k} \text{ for } k = \overline{0, 14}.$$

b) $(a_1, a_2, a_3, a_4, a_5, a_6, a_7, a_8, a_9, a_{10}, a_{11}, a_{12}, a_{13}, a_{14}, a_{15}, a_1, a_2, a_3, a_4, a_5, a_6, a_7, a_8, a_9, a_{10}, a_{11}, a_{12}, a_{13}, a_{14}, a_{15}, \dots)$ is a solution of (1) having period 15.

c) $\prod_{k=0}^4 \lim_{n \rightarrow \infty} x_{15n-3k-2} = 0, \prod_{k=0}^4 \lim_{n \rightarrow \infty} x_{15n-3k-1} = 0, \prod_{k=0}^4 \lim_{n \rightarrow \infty} x_{15n-3k} = 0,$ or $\prod_{k=0}^4 a_{3k+2} = 0, \prod_{k=0}^4 a_{3k+1} = 0, \prod_{k=1}^5 a_{3k} = 0.$

d) If there exist $n_0 \in \mathbb{N}$ such that $x_{n+1} \leq x_{n-11}$ for all $n \geq n_0$, then

$$\lim_{n \rightarrow \infty} x_n = 0.$$

e) The following formulas can be generated:

$$x_{15n+1+k} = x_{-14+k} \left(1 - \frac{x_{-2+k}x_{-5+k}x_{-8+k}x_{-11+k}}{1 + x_{-2+k}x_{-5+k}x_{-8+k}x_{-11+k}} \sum_{j=0}^n \prod_{i=1}^{5j} \frac{1}{1 + x_{3i-2+k}x_{3i-5+k}x_{3i-8+k}x_{3i-11+k}} \right), k = \overline{0, 2}$$

$$x_{15n+4+k} = x_{-11+k} \left(1 - \frac{x_{-2+k}x_{-5+k}x_{-8+k}x_{-14+k}}{1 + x_{-2+k}x_{-5+k}x_{-8+k}x_{-11+k}} \sum_{j=0}^n \prod_{i=1}^{5j+1} \frac{1}{1 + x_{3i-2+k}x_{3i-5+k}x_{3i-8+k}x_{3i-11+k}} \right), k = \overline{0, 2}$$

$$x_{15n+7+k} = x_{-8+k} \left(1 - \frac{x_{-2+k}x_{-5+k}x_{-11+k}x_{-14+k}}{1 + x_{-2+k}x_{-5+k}x_{-8+k}x_{-11+k}} \sum_{j=0}^n \prod_{i=1}^{5j+2} \frac{1}{1 + x_{3i-2+k}x_{3i-5+k}x_{3i-8+k}x_{3i-11+k}} \right), k = \overline{0, 2}$$

$$x_{15n+10+k} = x_{-5+k} \left(1 - \frac{x_{-2+k}x_{-8+k}x_{-11+k}x_{-14+k}}{1 + x_{-2+k}x_{-5+k}x_{-8+k}x_{-11+k}} \sum_{j=0}^n \prod_{i=1}^{5j+3} \frac{1}{1 + x_{3i-2+k}x_{3i-5+k}x_{3i-8+k}x_{3i-11+k}} \right), k = \overline{0, 2}$$

$$x_{15n+13+k} = x_{-2+k} \left(1 - \frac{x_{-5+k} x_{-8+k} x_{-11+k} x_{-14+k}}{1 + x_{-2+k} x_{-5+k} x_{-8+k} x_{-11+k}} \sum_{j=0}^n \prod_{i=1}^{5j+4} \frac{1}{1 + x_{3i-2+k} x_{3i-5+k} x_{3i-8+k} x_{3i-11+k}} \right), k = \overline{0, 2}.$$

f) If $x_{15n+1+k} \rightarrow a_{1+k} \neq 0$, $x_{15n+4+k} \rightarrow a_{4+k} \neq 0$, $x_{15n+7+k} \rightarrow a_{7+k} \neq 0$, $x_{15n+10+k} \rightarrow a_{10+k} \neq 0$, then $x_{15n+13+k} \rightarrow a_{13+k} = 0$ as $n \rightarrow \infty$. $k = \overline{0, 2}$.

Proof

a) Firstly, from the (1)

$$x_{n+1} (1 + x_{n-2} x_{n-5} x_{n-8} x_{n-11}) = x_{n-14}$$

is obtained. If $x_{n-2} x_{n-5} x_{n-8} x_{n-11} \in (0, \infty)$, then $1 + x_{n-2} x_{n-5} x_{n-8} x_{n-11} \in (1, \infty)$. Since

$$x_{n+1} < x_{n-14},$$

$n \in \mathbb{N}$,

$$\lim_{n \rightarrow \infty} x_{15n-14+k} = a_{1+k}, \text{ for } k = \overline{0, 14}$$

existed formulas are obtained.

b) $(a_1, a_2, a_3, a_4, a_5, a_6, a_7, a_8, a_9, a_{10}, a_{11}, a_{12}, a_{13}, a_{14}, a_{15}, a_1, a_2, a_3, a_4, a_5, a_6, a_7, a_8, a_9, a_{10}, a_{11}, a_{12}, a_{13}, a_{14}, a_{15}, \dots)$ is a solution of (1) having period 15.

c) In view the (1),

$$n = 15n \Rightarrow x_{15n+1} = \frac{x_{15n-14}}{1 + x_{15n-2} x_{15n-5} x_{15n-8} x_{15n-11}}$$

is obtained. If the limits are put on both sides of the above equality,

$$\lim_{n \rightarrow \infty} x_{15n+1} = \lim_{n \rightarrow \infty} \frac{x_{15n-14}}{1 + x_{15n-2} x_{15n-5} x_{15n-8} x_{15n-11}},$$

is obtained. Then

$$\prod_{k=0}^4 \lim_{n \rightarrow \infty} x_{15n-3k-2} = 0, k = \overline{0, 2}.$$

d) If there exist $n_0 \in \mathbb{N}$ such that $x_{n+1} \leq x_{n-11}$ for all $n \geq n_0$, then, $a_1 \leq a_4 \leq a_7 \leq a_{10} \leq a_{13} \leq a_1, a_2 \leq a_5 \leq a_8 \leq a_{11} \leq a_{14} \leq a_2, a_3 \leq a_6 \leq a_9 \leq a_{12} \leq a_{15} \leq a_3$.

e)

Subtracting x_{n-14} from the left and right-hand sides (1) we obtain:

$$x_{n+1} - x_{n-14} = \frac{1}{1 + x_{n-2} x_{n-5} x_{n-8} x_{n-11}} (x_{n-2} - x_{n-17}). \tag{2}$$

From (2), for $n \geq 3$ following formula is produced.

$$\begin{aligned}
 x_{3n-8} - x_{3n-23} &= (x_1 - x_{-14}) \prod_{i=1}^{n-3} \frac{1}{1 + x_{3i-2}x_{3i-5}x_{3i-8}x_{3i-11}} \\
 x_{3n-7} - x_{3n-22} &= (x_2 - x_{-13}) \prod_{i=1}^{n-3} \frac{1}{1 + x_{3i-2}x_{3i-5}x_{3i-8}x_{3i-11}} \\
 x_{3n-6} - x_{3n-21} &= (x_3 - x_{-12}) \prod_{i=1}^{n-3} \frac{1}{1 + x_{3i-2}x_{3i-5}x_{3i-8}x_{3i-11}}
 \end{aligned} \tag{3}$$

Replacing n by $5j$ in (3) and summing from $j=0$ to $j=n$, we obtain:

$$x_{15n+1+k} - x_{-14+k} = (x_{1+k} - x_{-14+k}) \sum_{j=0}^n \prod_{i=1}^{5j} \frac{1}{1 + x_{3i-2+k}x_{3i-5+k}x_{3i-8+k}x_{3i-11+k}}, k = \overline{0,2}$$

Also, $5j+1$ inserted in (3) by replacing n , $j=0$ to $j=n$ is obtained by summing

$$x_{15n+4+k} - x_{-11+k} = (x_{4+k} - x_{-11+k}) \sum_{j=0}^n \prod_{i=1}^{5j+1} \frac{1}{1 + x_{3i-2+k}x_{3i-5+k}x_{3i-8+k}x_{3i-11+k}}, k = \overline{0,2}$$

Also, $5j+2$ inserted in (3) by replacing n , $j=0$ to $j=n$ is obtained by summing

$$x_{15n+7+k} - x_{-8+k} = (x_{7+k} - x_{-8+k}) \sum_{j=0}^n \prod_{i=1}^{5j+2} \frac{1}{1 + x_{3i-2+k}x_{3i-5+k}x_{3i-8+k}x_{3i-11+k}}, k = \overline{0,2}$$

Also, $5j+3$ inserted in (3) by replacing n , $j=0$ to $j=n$ is obtained by summing

$$x_{15n+10+k} - x_{-5+k} = (x_{10+k} - x_{-5+k}) \sum_{j=0}^n \prod_{i=1}^{5j+3} \frac{1}{1 + x_{3i-2+k}x_{3i-5+k}x_{3i-8+k}x_{3i-11+k}}, k = \overline{0,2}$$

Also, $5j+4$ inserted in (3) by replacing n , $j=0$ to $j=n$ is obtained by summing

$$x_{15n+13+k} - x_{-2+k} = (x_{13+k} - x_{-2+k}) \sum_{j=0}^n \prod_{i=1}^{5j+4} \frac{1}{1 + x_{3i-2+k}x_{3i-5+k}x_{3i-8+k}x_{3i-11+k}}, k = \overline{0,2}$$

Now we obtained of the above formulas:

$$\begin{aligned}
 x_{15n+1+k} &= x_{-14+k} \left(1 - \frac{x_{-2+k}x_{-5+k}x_{-8+k}x_{-11+k}}{1 + x_{-2+k}x_{-5+k}x_{-8+k}x_{-11+k}} \sum_{j=0}^n \prod_{i=1}^{5j} \frac{1}{1 + x_{3i-2+k}x_{3i-5+k}x_{3i-8+k}x_{3i-11+k}} \right), k = \overline{0,2} \\
 x_{15n+4+k} &= x_{-11+k} \left(1 - \frac{x_{-2+k}x_{-5+k}x_{-8+k}x_{-14+k}}{1 + x_{-2+k}x_{-5+k}x_{-8+k}x_{-11+k}} \sum_{j=0}^n \prod_{i=1}^{5j+1} \frac{1}{1 + x_{3i-2+k}x_{3i-5+k}x_{3i-8+k}x_{3i-11+k}} \right), k = \overline{0,2} \\
 x_{15n+7+k} &= x_{-8+k} \left(1 - \frac{x_{-2+k}x_{-5+k}x_{-11+k}x_{-14+k}}{1 + x_{-2+k}x_{-5+k}x_{-8+k}x_{-11+k}} \sum_{j=0}^n \prod_{i=1}^{5j+2} \frac{1}{1 + x_{3i-2+k}x_{3i-5+k}x_{3i-8+k}x_{3i-11+k}} \right), k = \overline{0,2} \\
 x_{15n+10+k} &= x_{-5+k} \left(1 - \frac{x_{-2+k}x_{-8+k}x_{-11+k}x_{-14+k}}{1 + x_{-2+k}x_{-5+k}x_{-8+k}x_{-11+k}} \sum_{j=0}^n \prod_{i=1}^{5j+3} \frac{1}{1 + x_{3i-2+k}x_{3i-5+k}x_{3i-8+k}x_{3i-11+k}} \right), k = \overline{0,2} \\
 x_{15n+13+k} &= x_{-2+k} \left(1 - \frac{x_{-5+k}x_{-8+k}x_{-11+k}x_{-14+k}}{1 + x_{-2+k}x_{-5+k}x_{-8+k}x_{-11+k}} \sum_{j=0}^n \prod_{i=1}^{5j+4} \frac{1}{1 + x_{3i-2+k}x_{3i-5+k}x_{3i-8+k}x_{3i-11+k}} \right), k = \overline{0,2} .
 \end{aligned}$$

f) Suppose that $a_{1+k} = a_{4+k} = a_{7+k} = a_{10+k} = a_{13+k} = 0$ for $k = \overline{0, 2}$. By e) the following formulas are produced below

$$\begin{aligned} \lim_{n \rightarrow \infty} x_{15n+1+k} &= \lim_{n \rightarrow \infty} x_{-14+k} \left(1 - \frac{x_{-2+k} x_{-5+k} x_{-8+k} x_{-11+k}}{1 + x_{-2+k} x_{-5+k} x_{-8+k} x_{-11+k}} \sum_{j=0}^n \prod_{i=1}^{5j} \frac{1}{1 + x_{3i-2+k} x_{3i-5+k} x_{3i-8+k} x_{3i-11+k}} \right) \\ a_{1+k} &= x_{-14+k} \left(1 - \frac{x_{-2+k} x_{-5+k} x_{-8+k} x_{-11+k}}{1 + x_{-2+k} x_{-5+k} x_{-8+k} x_{-11+k}} \sum_{j=0}^{\infty} \prod_{i=1}^{5j} \frac{1}{1 + x_{3i-2+k} x_{3i-5+k} x_{3i-8+k} x_{3i-11+k}} \right) \\ a_{1+k} = 0 &\Rightarrow \frac{1 + x_{-2+k} x_{-5+k} x_{-8+k} x_{-11+k}}{x_{-2+k} x_{-5+k} x_{-8+k} x_{-11+k}} = \sum_{j=0}^{\infty} \prod_{i=1}^{5j} \frac{1}{1 + x_{3i-2+k} x_{3i-5+k} x_{3i-8+k} x_{3i-11+k}} \end{aligned} \tag{4}$$

Similarly;

$$a_{4+k} = 0 \Rightarrow \frac{1 + x_{-2+k} x_{-5+k} x_{-8+k} x_{-11+k}}{x_{-2+k} x_{-5+k} x_{-8+k} x_{-14+k}} = \sum_{j=0}^{\infty} \prod_{i=1}^{5j+1} \frac{1}{1 + x_{3i-2+k} x_{3i-5+k} x_{3i-8+k} x_{3i-11+k}} \tag{5}$$

Similarly;

$$a_{7+k} = 0 \Rightarrow \frac{1 + x_{-2+k} x_{-5+k} x_{-8+k} x_{-11+k}}{x_{-2+k} x_{-5+k} x_{-11+k} x_{-14+k}} = \sum_{j=0}^{\infty} \prod_{i=1}^{5j+2} \frac{1}{1 + x_{3i-2+k} x_{3i-5+k} x_{3i-8+k} x_{3i-11+k}} \tag{6}$$

Similarly;

$$a_{10+k} = 0 \Rightarrow \frac{1 + x_{-2+k} x_{-5+k} x_{-8+k} x_{-11+k}}{x_{-2+k} x_{-8+k} x_{-11+k} x_{-14+k}} = \sum_{j=0}^{\infty} \prod_{i=1}^{5j+3} \frac{1}{1 + x_{3i-2+k} x_{3i-5+k} x_{3i-8+k} x_{3i-11+k}} \tag{7}$$

Similarly;

$$a_{13+k} = 0 \Rightarrow \frac{1 + x_{-2+k} x_{-5+k} x_{-8+k} x_{-11+k}}{x_{-5+k} x_{-8+k} x_{-11+k} x_{-14+k}} = \sum_{j=0}^{\infty} \prod_{i=1}^{5j+4} \frac{1}{1 + x_{3i-2+k} x_{3i-5+k} x_{3i-8+k} x_{3i-11+k}} \tag{8}$$

From (4) and (5),

$$\begin{aligned} \frac{1 + x_{-2+k} x_{-5+k} x_{-8+k} x_{-11+k}}{x_{-2+k} x_{-5+k} x_{-8+k} x_{-11+k}} &= \sum_{j=0}^{\infty} \prod_{i=1}^{5j} \frac{1}{1 + x_{3i-2+k} x_{3i-5+k} x_{3i-8+k} x_{3i-11+k}} > \\ \frac{1 + x_{-2+k} x_{-5+k} x_{-8+k} x_{-11+k}}{x_{-2+k} x_{-5+k} x_{-8+k} x_{-14+k}} &= \sum_{j=0}^{\infty} \prod_{i=1}^{5j+1} \frac{1}{1 + x_{3i-2+k} x_{3i-5+k} x_{3i-8+k} x_{3i-11+k}} \end{aligned} \tag{9}$$

thus, $x_{-14+k} > x_{-11+k}$. From the (5) and (6),

$$\begin{aligned} \frac{1 + x_{-2+k} x_{-5+k} x_{-8+k} x_{-11+k}}{x_{-2+k} x_{-5+k} x_{-8+k} x_{-14+k}} &= \sum_{j=0}^{\infty} \prod_{i=1}^{5j+1} \frac{1}{1 + x_{3i-2+k} x_{3i-5+k} x_{3i-8+k} x_{3i-11+k}} > \\ \frac{1 + x_{-2+k} x_{-5+k} x_{-8+k} x_{-11+k}}{x_{-2+k} x_{-5+k} x_{-11+k} x_{-14+k}} &= \sum_{j=0}^{\infty} \prod_{i=1}^{5j+2} \frac{1}{1 + x_{3i-2+k} x_{3i-5+k} x_{3i-8+k} x_{3i-11+k}} \end{aligned} \tag{10}$$

thus, $x_{-11+k} > x_{-8+k}$. From the (6) and (7),

$$\begin{aligned} \frac{1 + x_{-2+k} x_{-5+k} x_{-8+k} x_{-11+k}}{x_{-2+k} x_{-5+k} x_{-11+k} x_{-14+k}} &= \sum_{j=0}^{\infty} \prod_{i=1}^{5j+2} \frac{1}{1 + x_{3i-2+k} x_{3i-5+k} x_{3i-8+k} x_{3i-11+k}} > \\ \frac{1 + x_{-2+k} x_{-5+k} x_{-8+k} x_{-11+k}}{x_{-2+k} x_{-8+k} x_{-11+k} x_{-14+k}} &= \sum_{j=0}^{\infty} \prod_{i=1}^{5j+3} \frac{1}{1 + x_{3i-2+k} x_{3i-5+k} x_{3i-8+k} x_{3i-11+k}} \end{aligned} \tag{11}$$

thus, $x_{-8+k} > x_{-5+k}$. From the (7) and (8),

$$\frac{1 + x_{-2+k} x_{-5+k} x_{-8+k} x_{-11+k}}{x_{-2+k} x_{-8+k} x_{-11+k} x_{-14+k}} = \sum_{j=0}^{\infty} \prod_{i=1}^{5j+3} \frac{1}{1 + x_{3i-2+k} x_{3i-5+k} x_{3i-8+k} x_{3i-11+k}} >$$

$$\frac{1 + x_{-2+k} x_{-5+k} x_{-8+k} x_{-11+k}}{x_{-5+k} x_{-8+k} x_{-11+k} x_{-14+k}} = \sum_{j=0}^{\infty} \prod_{i=1}^{5j+4} \frac{1}{1 + x_{3i-2+k} x_{3i-5+k} x_{3i-8+k} x_{3i-11+k}} \tag{12}$$

thus, $x_{-5+k} > x_{-2+k}$.

From here we obtain $x_{-14+k} > x_{-11+k} > x_{-8+k} > x_{-5+k} > x_{-2+k}$. We arrive at a contradiction which completes the proof of theorem.

3. Example

Example 3.1: If the initial conditions are selected in accordance with Lemma 1 and Theorem 1;

$x[-14] = 0.9999999999999999$; $x[-13] = 0.9999999999999999$; $x[-12] = 0.9999999999999999$; $x[-11] = 9.999999999999999$;
 $x[-10] = 9.999999999999999$; $x[-9] = 9.999999999999999$; $x[-8] = 8.999999999999999$; $x[-7] = 7.999999999999999$; $x[-6] = 6.999999999999999$,
 $x[-5] = 5.999999999999999$; $x[-4] = 4.999999999999999$; $x[-3] = 3.999999999999999$; $x[-2] = 2.999999999999999$; $x[-1] = 1.999999999999999$; $x[0] = 0.9$;

$$x_n = \left\{ \begin{array}{l} 0.50025, 0.502515, 0.526341, 0.666778, 0.667786, 0.678583, 0.750063, 0.75063, 0.756763, 0.800039, \\ 0.800394, 0.804256, 0.832389, 0.823893, 0.739291, 0.375266, 0.377674, 0.403224, 0.561523, 0.562608, \\ 0.574373, 0.65776, 0.658379, 0.665167, 0.717284, 0.717676, 0.722025, 0.757118, 0.748722, 0.665291, \\ 0.31257, 0.314982, 0.340698, 0.505124, 0.506201, 0.517986, 0.605816, 0.606423, 0.613186, 0.668847, \\ 0.669228, 0.673535, 0.711593, 0.703219, 0.620095, 0.272833, 0.275222, 0.300796, 0.468286, 0.469337, \\ 0.480937, 0.571088, 0.571671, 0.578248, 0.635834, 0.636192, 0.64032, 0.680044, 0.671665, 0.588569, \\ 0.244554, 0.246913, 0.27226, 0.441617, 0.442639, 0.454, 0.545609, 0.546164, 0.55251, 0.611337, \\ 0.611668, 0.615577, 0.656398, 0.648005, 0.564824, 0.222993, 0.225322, 0.25042, 0.421059, 0.422052, \\ 0.433162, 0.525799, 0.526325, 0.53243, 0.592148, 0.592452, 0.59613, 0.637754, 0.629342, 0.546025, \\ 0.205788, 0.208088, 0.232934, 0.404529, 0.405493, 0.416354, 0.509772, 0.510272, 0.516136, 0.576544, \dots \end{array} \right.$$

solutions are obtained and the graphs of the solutions are shown below.

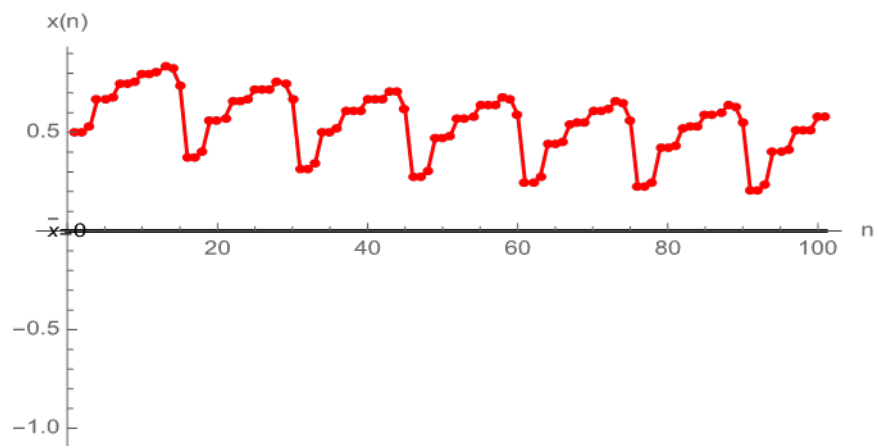


Figure 3.1 x_n solutions graph

References

- [1]. Amleh A. M., Grove E. A., Ladas G., Georgiou D. A., On the recursive sequence $x_{n+1} = \alpha + \frac{x_{n-1}}{x_n}$, J. Math. Anal. Appl., 233, 2, (1999), 790-798.
- [2]. Ari, M., Gelişken, A., Periodic and asymptotic behavior of a difference equation. Asian-European Journal of Mathematics, 12, 6, (2019), 2040004.
- [3]. Belhannache, F., Nouressadat T., and Raafat A., Dynamics of a third-order rational difference equation, Bull. Math. Soc. Sci. Math. Roumanie, 59, 1, (2016).
- [4]. Cinar C., On the positive solutions of the difference equation $x_{n+1} = \frac{x_{n-1}}{1 + ax_n x_{n-1}}$, Appl. Math. Comp., 158, 3, (2004), 809–812.
- [5]. Cinar C., On the positive solutions of the difference equation $x_{n+1} = \frac{x_{n-1}}{-1 + ax_n x_{n-1}}$, Appl. Math. Comp., 158, 3, (2004), 793–797.
- [6]. Cinar C., On the positive solutions of the difference equation $x_{n+1} = \frac{ax_{n-1}}{1 + bx_n x_{n-1}}$, Appl. Math. Comp., 156, 3, (2004), 587–590.
- [7]. Cinar, G., Gelişken, A., Özkan, O., Well-defined solutions of the difference equation $x_n = x_{n-3} - 4x_{n-4} - 5x_{n-5} - kx_{n-2} + 1 \pm x_{n-3} - 4x_{n-4} - 5x_{n-5} - k$. Asian-European Journal of Mathematics, 12, 6, (2019), 2040016.
- [8]. DeVault R., Ladas G., Schultz W.S., On the recursive sequence $x_{n+1} = \frac{A}{x_n} + \frac{1}{x_{n-2}}$, Proc. Amer. Math. Soc., 126, 11, (1998), 3257-3261.
- [9]. Elabbasy E. M., El-Metwally H., Elsayed E. M., On the difference equation $x_{n+1} = ax_n - \frac{bx_n}{cx_n - dx_{n-1}}$, Advances in Difference Equation, (2006), 1-10.
- [10]. Elabbasy E. M., El-Metwally H., Elsayed E. M., Qualitative behavior of higher order difference equation, Soochow Journal of Mathematics, 33, 4, (2007), 861-873.
- [11]. Elabbasy E. M., El-Metwally H., Elsayed E. M., Global attractivity and periodic character of a fractional difference equation of order three, Yokohama Mathematical Journal, 53, (2007), 89-100.
- [12]. Elabbasy E. M., El-Metwally H., Elsayed E. M., On the difference equation $x_{n+1} = \frac{\alpha x_{n-k}}{\beta + \gamma \prod_{i=0}^k x_{n-i}}$, J. Conc. Appl. Math., 5(2), (2007), 101-113.
- [13]. Elabbasy E. M. and Elsayed E. M., On the Global Attractivity of Difference Equation of Higher Order, Carpathian Journal of Mathematics, 24, 2, (2008), 45–53.
- [14]. Elsayed E. M., On the Solution of Recursive Sequence of Order Two, Fasciculi Mathematici, 40, (2008), 5–13.
- [15]. Elsayed E. M., Dynamics of a rational recursive sequences. International Journal of Difference Equations, 4, 2, 185–200, 2009.
- [16]. Elsayed E. M., Dynamics of a Recursive Sequence of Higher Order, Communications on Applied Nonlinear Analysis, 16, 2, (2009), 37–50.
- [17]. Elsayed E. M., Solution and attractivity for a rational recursive sequence, Discrete Dynamics in Nature and Society, (2011), 17.
- [18]. Elsayed E. M., On the solution of some difference equation, European Journal of Pure and Applied Mathematics, 4, 3, (2011), 287–303.

- [19]. Elsayed E. M., On the Dynamics of a higher order rational recursive sequence, *Communications in Mathematical Analysis*, 12, 1, (2012), 117–133.
- [20]. Elsayed E. M., Solution of rational difference system of order two, *Mathematical and Computer Modelling*, 55, (2012), 378–384.
- [21]. Gelisken A., On A System of Rational Difference Equations, *J. Comput. Anal. Appl.*, 23, 4, (2017), 593-606.
- [22]. Gibbons C. H., Kulenović M. R. S. and Ladas G., On the recursive sequence $x_{n+1} = \frac{\alpha + \beta x_{n-1}}{\chi + x_n}$, *Math. Sci. Res. Hot-Line*, 4, 2, (2000), 1-11.
- [23]. Ibrahim, T. F., Periodicity and analytic solution of a recursive sequence with numerical examples, *Journal of Interdisciplinary Mathematics*, 12, 5, (2009), 701-708.
- [24]. Ibrahim, T. F. On the third order rational difference equation, *Int. J. Contemp. Math. Sciences* 4, 27, (2009), 1321-1334.
- [25]. Ibrahim, T. F., and Touafek, N., On a third order rational difference equation with variable coefficients, *DCDIS Series B: Applications & Algorithms* 20, (2013), 251-264.
- [26]. Ibrahim T. F., Periodicity and Global Attractivity of Difference Equation of Higher Order, *Journal of Computational Analysis & Applications*, 16, 1, (2014).
- [27]. Khaliq A., Alzahrani F., and Elsayed E. M., Global attractivity of a rational difference equation of order ten, *J. Nonlinear Sci. Appl.*, 9, 6, (2016), 4465-4477.
- [28]. Kulenović M.R.S., Ladas G., Sizer W.S., On the recursive sequence $x_{n+1} = \frac{\alpha x_n + \beta x_{n-1}}{\chi x_n + \delta x_{n-1}}$ *Math. Sci. Res. Hot-Line*, 2, 5, (1998), 1-16.
- [29]. Kulenovic, M. R. S., Moranjkic, S., and Nurkanovic, Z., Naimark-Sacker bifurcation of second order rational difference equation with quadratic terms., *J. Nonlinear Sci. Appl.*, 10, (2017), 3477-3489.
- [30]. Stevic S., On the recursive sequence $x_{n+1} = \frac{x_{n-1}}{g(x_n)}$, *Taiwanese J. Math.*, 6, 3, (2002), 405-414.
- [31]. Simsek D., Cinar C. and Yalcinkaya I., On the recursive sequence $x_{n+1} = \frac{x_{n-3}}{1 + x_{n-1}}$, *Int. J. Contemp. Math. Sci.*, 1, 9, 12, (2006), 475-480.
- [32]. Simsek D., Cinar C., Karatas R., Yalcinkaya I., On the recursive sequence $x_{n+1} = \frac{x_{n-5}}{1 + x_{n-2}}$, *Int. J. Pure Appl. Math.*, 27, 4, (2006), 501-507.
- [33]. Simsek D., Cinar C., Karatas R., Yalcinkaya I., "n the recursive sequence $x_{n+1} = \frac{x_{n-5}}{1 + x_{n-1}x_{n-3}}$, *Int. J. Pure Appl. Math.*, 28, 1, (2006), 117-124.
- [34]. Simsek D., Cinar C., Yalcinkaya I., On The Recursive Sequence $x(n+1) = x[n-(5k+9)] / 1+x(n-4)x(n-9) x[n-(5k+4)]$, *Taiwanese Journal of Mathematics*, 12, 5, (2008), 1087-1098.
- [35]. Simsek D., Dogan A., On A Class of Recursive Sequence, *Manas Journal of Engineering*, 2, 1, (2014), 16-22.
- [36]. Simsek D., Eroz M., Solutions of The Rational Difference Equations $x_{n+1} = \frac{x_{n-3}}{1 + x_n x_{n-1} x_{n-2}}$, *Manas Journal of Engineering*, 4, 1, (2016), 12-20.
- [37]. Simsek D., Ogul B., Solutions of The Rational Difference Equations $x_{n+1} = \frac{x_{n-(2k+1)}}{1 + x_{n-k}}$, *Manas Journal of Engineering*, 5, 3, (2017), 57-68.

- [38]. Simsek D., Ogul B., Abdullayev F., Solutions of The Rational Difference Equations $x_{n+1} = \frac{x_{n-11}}{1 + x_{n-2} \cdot x_{n-5} \cdot x_{n-8}}$, AIP Conference Proceedings, 1880, 1, 040003, (2017).
- [39]. Simsek D., Abdullayev F., On The Recursive Sequence $x_{n+1} = \frac{x_{n-(4k+3)}}{1 + \prod_{r=0}^2 x_{n-(k+1)r-k}}$, Journal of Mathematics Sciences, 6, 222, (2017), 762-771.
- [40]. Simsek, D., Abdullayev, F. G., On the Recursive Sequence $x_{n+1} = \frac{x_{n-(k+1)}}{1 + x_n x_{n-1} \dots x_{n-k}}$, Journal of Mathematical Sciences, 234, 1, (2018), 73-81.
- [41]. Simsek, D., Ogul, B., Cinar, C., Solution of the rational difference equation $x_{n+1} = \frac{x_{n-17}}{1 + x_{n-5} \cdot x_{n-11}}$, Filomat, 33, 5, (2019), 1353-1359.
- [42]. Simsek, D., Ogul, B., On The Recursive Sequence $x_{n+1} = \frac{x_{n-20}}{[1 + x_{n-2} x_{n-5} x_{n-8} x_{n-11} x_{n-14} x_{n-17}]}$, MANAS Journal of Engineering, 7, 2, (2019), 147-156.
- [43]. Yalcinkaya, I., Cinar, C., Atalay, M., On the solutions of systems of difference equations, Advances in Difference Equations, 2008, (2008), 1-9.
- [44]. Yalcinkaya, I., Cinar, C., Simsek, D., Global asymptotic stability of a system of difference equations, Applicable Analysis, 87, 6, (2008), 677-687.
- [45]. Yalcinkaya, I., Cinar, C., Global asymptotic stability of a system of two nonlinear difference equations, Fasciculi Mathematici, 43, (2010), 171-180.